
Doctoral Dissertations

Student Theses and Dissertations

Summer 2009

Guidance, navigation and control system for autonomous proximity operations and docking of spacecraft

Daero Lee

Follow this and additional works at: https://scholarsmine.mst.edu/doctoral_dissertations



Part of the [Aerospace Engineering Commons](#)

Department: Mechanical and Aerospace Engineering

Recommended Citation

Lee, Daero, "Guidance, navigation and control system for autonomous proximity operations and docking of spacecraft" (2009). *Doctoral Dissertations*. 1942.

https://scholarsmine.mst.edu/doctoral_dissertations/1942

This thesis is brought to you by Scholars' Mine, a service of the Missouri S&T Library and Learning Resources. This work is protected by U. S. Copyright Law. Unauthorized use including reproduction for redistribution requires the permission of the copyright holder. For more information, please contact scholarsmine@mst.edu.

GUIDANCE, NAVIGATION AND CONTROL SYSTEM FOR
AUTONOMOUS PROXIMITY OPERATIONS AND DOCKING OF SPACECRAFT

by

DAERO LEE

A DISSERTATION

Presented to the Faculty of the Graduate School of the
MISSOURI UNIVERSITY OF SCIENCE AND TECHNOLOGY

In Partial Fulfillment of the Requirements for the Degree

DOCTOR OF PHILOSOPHY

in

AEROSPACE ENGINEERING

2009

Approved by

Henry Pernicka, Advisor
Jagannathan Sarangapani
Ashok Midha
Robert G. Landers
Cihan H Dagli

© 2009

DAERO LEE

All Rights Reserved

ABSTRACT

This study develops an integrated guidance, navigation and control system for use in autonomous proximity operations and docking of spacecraft. A new approach strategy is proposed based on a modified system developed for use with the International Space Station. It is composed of three “V-bar hops” in the closing transfer phase, two periods of stationkeeping and a “straight line V-bar” approach to the docking port. Guidance, navigation and control functions are independently designed and are then integrated in the form of linear Gaussian-type control. The translational maneuvers are determined through the integration of the state-dependent Riccati equation control formulated using the nonlinear relative motion dynamics with the weight matrices adjusted at the steady state condition. The reference state is provided by a guidance function, and the relative navigation is performed using a rendezvous laser vision system and a vision sensor system, where a sensor mode change is made along the approach in order to provide effective navigation. The rotational maneuvers are determined through a linear quadratic Gaussian-type control using star trackers and gyros, and a vision sensor. The attitude estimation mode change is made from absolute estimation to relative attitude estimation during the stationkeeping phase inside the approach corridor. The rotational controller provides the precise attitude control using weight matrices adjusted at the steady state condition, including the uncertainty of the moment of inertia and external disturbance torques. A six degree-of-freedom simulation demonstrates that the newly developed GNC system successfully autonomously performs proximity operations and meets the conditions for entering the final docking phase.

ACKNOWLEDGMENTS

Many years have passed as I try to write acknowledgements from when I left Korea for my Ph.D. Most of all, I would like to appreciate God who led me through hardships and failures. I appreciate that God let me rely on him to overcome my ordeal and sufferings.

My mother and father have lived a devoted life for me in support of my study. I greatly appreciate their long endurance and endless love. Honestly, I was dismayed that I must request my parents' sacrifice. From now on, I want to return my debt to my parents.

I sincerely appreciate Dr. Henry Pernicka who has worked for me as my academic advisor. He has clarified many ambiguities in my research and kept pace with me to make progress quickly in a limited time. I deeply appreciate his favor and effort.

I appreciate Dr. John Cochran with all my heart who was my first advisor when I came to the U.S. I always have felt sorry that I could not keep studying with him. While I researched with him in Auburn University, he helped me to establish an academic basis and motivation for my Ph.D. research. I spent a long time with him in deriving equations and listening to his kind explanations.

I would like to appreciate all of my committee members (Dr. Jagannathan Sarangapani, Dr. Ashok Midha, Dr. Robert G. Landers and Dr. Cihan H Dagli). Dr. Sarangapani was glad to accept my request to discuss my research progress and answered several of my questions. Dr. Midha always treated me kindly and helped me a lot. I deeply appreciate him. I also appreciate Dr. Landers and Dr. Dagli who were delighted to become my committee members.

When I was a master's student in Konkuk University, Seoul, Korea, I was a graduate student of Dr. Young Jae Lee. I appreciate his encouragement and care though I was not an excellent student. I am thankful to my grandmother and maternal grandmother who always wish my prosperity. I appreciate my younger sisters (Seol Hwa, Nam Hwa, Keum Hwa) and my younger brother (Dae Woong). I appreciate Christian fellows praying for me in the Calvary Korean Presbyterian church. Finally, I appreciate everyone who always wishes my prosperity.

TABLE OF CONTENTS

	Page
ABSTRACT.....	iii
ACKNOWLEDGMENTS	iiiiv
LIST OF ILLUSTRATIONS.....	vii
LIST OF TABLES.....	x
SECTION	
1. INTRODUCTION	1
1.1. BACKGROUND AND DEVELOPMENT.....	1
1.2. NAVIGATION SYSTEMS	8
1.3. OBJECTIVES AND OUTLINES.....	10
2. OVERVIEW OF PROXIMITY OPERATIONS STRATEGIES.....	14
2.1. OVERVIEW OF PROXIMITY OPERATIONS STRATEGY OF THE SHUTTLE.....	14
2.2. OVERVIEW OF NEW PROXIMITY OPERATIONS STRATEGY.....	15
3. GNC PROXIMITY OPERATIONS ARCHITECTURE	18
4. DYNAMIC MODELING.....	21
4.1. COORDINATE SYSTEM.....	21
4.2. TRANSLATIONAL RELATIVE MOTION DYNAMICS.....	22
4.3. ROTATIONAL MOTION DYNAMICS AND KINEMATICS	26
5. GUIDANCE FUNCTION.....	30
6. NAVIGATION FUNCTION.....	33
6.1. NONLINEAR SYSTEM STATE ESTIMATION.....	33
6.1.1. Extended Kalman Filter Description	34
6.1.2. Unscented Kalman Filter Description.....	37
6.2. RELATIVIS SCANNING SYSTEM-BASED RELATIVE STATE ESTIMATION USING THE EXTENDED KALMAN FILTER.....	42
6.2.1. LIDAR Measurements.....	42
6.2.2. Relative Position and Velocity Estimation	43
6.3. ABSOLUTE ATTITUDE ESTIMATION USING STAR TRACKERS AND GYROSCOPES.....	45

6.3.1. Star Tracker Measurements	45
6.3.2. Absolute Attitude Estimation.....	46
6.4. VISION-BASED RELATIVE STATE ESTIMATION USING THE EXTENDED KALMAN FILTER.....	52
6.4.1. Vision-Based Navigation System and Gyro Model.....	52
6.4.2. Relative State Estimation.....	56
6.5. VISION-BASED RELATIVE STATE ESTIMATION USING THE UNSCENTED KALMAN FILTER	61
6.6. SIMULATION RESULTS AND ANALYSIS.....	66
6.6.1. Bounded Relative Motion.....	66
6.6.2. Rendezvous Maneuver.....	77
6.7. CONCLUSION.....	81
7. CONTROL FUNCTION	83
7.1. SDRE TRACKING FORMULATION FOR TRANSLATIONAL MOTION...83	
7.2. LINEAR QUADRATIC TRACKING FORMULATION FOR TRANSLATIONAL MANEUVERS.....	88
7.3. LINEAR QUADRATIC GAUSSIAN-TYPE CONTROL FORMULATION FOR TRANSLATIONAL MANEUVERS.....	91
7.4. LINEAR QUADRATIC GAUSSIAN-BASED CONTROL FORMULATION FOR ROTATIONAL MANEUVER.....	92
7.5. NUMERICAL RESULTS AND ANALYSIS	95
7.6. CONCLUSION	109
8. NUMERICAL RESULTS AND ANALYSIS.....	111
9. CONCLUSION.....	124
9.1. GUIDANCE FUNCTION.....	124
9.2. NAVIGATION FUNCTION.....	124
9.3. CONTROL FUNCTION.....	125
10. FUTURE WORK.....	127
BIBLIOGRAPHY.....	128
VITA	137

LIST OF ILLUSTRATIONS

Figure	Page
1.1. Gemini 7 Photographed for Gemini by the Gemini 6 Crew after the First Space Rendezvous.....	2
1.2. Gemini and Agena Docking	2
1.3. Apollo 17 LEM.....	3
1.4. Apollo 15 CSM.....	3
1.5. Shuttle Atlantis Docked to Mir.....	4
1.6. Shuttle Situational Awareness Display.....	4
1.7. DART and MULCOM System.....	5
1.8. DART Proximity Operations.....	5
1.9. Orbital Express System.....	6
1.10. XSS-11 System.....	6
1.11. Jules Verne ATV.....	7
1.12. ATV Docking to Zeveda.....	7
1.13. Autonomous Rendezvous and Docking Program Timeline.....	8
1.14. Approach Strategy to $-V$ -bar Docking Port.....	10
1.15. Shuttle Proximity Operations Trajectory.....	11
2.1. New Proximity Operations Strategy.....	16
3.1. GNC Rendezvous Functional Architecture.....	18
3.2. Closed-Loop GNC System.....	20
4.1. CW and Body-Fixed Frames.....	21
4.2. General Type of Spacecraft Formation with Relative Motion.....	23
6.1. Example of the UT for Mean and Covariance Propagation.....	41
6.2. VISNAV System for Proximity Operations and Docking.....	53
6.3. Beacons Configuration on the Target Docking Port.....	53
6.4. Ground Tracks of Target and Chaser	67
6.5. Orbits of of Target and Chaser	67
6.6. Beacons Configuration in the CW Frame.....	68
6.7. Target Gyro Bias Estimate.....	70

6.8. Chaser Gyro Bias Estimate.....	70
6.9. Attitude Errors and 3σ Bounds by EKF Filter.....	71
6.10. Attitude Errors and 3σ Bounds by UKF Filter.....	71
6.11. Attitude Error Norms.....	72
6.12. Estimated Relative Orbit and Error.....	72
6.13. Relative Position Errors.....	73
6.14. Relative Velocity Errors.....	73
6.15. Attitude Error Norms.....	74
6.16. Attitude Errors and 3σ Bounds by UKF Filter	74
6.17. Attitude Error Norms.....	75
6.18. Attitude Errors and 3σ Bounds by UKF Filter	75
6.19. Attitude Error Norms.....	76
6.20. Attitude Errors and 3σ Bounds by UKF Filter.....	76
6.21. Attitude Error Norms.....	78
6.22. Relative Position Errors.....	78
6.23. Relative Velocity Errors.....	79
6.24. Rendezvous Maneuver Trajectory.....	79
6.25. Attitude Error Norms.....	80
6.26. Relative Position Errors.....	80
6.27. Relative Velocity Errors.....	81
6.28. Rendezvous Maneuver Trajectory.....	81
7.1. Desired Control Effect.....	83
7.2. Implementation of the Closed-Loop Optimal Control.....	87
7.3. Implementation of Optimal Tracking System.....	90
7.4. Linear Quadratic Gaussian-Type Controller.....	91
7.5. Geometry of Axis Alignment.....	96
7.6. Proximity Operation Trajectories.....	97
7.7. Out-of-Plane Relative Motion.....	98
7.8. First R-Bar Approach.....	98
7.9. Second R-Bar Approach.....	99
7.10. First Stationkeeping Subsegment.....	100

7.11. V-Bar Hopping Approach.....	100
7.12. Second Stationkeeping Subsegment.....	101
7.13. Straight LOS FINAL V-Bar Approach.....	101
7.14. Position Tracking Error History.....	103
7.15. Approach Range Rate History.....	103
7.16. Control Force History.....	104
7.17. Propellant Mass Consumption.....	105
7.18. Target and Chaser Quaternion Histories.....	106
7.19. Euler Angle Histories.....	106
7.20. Angle Error History.....	107
7.21. Angular Rate Histories.....	108
7.22. Chaser's Gravity-Gradient and External Torque Histories.....	108
7.23. Control Torque History.....	109
8.1. (a) Approach Trajectories and (b) Approach Trajectories	112
8.2. Proximity Operations in 3-D Space.....	113
8.3. Relative Position History.....	114
8.4. Tracking Error History.....	114
8.5. Approach Velocity History.....	115
8.6. Nominal Bearing History.....	116
8.7. Control Force History.....	117
8.8. Position Errors and 3σ Bounds.....	117
8.9. Velocity Errors and 3σ Bounds.....	118
8.10. Target and Chaser Quaternion Histories.....	119
8.11. Euler Angler Histories.....	119
8.12. Euler Angle Error History.....	120
8.13. Angular Rate Histories.....	120
8.14. Chaser's Gravity-Gradient and External Torque History.....	121
8.15. Control Torque History.....	121
8.16. Propellant Mass Consumption.....	122
8.17. Attitude Errors and 3σ Bounds.....	123

LIST OF TABLES

Table	Page
6.1. Continuous-Discrete Extended Kalman Filter.....	36
6.2. Discrete Unscented Kalman Filter	40
6.3. RELAVIS LIDAR Sensor Specifications.....	42
6.4. Extended Kalman Filter for Absolute Attitude Estimation.....	51
6.5. Extended Kalman Filter for Relative Attitude Estimation	60
6.6. Inertial Propagation Force Model.....	69
8.1. Conditions for Entering Docking Phase (3σ)	115

1. INRODUCTION

1.1. BACKGROUND AND DEVELOPMENT

Autonomous rendezvous and docking [1-12] are important technologies for current space programs, including transportation missions such as supply and repair to the International Space Station (ISS) and future space exploration of the Moon, Mars, and beyond. Proximity operations (PO) [2], [4], [7] and docking require extremely delicate and precise translational and rotational maneuvers. In the final approach during the proximity operations phase, the relative position, velocity, attitude and angular rates between the target and the chaser spacecraft are required to be precisely controlled to obtain the required docking interface conditions. In addition, precise relative position, velocity and attitude state estimations are required. This requirement has necessitated the development and application of various precision sensors.

The first spacecraft rendezvous and docking dates back to the manned U.S. Gemini [6] and Apollo programs [7], [13], [14] and the unmanned Russian Cosmos missions of the late 1960s. The first rendezvous and docking operations were conducted by the Gemini program in December 1965. Its objective was to develop techniques for advanced space travel, notably those necessary for the Apollo project, whose objective was to land humans on the Moon. The Gemini program provided valuable experience in developing both pre-mission and in real-time alternate procedures to address on-board and ground system problems. Gemini 7 (Figure 1.1) was originally intended to fly after Gemini 6, but the original Gemini 6 mission was cancelled after the failure during the launch of the Agena Target Vehicle (Figure 1.2) with which it was to rendezvous and dock. However the rendezvousing objective was so important it was decided to fly Gemini 6 at the same time as Gemini 7, using the latter as the rendezvous target. The Gemini program consisted of a total of 19 launches, 2 initial uncrewed test missions, 7 target vehicles, and 10 crewed missions, each of which carried two astronauts to Earth orbit. Designed as a bridge between the Mercury and Apollo programs, the Gemini program primarily tested equipment and mission procedures and trained astronauts and ground crews for future Apollo missions. The general objectives of the program included: long duration flights testing the ability to maneuver a spacecraft and to achieve

rendezvous and docking of two vehicles in Earth orbit training of both flight and ground crews conducting experiments in space; extravehicular operations (standup sessions and spacewalks) active control of reentry to achieve a precise landing and onboard orbital navigation.



Figure 1.1. Gemini 7 as seen from Gemini 6 during their rendezvous in space (Figure Taken from Reference [15])

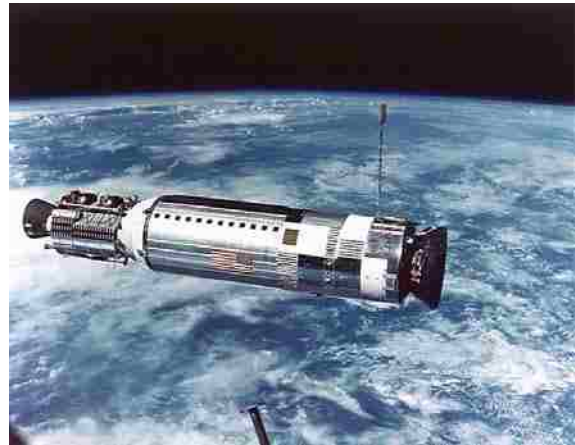


Figure 1.2. Gemini and Agena Docking (Figure Taken from Reference [16])

The Apollo program was designed to land humans on the Moon and bring them safely back to Earth. For Apollo, the Lunar Excursion Module's (LEM) (Figure 1.2) guidance and control system functioned as the chaser vehicle and was similar to the Gemini's. The crew's interaction in the Command Service Module (CSM) (Figure 1.3) functioned as the target vehicle with LEM's guidance and control system also similar to the Gemini's. The LEM avionics included a guidance digital computer, an inertial measurement unit (IMU), optical equipment for IMU alignment, and a rendezvous radar operating from 740 km to 24 meters. The rendezvous radar in the LEM, which is an interferometric-type system, provided the CSM's range, range rate, and bearing to crew displays and to the guidance computer for maneuver computations. The Apollo program, even with limited computer resources, could demonstrate many of the automated guidance, navigation and control functions required for present-day autonomous rendezvous and docking.

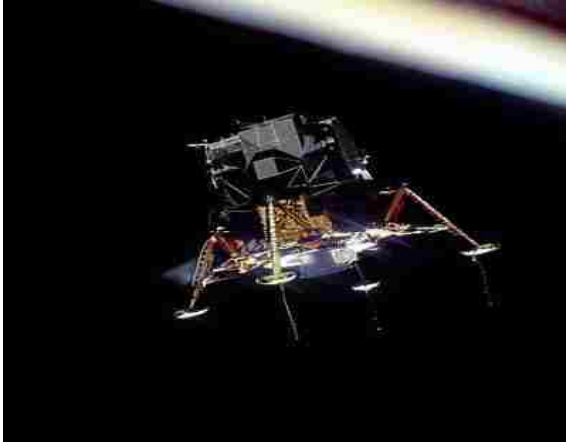


Figure 1.3. Apollo 17 LEM.
(Figure Taken from Reference [17])



Figure 1.4. Apollo 15 CSM.
(Figure Taken from Reference [18])

As the next step to the Apollo program, the Shuttle program, beginning from the early 1980s, has demonstrated rendezvous and docking functions for various types of spacecraft. The Shuttle Orbiter's Guidance, Navigation and Control (GNC) system is also similar to the LEM's as far as rendezvous and docking are concerned. Small and large target vehicles, as well as plume impingement concerns with the Shuttle Reaction Control System (RCS) jets, drove the development for new piloting techniques. This led to an increase in sophistication of proximity operations. Proximity operations for the Shuttle required more planning and analysis than it did for Gemini and Apollo missions. Rendezvous and docking missions to Mir (Figure 1.5) and the International space station (ISS) involved crew transfer, re-supply, and transport of new station elements. The sensor system used for the Apollo program is still used for the Shuttle's GNC system. In addition to this sensor system, the Trajectory Control Sensor (TCS), which is a laser ranging device that is mounted in the Orbiter's payload bay for short range use, is used to provide range, range rate, and bearing to the target for display to the crew at ranges varying from 1.5 km to 1.5 meters. The onboard GNC system, through the crew command, can automatically perform various rendezvous functions including translation and rotational control, targeting, and relative navigation. However, the crew manually performs the final phase approach maneuvering within about 90 meters of the target

using visual images from the centerline camera fixed to the center of the Orbiter's docking mechanism, TCS and laptop situational awareness displays shown in Figure 1.6.

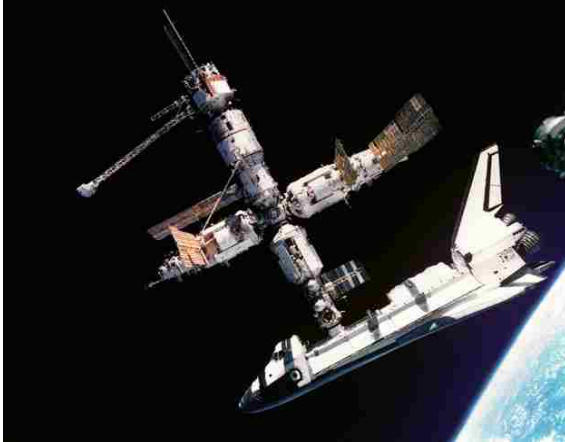


Figure 1.5. Shuttle Atlantis Docked to Mir. (Figure Taken from Reference [18])

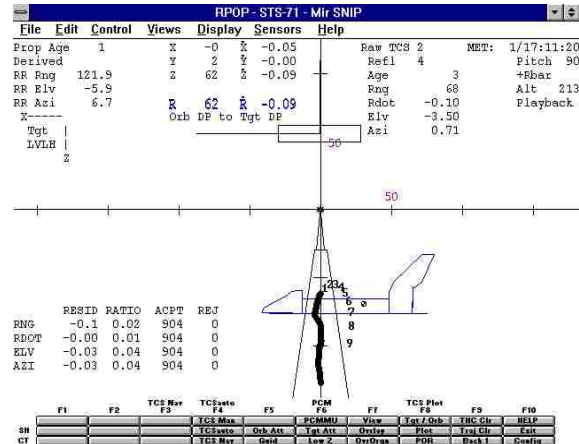


Figure 1.6. Shuttle Situational Awareness Display. (Figure Taken from Reference [19])

Since the early 2000s, there have been several programs proposed to demonstrate the capability to perform autonomous rendezvous and docking. The DART [25-27] (Demonstration of Autonomous Rendezvous Technology) mission, which was a joint program between the Marshall Space Flight Center and Orbital Sciences Corporation, was intended to provide a key step in establishing autonomous rendezvous capabilities for the U.S. space program by performing autonomous rendezvous. On April 15, 2005, the DART spacecraft was successfully deployed from a Pegasus XL rocket launched from the Western Test Range at Vandenberg Air Force Base, California. DART, which is illustrated in Figure 1.7, was designed to rendezvous with and perform a variety of maneuvers in close proximity to the Multiple Paths, Beyond-Line-of-Sight Communications (MUBLCOM) satellite, without assistance (autonomously) from ground personnel. The NASA spacecraft performed nominally during the first eight hours of the mission-launch, checkout, and rendezvous phases. It accomplished all objectives up to that point, though ground operations personnel noticed some anomalies with the spacecraft's navigation system. However, DART had no means to receive or execute

uplinked commands, so the ground crew could not take any action to correct the anomalies. Approximately 11 hours into the mission, the spacecraft detected its propellant supply was depleted and began a series of maneuvers for “departure and retirement.” As a result, portions of the mission were deemed failures. A mishap investigation board for the DART determined that the first cause of its premature retirement occurred when the estimated and measured positions differed to such a degree that the software executed a computational “reset.” By design, the reset caused DART to discard its estimated position and speed and restart those estimates using measurements from the primary GPS receiver. DART used GPS for long-range measurements and the Advanced Video Guidance System (AVGS) for proximity operations (See Figure 1.8).



Figure 1.7 DART and MULCOM System.
(Figure Taken from Reference [20])

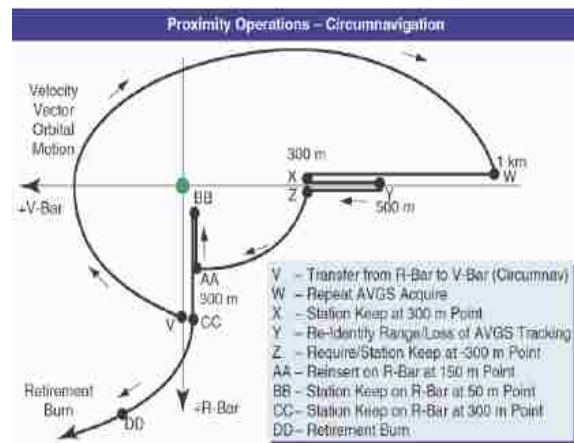


Figure 1.8. DART Proximity Operations
(Figure Taken from Reference [21])

The Orbital Express [28] program was a space mission managed by the U.S. Defense Advanced Research Projects Agency (DARPA) and a team led by engineers at NASA's Marshall Space Flight Center. The project aimed to demonstrate several satellite servicing operations and technologies including rendezvous, proximity operations and stationkeeping, capture, docking, and fluid transfer (hydrazine). May 11, 2007, the Boeing Orbital Express system, shown in Figure 1.9, completed another first by successfully performing a fully autonomous free-flight rendezvous and capture operation.

The system consisted of two spacecraft: the Autonomous Space Transport Robotic Operations (ASTRO) vehicle and a prototype modular next-generation serviceable satellite (NEXTSat). The program demonstrated several sensor technologies for long- and short-range navigation. The AVGS system was also used for close-range position estimation and attitude estimation. The final rendezvous and docking between the two spacecraft occurred on June 29, 2007 after three months of highly successful demonstrations.

The Experimental Satellite System (XSS) series [14], [29] conducted by the U.S. Air Force, is to demonstrate increasing levels of microsatellite technology maturity such as inspection, rendezvous and docking, repositioning and techniques for close-in proximity maneuver around orbiting satellites. The XSS-10 is the first microsatellite in the series and was launched in 2003. It demonstrated semi-autonomous operations and visual inspection in close proximity of an object in space. The success of the XSS-10 flight demonstration was the first step in applying micro-satellite technology to military space missions and paved the way for more ambitious experiments on XSS-11 and future programs. The subsequent spacecraft in the series, XSS-11 shown Figure 10, used an active LIDAR [30-35], (Light Detection and Ranging) system for its rendezvous mission, featuring a passive camera and star tracker for relative navigation.



Figure 1.9. Orbital Express System.
(Figure Taken from Reference [22])

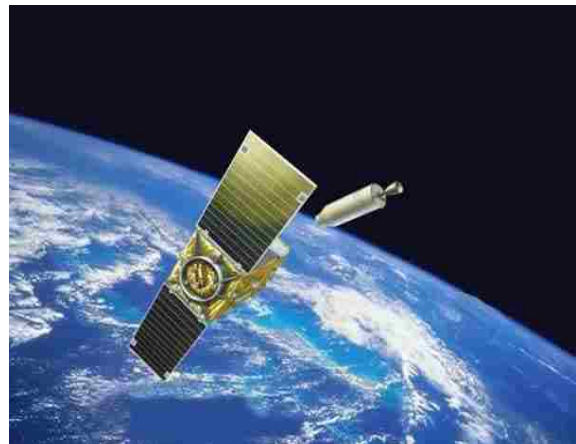


Figure 1.10. XSS-11 System.
(Figure Taken from Reference [23])

The LIDAR system is an optical remote sensing technology that measures properties of scattered light to find range and/or other information of a distant target. A LIDAR instrument suitable for use in rendezvous space applications is the Rendezvous Laser Vision (RELAVIS) scanning system [30-35].

The ATV [36-46] (Automated Transfer Vehicle) is an expendable, unmanned resupply spacecraft developed by the European Space Agency (ESA). The ATV program is designed to perform automated phasing, approach, rendezvous and docking to the ISS, followed by departure and deorbit maneuvers. It uses absolute and relative GPS navigation and star trackers to automatically rendezvous with the ISS. At a distance of 249 m, the ATV computers use videometer and telegoniometer data for final approach and docking maneuvers. The actual docking to Zvezda (see Figure 1.8), the Russian service module on the ISS, is fully automatic. The first mission of the Jules Verne ATV was launched on March 9, 2008 and docked successfully to the ISS on April 3, 2008. Jules Verne ATV, shown in Figure 1.11, also successfully demonstrated the critical Collision Avoidance Maneuver. The elements composing the ATV nominal rendezvous strategy [36-45] include a drift phase, homing transfer, closing transfer, and final translation. Figure 1.12 illustrates the ATV's approach maneuver when docking with Zvezda.



Figure 1.11. Jules Verne ATV.
(Figure Taken from Reference [24])

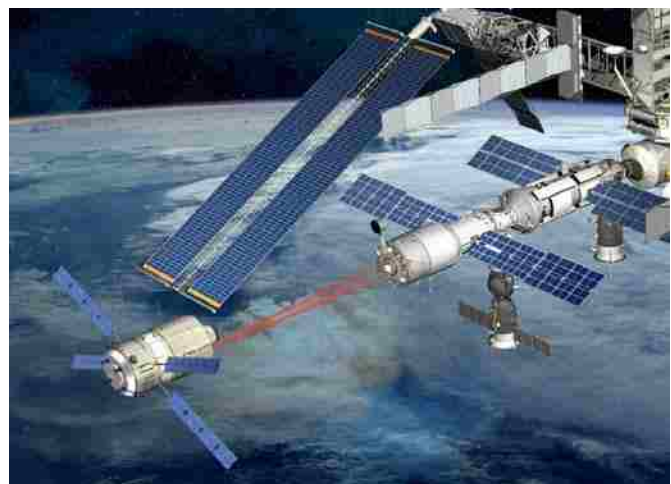


Figure 1.12. ATV Docking to Zvezda.
(Figure Taken from Reference [25])

Other programs are also under development involving autonomous rendezvous and docking such as the Japanese HTV (H-2 Transfer Vehicle), the Russian Progress vehicle, and the recent Hubble Robotic Servicing and Deorbit Mission (HRSDM) led by the NASA Goddard Space Flight Center and Lockheed Martin. Figure 1.13 [14] illustrates a time line of autonomous rendezvous and docking programs.

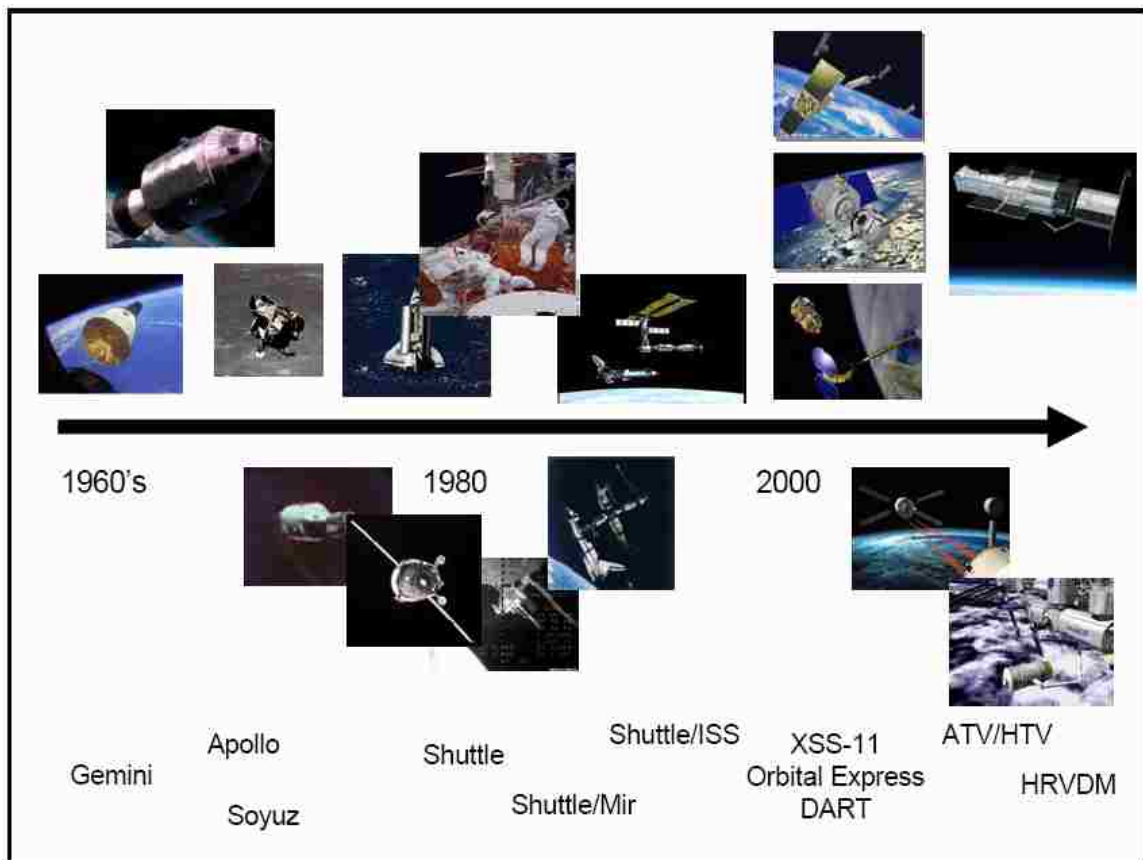


Figure 1.13. Autonomous Rendezvous and Docking Program Timeline. (Figure Taken from Reference [14])

1.2. NAVIGATION SYSTEMS

Proximity operations and docking are the phases requiring highly precise translational and rotational maneuvering. These requirements led to the development and evaluation of several relative navigation sensors, such as the Advanced Video Guidance

Sensor (AVGS), GPS, LIDAR, laser dynamics ranger imager (LDRI), and optical sensors combined with structured active light sources, star tracker, and the Inertial Navigation System (INS). Relative GPS (RGPS) navigation in the ATV program successfully fulfills the GNC and safety requirements for approaching the ISS from locations S0 to S3 as illustrated in Figure 1.14 [36-45]. When a spacecraft approaches the ISS for rendezvous, the signals from the GPS satellites may be blocked by the ISS structure leading to the lack of visibility or degradation from multi-path effects [38-49]. For this reason, RGPS cannot meet the necessary navigation requirements for docking in the ATV program. RGPS is not used in either the Shuttle rendezvous or proximity operations due to various concerns such as accuracy deterioration, multi-path effects, unreliability and antenna obscuration [48], [49]. At location S3 RGPS navigation is replaced by the Relative Navigation system with Videometer (RVDM). The RVDM system provides the relative position, velocity and attitude in the final approach meeting docking requirements.

This study uses the RELAVIS system based on scanning laser radar measurements, designed by Optech and MD Robotics [30], [31] and a vision-based navigation (VISNAV) system (which uses Position Sensing Diodes (PSD)) [50-57] as alternatives to RGPS and RVDM. The RELAVIS scanning system provides an integrated laser-based vision system that obtains relative position and orientation of a target vehicle. This system was demonstrated successfully in the XSS-11 program. Its application is also useful for deep space exploration where GPS is not available. The navigation system using the RELAVIS scanning system in this study provides the relative position and velocity. As the two vehicles get closer, the VISNAV measurements become more accurate, at which point a sensor mode switch is made to the VISNAV system to take advantage of the more accurate relative position, velocity, and attitude measurements in the final straight line approach before S4. With the use of the RELAVIS scanning system in the closing transfer and straight line translational approach to S4 from S3, star trackers and three axis gyroscopes (gyros) are also used to estimate the chaser absolute attitude in those phases. This study also adopts and modifies the approach strategy of the ATV shown in Figure 1.14. It considers the closing transfer to the final translational approach for the acquisition of the required docking conditions. Moreover, S3, which is where the navigation system switches from RGPS to RVDM, is now relabeled S4 where the

RELAVIS scanning system and star trackers-based absolute attitude estimation are replaced by the VISNAV system.

1.3. OBJECTIVES AND OUTLINES

Among the space programs discussed, the approach strategy used by the ATV of translating to the docking port located along the $-V$ -bar direction as shown in Figure 1.14 is selected and modified as a case-study to evaluate the integrated GNC system proposed in this study. In addition, the GNC system is developed to have the capability of autonomously meeting the final conditions required during the docking phase of the proximity operations. Autonomy is defined as the ability for a vehicle and its onboard system to perform a function without external support.

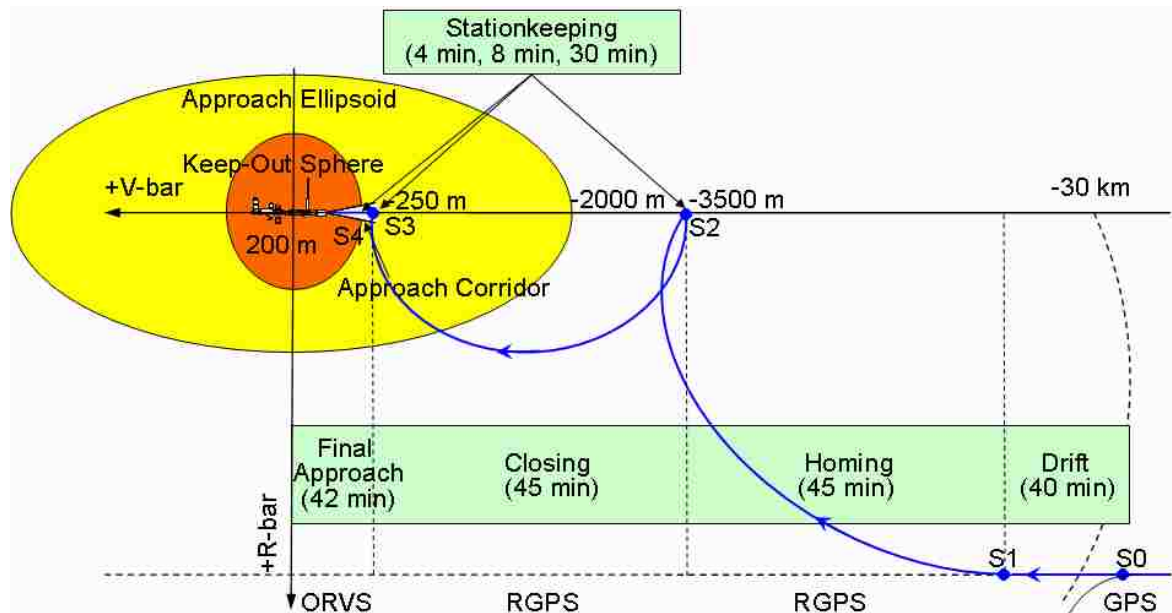


Figure 1.14. Approach Strategy to $-V$ -bar Docking Port. (Figure Taken from References [46-45])

The level of autonomy is the degree with which a function can be performed by on board systems and the crew without ground system support, or support from other vehicles.

Autonomous proximity operations are characterized by controlling a chaser vehicle about a predetermined reference trajectory toward the docking port of the target. This study proposes an integrated autonomous GNC system for the proximity operations and docking of a spacecraft with an ISS-type vehicle. The proposed integrated GNC system is composed of an independent guidance function, navigation function and control function.

The Shuttle crew's manual flight segment was chosen to demonstrate the autonomous control techniques. The Shuttle program is scheduled to be retired by 2010; however, the Shuttle orbiter's standard ISS approach techniques will likely be applied to other future programs. The optimal control techniques developed in this study are applied to the Shuttle orbiter's manual phase flight segment including proximity operations and entering the docking phase as shown in Figure 1.15 [4], [49], [50], [58], [59]. The goal for autonomous proximity operations is to meet the conditions for a successful docking.

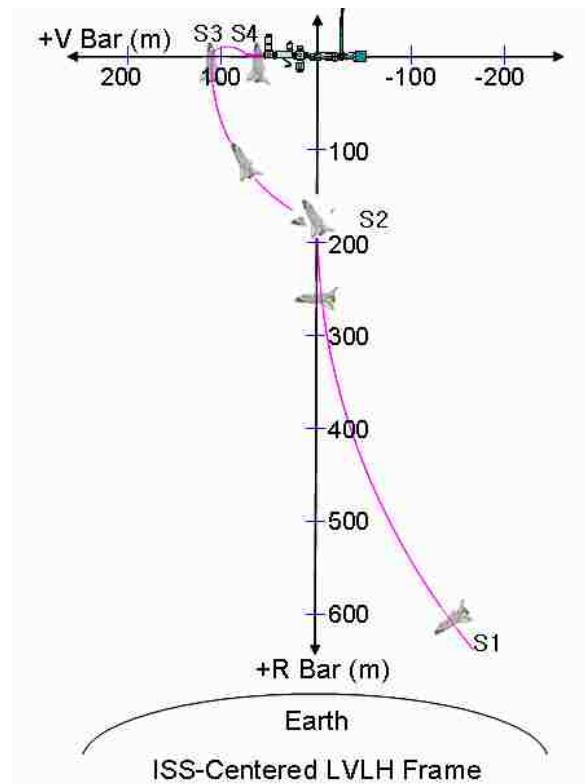


Figure 1.15. Shuttle Proximity Operations Trajectory. (Figure Adapted from Reference [4], [49], [50], [58], [59])

The task of the guidance function is to provide the desired trajectory of the chaser as nominal values of the state vector at each point in time, enabling the control function to determine the control commands. The Clohessy-Wiltshire (CW) terminal guidance scheme [60-62] is used to determine the proper transfer time, reference trajectory, and required ΔV during the closing phase. The straight line V-bar approach is used for the final approach from the ending point of the closing to the docking port of the target to enable soft docking. For the stationkeeping phase, the exponential braking law [63] is used to nullify the approach. The desired quaternion and angular rates of the target, computed by onboard navigation, are provided to the attitude controller. Relative position, velocity, attitude and angular rate of the chaser are provided to the control function.

The task of the navigation function is to provide the best estimate of the current state of the chaser vehicle to the guidance and control functions using the extended Kalman filter (EKF) [64-67]. The RELAVIS scanning system provides relative position and velocity from S2 to S4. A switch is then made to VISNAV to provide more accurate navigation and relative attitude measurements. Like the sensor mode switch for the translational maneuvers, there is also a sensor mode switch for the rotational maneuvers. Absolute attitude estimation of the chaser using star trackers and rate integrating gyros is used from S2 to S4. Relative attitude estimation is then performed from S4 to the docking port using vision sensors. The estimated relative positions, velocities and attitudes, determined through the integrated navigation system, are fed to the Control function.

The task of the Control function is to provide the control force and control torque commands that will be executed by the control system of the chaser vehicle to track the reference trajectory and attitude. For the translational control of the chaser vehicle, state-dependent Riccati equation (SDRE) control is used [67-72], [77-81] based on the nonlinear relative motion dynamics including the Earth oblateness and air drag perturbations. For the attitude control of the chaser vehicle, a linear quadratic regulator (LQR) [71], [72] controller with linear closed-loop error dynamics is used to drive the chaser absolute attitude and angular rate to the desired attitude. This controller is then combined with an extended Kalman filter, leading to a linear quadratic Gaussian (LQG)-type control [71-73] system. As with the translational maneuvering, the LQG-type

attitude control system is integrated with the SDRE controller. Guidance, navigation and control functions are integrated into a feedback closed-loop system. The GNC is then performed autonomously by real-time.

In Chapter 2, the high-level proximity operations strategy of the Shuttle is reviewed. The proximity operations strategy developed in this study, modified from the current strategy for the ATV, is described. In Chapter 3, the GNC proximity operations architecture is described. In Chapter 4, the dynamic modeling for control and estimation formulations is set forth. In Chapter 5, the guidance function, which is composed of the CW guidance terminal scheme, exponential braking law for stationkeeping phase, and straight line V-bar approach leading to soft docking, is described. In Chapter 6, the navigation function, including the use of several navigation sensors, is described. The use of EKF algorithms and the unscented Kalman filter (UKF) algorithm is established. In Chapter 7, the design of the control function based on optimal control techniques is described. The integration of each function composing the autonomous GNC system is then described. Finally, the autonomous optimal control techniques are demonstrated for Shuttle-like proximity operations and the GNC system is demonstrated for the newly proposed approach strategy using six-degree-of numerical simulations.

2. OVERVIEW OF PROXIMITY OPERATIONS STRATEGIES

Optimal control techniques are summarized for the proximity operations strategy of the Shuttle. The GNC system proposed in this study, modified from that of the ATV, is also summarized.

2.1. OVERVIEW OF PROXIMITY OPERATIONS STRATEGY OF THE SHUTTLE

The trajectory profile design in the manual flight phase of the Shuttle is highly dependent on the payload configuration. Payload attitude control and susceptibility to plume impingement are primary drivers in the final approach. The preferred technique for plume impingement prevention is the use of the V-bar guidance method during the final approach, which guides the approach of the Shuttle (chaser) along the velocity vector toward a target such as the ISS. This approach along the target's velocity vector, a form of pursuit guidance, is well-known and has been thoroughly investigated dating back to the Gemini program. The piloting procedure is relatively easy to execute. To initiate the V-bar approach, the active vehicle nulls the orthogonal relative velocities along the V-bar direction and accelerates to the desired closing rate along the V-bar direction, which is now along the line of sight to the target. The V-bar final approach is desirable because it is relatively fuel efficient. In addition, the constant Earth horizon orientation provides a good piloting reference, and closing rates can be easily and immediately nulled with subsequent stationkeeping should some Shuttle or payload system anomaly occur. The trajectory of the Shuttle to the ISS in use since the STS-102 mission in 2001 is by default the starting point for the design of the lower surface inspection maneuver. Figure 1.15 shows this approach trajectory in the rotating local vertical local horizontal (LVLH) frame, centered at the ISS center of mass. This trajectory satisfies the many constraints on visual and sensor visibility, plume impingement pressures and contamination, propellant consumption, and other factors. The reaction control system of the Shuttle orbiter is used to provide thrusters for this approach trajectory. The 38 Primary Reaction Control System (PRCS) thrusters are arrayed around the Shuttle orbiter. The final orbit of the Shuttle orbiter rendezvous profile targets a point 183 m (600 ft) below the ISS along the R-bar

direction. The Shuttle orbiter crew begins manual trajectory control at a range of 610 m (2000 ft). The negative R-bar direction control is activated at 305 m (100 ft) to provide plume protection by inhibiting thrusters that fire toward the ISS. At the 183 m (600 ft) point, the Shuttle orbiter begins an 11.5 minute positive pitch automatic maneuver to the final ISS approach attitude. A simultaneous manual 0.3 m/s (1 ft/s) of V-bar translation accomplishes a slow transition from the 183 m (600 ft) R-bar departure point to the final approach corridor along the ISS V-bar. In the LVLH frame, this transition appears as a gradual spiral from 183 m (600 ft) along R-bar to approximately (107 m) 350 ft along V-bar. From the arrival point on the V-bar axis, the Shuttle orbiter slowly approaches the docking port at a rate of 0.06 to 0.03 m/sec (0.2 to 0.1 ft/sec).

2.2. OVERVIEW OF NEW PROXIMITY OPERATIONS STRATEGY

Figure 1.14 represents the approach strategy of the chaser (ATV) to the -V-bar docking port. The target vehicle (ISS) is on a quasi-circular orbit with its attitude Earth-pointing. The nominal docking of the ATV takes place on the Russian service module, Zvezda. In general, the proximity operation covers a range of less than 1 km. However, the range is extended to 3.5 km away from the docking port in this study, which still represents a close-range rendezvous. The closing transfer begins at location S2 with the use of RGPS. The FOV angles resulting from the geometry of the closing transfer may exceed the FOV limits of the RELAVIS scanning system, which is the case with the ISS/ATV. For this reason, the closing maneuver in Figure 1.14 in use for the ATV program is modified to the V-bar hopping approach developed in this study so that the RELAVIS scanning system can be used and satisfy the FOV requirements. The proximity operation operations strategy proposed here is illustrated in Figure 2.1 [39]. The various phases of this closing transfer include: V-bar hops from S2 to S3, stationkeeping at S3, straight line approach from S3 to S4, a second period of stationkeeping at S4, straight line approach from S4 to S41, a third period of stationkeeping at S41 and a straight line approach from S41 to the docking port. The proximity operation strategy is conducted step-by-step autonomously on the basis of predefined guidance and real-time navigation. The chaser is first brought to location S0 on a circular orbit about 6 km lower in altitude

and about 30 km behind the target. Since the target orbital rate is slightly higher than the chaser, the chaser catches up with the target during a pre-homing drift phase, transferring from S0 to S1 in 40 minutes. The chaser establishes the local communication link with the target at S0 (about 30 km range). While drifting on this orbit, the communication link is acquired with the target and the navigation filter for RGPS converges. A homing transfer using RGPS navigation is then initiated at S1 to bring the chaser to S2 on the target orbit, 3.5 km behind in 45 minutes. At this point S2, stationkeeping is performed, while waiting for the target and the ground control to issue a clearance to proceed [39]. This study considers the scenario beginning at S2 after the stationkeeping phase and ending at the docking port. The transfer trajectory, with all possible dispersions, is not allowed to enter the approach ellipsoid around the target. The approach ellipsoid in Figure 2.1 has an extension of ± 2000 m in the V-bar direction, ± 1000 m in the R-bar direction and ± 1000 m in the H-bar direction ellipsoid centered on the target center of mass.

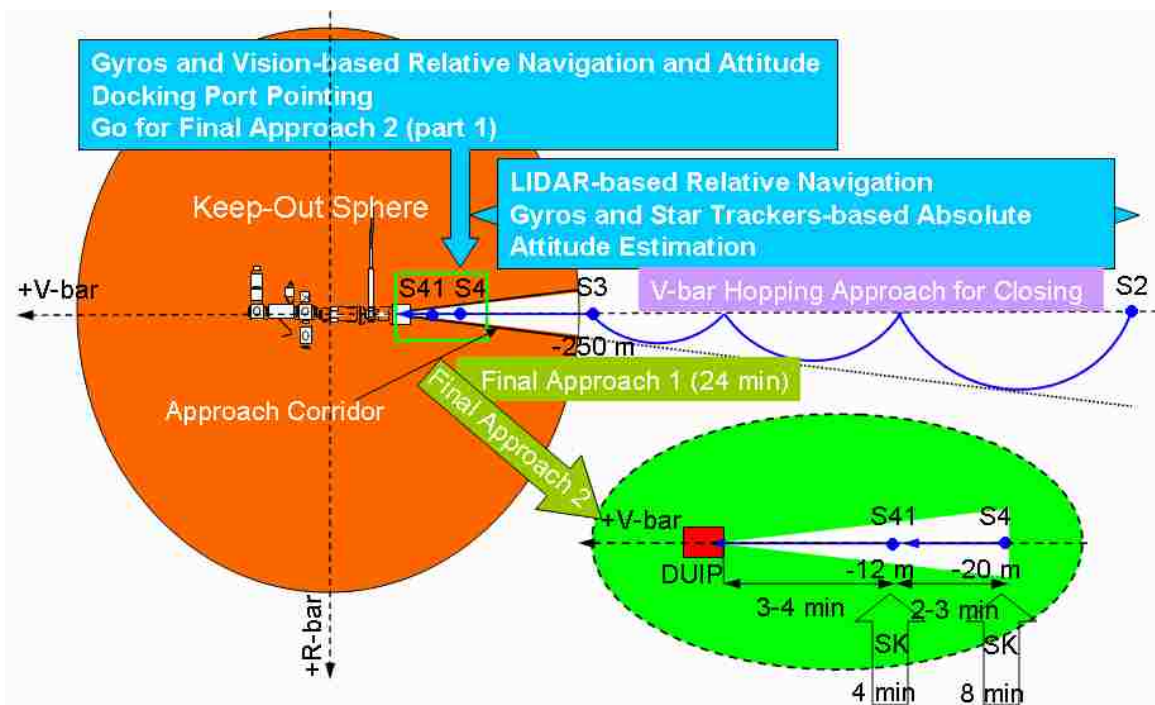


Figure 2.1. New Proximity Operations Strategy. (Figure Adapted from Reference [39])

At a holding point on the target orbit where stationkeeping takes place outside the approach ellipsoid, final check-outs of the chaser system and synchronization corrections with external events, such as lighting conditions, crew schedule, etc., take place. Prior to entering the approach ellipsoid, the chaser is under standby until the target approves the chaser to enter it. Additional excursion into the approach ellipsoid can only commence after approval from the target. The proximity operations strategy in this study spans from the closing transfer after the stationkeeping phase at S2 to the target docking port A closing transfer is executed to bring the chaser to location S3, 250 m behind the target docking port. Navigation systems originally used for the ATV were replaced here to study the benefits of alternative navigation systems. RGPS was replaced by the RELAVIS scanning system for the interval ranging from S2 to S4 and Videometer-based relative navigation was replaced by vision-based navigation for the interval ranging from S4 to the docking port. Also of importance is a 200 m spherical area surrounding the target typically labeled the “Keep-Out Sphere.” This volume can be entered only through one of the approach and departure corridors. No vehicle is allowed to penetrate this space except through the circular cone as illustrated in Figure 2.1. At S4, the navigation system is switched to more accurate sensors meeting the strict approach corridor requirements.

The GNC system performs the new proximity operations strategy without being controlled by the ground control station being helped by the target spacecraft. The GNC system autonomously switches the navigation system along the various phases and determines control commands using the predefined guidance function and the real-time onboard navigation function. The GNC system was designed to not rely on external support such as the ground system support or other spacecraft in performing the series of phases. However, troubleshooting and decision making activities by the crew members when an anomaly or emergency occurs allows the interruption of the GNC system. The GNC system, in the absence of anomalies, is fully autonomous.

3. GNC PROXIMITY OPERATIONS ARCHITECTURE

The proposed GNC system for the chaser is composed of independent guidance, navigation and control functions, managed by a centralized GNC proximity operation. Figure 3.1 provides an overview of the GNC proximity operations architecture. The GNC proximity operations for the chaser manager covers functions common for guidance, navigation and control, including command, data handling, and managing overall mission phase sequencing. Because of the many different maneuvers and navigation requirements, and the variety of attitude and navigation sensors used in the various proximity operations phases, a different set of algorithm parameters and hardware functions are used for each phase. The GNC proximity operations management can be delegated to the crew when an anomaly or contingency occurs. The GNC proximity operations functional architecture is based on separate and independent, guidance, navigation and control functions, managed by the GNC proximity operation manager.

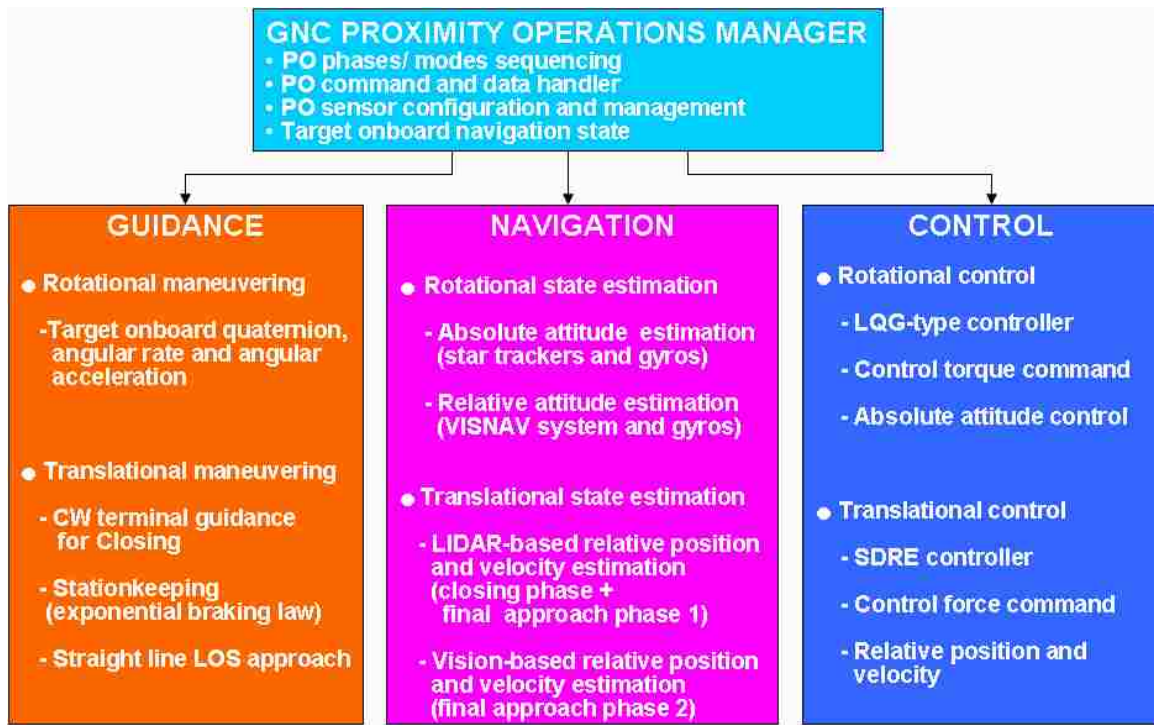


Figure 3.1. GNC Proximity Operations Functional Architecture.

The guidance function provides the predefined reference state such as including the relative position, velocity, attitude and angular rate, which will then be compared with the estimated actual values, provided by the navigation function, enabling the control function to compute the control commands. When simulating the closed-loop GNC system, the High Precision Orbit Propagator (HPOP) in Satellite Tool Kit (STK) [82] is used to produce the target's inertial position and velocity vectors. The quaternion defining the orientation of the target vehicle with respect to the inertial frame, and the target's angular rate expressed in the body-fixed frame of the target vehicle, are also simulated. However, the target's inertial position and velocity vectors, and quaternions which are acquired by onboard navigation, are transmitted to the chaser through the communication link in an actual mission.

The navigation function provides the controller with the current rotational and translational states estimated using the different navigation systems. The navigation sensors sense the measurements affected by control forces and torque commands. The navigation function can be reduced to converting the sensor information to the formats required by the control function. The different navigation systems listed in Figure 3.2 are sequentially switched along the phases to provide the efficient and reliable navigation.

The control function is in charge of determining the control forces and torques which will be executed by the RCS of the spacecraft to correct the deviations of the actual (estimated) state vector from the nominal one. The thruster management function then transforms the torque and force commands into on/off commands for the individual thrusters. This study assumes that the commands requested by the controllers can be provided by an appropriate combination of firing individual thrusters in the RCS system considering their orientations and their locations with respect to the instantaneous center of mass of the vehicle.

Each independent function shown in Figure 3.1 is integrated in a block diagram with typical closed-loops, shown in Figure 3.2, for each of the six degrees of freedom. This integrated system illustrated by Figure 3.2 becomes the GNC system performing the mission scenario autonomously.

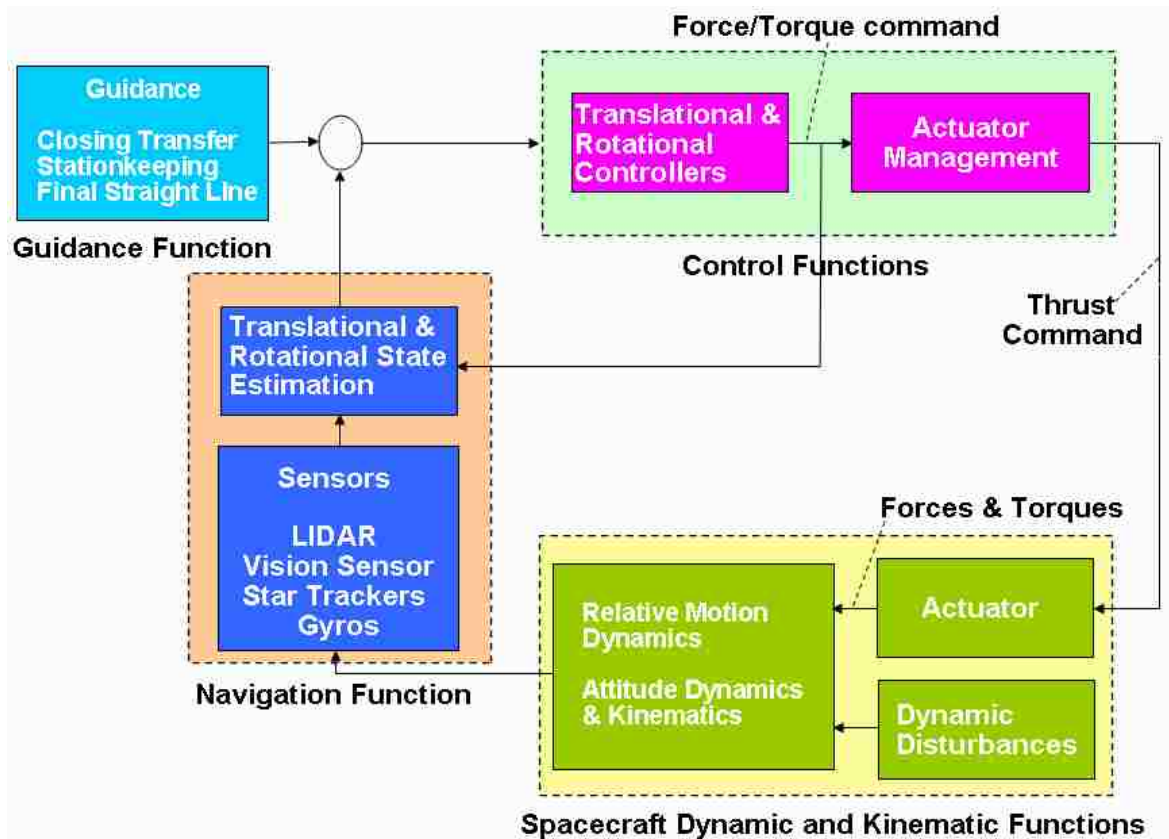


Figure 3.2. Closed-Loop GNC System.

During the proximity operations, various translational and rotational maneuvers are executed using different sensor types. This requires an initialization of the navigation system each time, in which algorithms and parameters of the navigation functions must be reset. The combined set of algorithms and parameters used to determine maneuvers is termed the GNC mode. The GNC modes consist of a set of guidance, navigation and control modes. The Guidance function provides the reference states working as feed-forward terms in the controllers. The Navigation function estimates the relative position, velocity and attitude onboard the chaser spacecraft. The estimated states are then combined with the optimal controllers by replacing the control state with the estimated state. This is proven to be optimal using the separation theorem [71], [72]. The objective of the new integrated GNC system is to perform the new proximity operations strategy autonomously meeting the required final conditions at docking successfully.

4. DYNAMIC MODELING

In this chapter, a nonlinear and a linear spacecraft relative dynamic model including relative perturbations are presented to describe the translational motion. Attitude kinematics and Euler's equations of motion (including the gravity-gradient torque) are presented to describe the rotational motion.

4.1. COORDINATE SYSTEM

The coordinate systems used are: local vertical/local horizontal (LVLH) frames centered on the target and the chaser spacecraft, an orthogonal body-fixed frame at the center of mass of each spacecraft, and an Earth-Centered Inertial (ECI) frame N , as shown in Figure 4.1. The LVLH frame is sometimes referred to as the CW frame [59-61], [83], [86] E , with the x -axis directed radially outward along the local vertical, the y -axis along the general direction of motion, and the z -axis normal to the reference orbit plane.

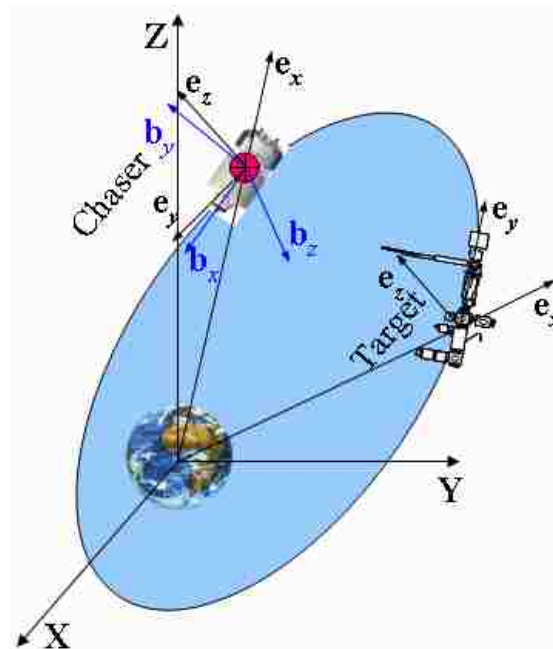


Figure 4.1. CW and Body-Fixed Frames.

In a rendezvous mission, the motion of the chaser spacecraft is commonly described relative to the target spacecraft. Instead of the CW frame E , the spacecraft local orbital frame A is adopted here to describe its motion. This frame is related to the CW frame E through

$$\begin{aligned} \mathbf{a}_x &= \mathbf{e}_y & \text{V-bar} \\ \mathbf{a}_y &= -\mathbf{e}_z & \text{H-bar} \\ \mathbf{a}_z &= -\mathbf{e}_x & \text{R-bar} \end{aligned} \quad (1)$$

where $\mathbf{a}_x, \mathbf{a}_y$, and \mathbf{a}_z are unit vectors in the spacecraft local orbital frame A , and $\mathbf{e}_x, \mathbf{e}_y$ and \mathbf{e}_z are unit vectors in the CW frame E . The $+\mathbf{a}_x$ axis is referred to as the V-bar axis, the $+\mathbf{a}_y$ axis as the H-bar axis, and the $+\mathbf{a}_z$ axis is termed the R-bar axis. The $\mathbf{b}_x, \mathbf{b}_y$, and \mathbf{b}_z axes are body-fixed unit vectors in the spacecraft to describe the attitude with respect to the inertial frame.

4.2. TRANSLATIONAL RELATIVE MOTION DYNAMICS

This section presents the nonlinear and linear relative equations of motion with methods to establish closed relative orbits. The target or reference spacecraft is denoted as the target spacecraft and the chaser or follower is denoted as the chaser spacecraft. The inertial target position vector is denoted as \mathbf{r}_t , while the chaser position is expressed as vector \mathbf{r}_c . Subscripts t and c denote the target and the chaser, respectively. The relative position vector $\boldsymbol{\rho}$ is expressed in Cartesian coordinate components as $\boldsymbol{\rho} = (x, y, z)^T$. To derive the relative equations of motion expressed in CW Cartesian coordinates, the chaser position vector is written as $\mathbf{r}_c = \mathbf{r}_t + \boldsymbol{\rho}$. This geometry is illustrated in Figure 4.2. A complete derivation of the relative equation motion for the elliptical and the circular orbit case is given in Reference [83]. Using the two two-body equations of motion for the target and the chaser the exact nonlinear relative equations of motion are given by

$$\begin{aligned}
\ddot{x} - 2\dot{f}\left(\dot{y} - y\frac{\dot{r}_t}{r_t}\right) - x\dot{f}^2 - \frac{\mu}{r_t^2} &= -\frac{\mu}{r_c^3}(r_t + x) \\
\ddot{y} + 2\dot{f}\left(\dot{x} - x\frac{\dot{r}_t}{r_t}\right) - y\dot{f}^2 &= -\frac{\mu}{r_c^3}y \\
\ddot{z} &= -\frac{\mu}{r_c^3}z, \quad r_c = \sqrt{(r_t + x)^2 + y^2 + z^2}
\end{aligned} \tag{2}$$

where x , y , z represent the relative position of chaser spacecraft with respect to the target spacecraft, r_t refers to the scalar radius of the target from the center of the Earth, r_c refers to the scalar radius of the chaser from the center of the Earth, μ is the gravitational parameter, and f is the target true anomaly. These relative equations of motion are valid for large relative orbits, and the target orbit may be eccentric.

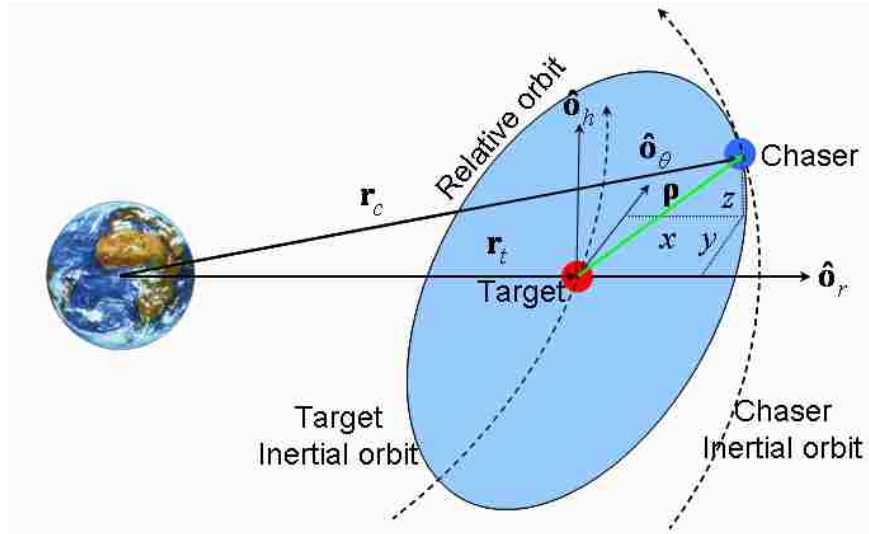


Figure 4.2. General Type of Spacecraft Formation with Relative Motion.

Both attracting body masses are assumed to be spherical, and no other perturbations are modeled. If the relative orbit coordinates (x, y, z) are small compared to the target orbit radius r_t , then Eq. (2) can be further simplified to the linear equations [83]. The

equations of motion for the translational control formulation of the LQR then are then given by

$$\begin{aligned}
 \ddot{x} - 2\dot{v}\left(1 + 2\frac{r_c}{p}\right) - 2\dot{v}\left(\dot{y} - y\frac{\dot{r}_c}{r_c}\right) &= \frac{F_x}{m(t)} \\
 \ddot{y} + 2\dot{v}\left(\dot{x} - x\frac{\dot{r}_c}{r_c}\right) - y\dot{v}^2\left(1 - \frac{r_c}{p}\right) &= \frac{F_y}{m(t)} \\
 \ddot{z} + \frac{r_c}{p}\dot{v}^2 z &= \frac{F_z}{m(t)}
 \end{aligned} \tag{3}$$

where p is the semilatus rectum. The terms F_x , F_y , and F_z are the control forces and $m(t)$ is the time varying mass of the chaser spacecraft due to the propellant mass consumption. The true anomaly acceleration and target orbit-radius acceleration are given by [82] as

$$\ddot{f} = -2\frac{\dot{r}_t}{r_t}\dot{f} \tag{4a}$$

$$\ddot{r}_t = r_t\dot{f}^2\left(1 - \frac{r_t}{p}\right) \tag{4b}$$

For generation of bounded relative motion used in the simulations, the initial condition at perigee is given by [82] as

$$\frac{\dot{y}_0}{x_0} = \frac{-n(2+e)}{\sqrt{(1+e)(1-e)^3}} \tag{5}$$

where n is the mean motion of the target and e is the target eccentricity. Among the many sources of perturbations between the target and chaser, the Earth oblateness and aerodynamic drag in low Earth orbit (LEO) are dominant. The effects of Earth oblateness and aerodynamic drag are included in the nonlinear relative equations to improve the

accuracy of the dynamic modeling. In the CW frame E , the perturbing acceleration J_2 is described by [60] as

$$\mathbf{a}_{J_2} = \frac{-3\mu J_2 R_e^2}{r^4} \left[\left(\frac{1}{2} - \frac{3\sin^2 i \sin \theta}{2} \right) \mathbf{e}_x + (\sin^2 i \sin \theta \cos \theta) \mathbf{e}_y + (\sin i \sin \theta \cos i) \mathbf{e}_z \right] \quad (6)$$

where R_e is the radius of the Earth, i is the inclination, and θ is the argument of latitude.

The relative effect of the Earth oblateness due to J_2 then becomes

$$\Delta \mathbf{a}_{J_2} = \mathbf{a}_{J_2}(r_c, i_c, \theta_c) - \mathbf{a}_{J_2}(r_t, i_t, \theta_t) \quad (7)$$

The radius, inclination and the argument of latitude of the target are assumed to be known from the onboard navigation system of the target vehicle. The radius, inclination, and the argument of latitude of the chaser are then used to relate the position and velocity vectors through [87]

$$\begin{aligned} \mathbf{r}_c &= \mathbf{r}_t + C^T \boldsymbol{\rho} \\ \mathbf{v}_c &= \mathbf{v}_t + C^T \tilde{\boldsymbol{\omega}} \boldsymbol{\rho} + C^T \dot{\boldsymbol{\rho}} \end{aligned} \quad (8)$$

where C is the 3-1-3 rotation sequence $C = C_3(\theta_c)C_1(i_c)C_3(\Omega_c)$, $\boldsymbol{\rho}$ is the relative position, and $\dot{\boldsymbol{\rho}}$ is the relative velocity. The $\tilde{\boldsymbol{\omega}}$ term is the cross product matrix. The perturbing acceleration in the CW frame due to aerodynamic drag is computed by expressing the acceleration in terms of the ECI frame [84], [85] as

$$\mathbf{a}_{air\ drag} = -\frac{1}{2} \rho \left(\frac{c_D A}{m} \right) \|\mathbf{v}_{rel}\| \mathbf{v}_{rel} \quad (9)$$

where ρ is the atmospheric density and often a difficult parameter to determine. The ballistic coefficient BC is $c_D A/m$, another measure of a spacecraft susceptibility to drag effects and its value is assumed to be known for the simulations conducted in this study,

and \mathbf{v}_{rel} is the velocity vector relative to the rotating atmosphere. An exponential model is adopted to determine ρ . The velocity relative to the rotating atmosphere is [84]

$$\mathbf{v}_{rel} = \dot{\mathbf{r}} - \tilde{\omega}_{\oplus} \mathbf{r} = \begin{bmatrix} \dot{X} + \omega_{\oplus} Y & \dot{Y} - \omega_{\oplus} X & \dot{Z} \end{bmatrix} \quad (10)$$

where $\tilde{\omega}_{\oplus}$ is the cross product matrix of the Earth rotation vector, and X, Y, Z and $\dot{X}, \dot{Y}, \dot{Z}$ are the position and velocity respectively in the ECI frame. The relative effect of atmospheric drag in the CW frame is then

$$\Delta \mathbf{a}_{air\ drag} = C(\mathbf{a}_{air\ drag}(\mathbf{r}_c, \mathbf{v}_c, BC_c) - \mathbf{a}_{air\ drag}(\mathbf{r}_t, \mathbf{v}_t, BC_t)) \quad (11)$$

in which drag is computed for both the chaser and the target spacecraft. Thus, the sum of the relative effect of Earth oblateness and drag becomes

$$\Delta \mathbf{a} = \Delta \mathbf{a}_{J_2} + \Delta \mathbf{a}_{air\ drag} \quad (12)$$

Consequently, the equations of motion for the translational control formulation become

$$\begin{aligned} \ddot{x} - 2\dot{f} \left(\dot{y} - y \frac{\dot{r}_t}{r_t} \right) - x\dot{f}^2 - \frac{\mu}{r_t^2} &= -\frac{\mu}{r_c^3} (r_t + x) + \frac{F_x}{m(t)} + \Delta \mathbf{a}_x \\ \ddot{y} + 2\dot{f} \left(\dot{x} - x \frac{\dot{r}_t}{r_t} \right) - y\dot{f}^2 &= -\frac{\mu}{r_c^3} y + \frac{F_y}{m(t)} + \Delta \mathbf{a}_y \\ \ddot{z} &= -\frac{\mu}{r_c^3} z + \frac{F_z}{m(t)} + \Delta \mathbf{a}_z, \quad r_c = \sqrt{(r_t + x)^2 + y^2 + z^2} \end{aligned} \quad (13)$$

4.3. ROTATIONAL MOTION DYNAMICS AND KINEMATICS

The rotational motion of the chaser is expressed in the body-fixed frame using the well-known Euler's equations of motion. Like the perturbing accelerations in relative translational dynamics, rotational dynamics also experience disturbing torques such as

torque due to aerodynamic drag, magnetic field torque, and gravity-gradient torque due to asymmetry of spacecraft. This study models only the gravity-gradient torque. The effects of the gravitational field are not uniform over an arbitrarily shaped body in space, creating a gravitational torque about the body's center of mass. This gravity-gradient torque, expressed using the local orbital frame A , is given in vector/dyadic form as [83], [86]

$$\mathbf{T}_g = 3 \frac{\mu}{r_c^3} \mathbf{a}_z \times I \cdot \mathbf{a}_z \quad (14)$$

where I is the inertia matrix of the chaser spacecraft. The orientation of the body-fixed frame B of the chaser with respect to the spacecraft local orbital frame A of the chaser is described by the direction cosine matrix $C^{B/A}$ as

$$\begin{bmatrix} \mathbf{b}_x \\ \mathbf{b}_y \\ \mathbf{b}_z \end{bmatrix} = \begin{bmatrix} C_{11}^{B/A} & C_{12}^{B/A} & C_{13}^{B/A} \\ C_{21}^{B/A} & C_{22}^{B/A} & C_{23}^{B/A} \\ C_{31}^{B/A} & C_{32}^{B/A} & C_{33}^{B/A} \end{bmatrix} \begin{bmatrix} \mathbf{a}_x \\ \mathbf{a}_y \\ \mathbf{a}_z \end{bmatrix} \quad (15)$$

The orientation of the local orbital frame A of the target spacecraft with respect to the CW frame C is described by the direction cosine matrix $C^{A/C}$ such that

$$\begin{bmatrix} \mathbf{a}_1 \\ \mathbf{a}_2 \\ \mathbf{a}_3 \end{bmatrix} = C^{A/C} \begin{bmatrix} \mathbf{e}_x \\ \mathbf{e}_y \\ \mathbf{e}_z \end{bmatrix} = \begin{bmatrix} 0 & 1 & 0 \\ 0 & 0 & -1 \\ -1 & 0 & 0 \end{bmatrix} \begin{bmatrix} \mathbf{e}_x \\ \mathbf{e}_y \\ \mathbf{e}_z \end{bmatrix} \quad (16)$$

The direction cosine matrix $C^{B/A}$ can be expressed using successive rotations with the inertial frame N through Eq. (17) as

$$C^{B/A} = C^{B/N} C^{N/A} \quad (17)$$

The angular velocity of the chaser, $\boldsymbol{\omega} = \boldsymbol{\omega}^{B/N}$, and \mathbf{a}_z can be expressed in terms of the basis vector of the body-fixed frame B of the chaser as

$$\boldsymbol{\omega} = \omega_1 \mathbf{b}_x + \omega_2 \mathbf{b}_y + \omega_3 \mathbf{b}_z \quad (18)$$

$$\mathbf{a}_z = C_{13}^{B/A} \mathbf{b}_x + C_{23}^{B/A} \mathbf{b}_y + C_{33}^{B/A} \mathbf{b}_z \quad (19)$$

The gravity-gradient torque matrix becomes

$$\mathbf{T}_g = 3 \frac{\mu}{r_c^3} \begin{bmatrix} 0 & -C_{33}^{B/A} & C_{23}^{B/A} \\ C_{33}^{B/A} & 0 & -C_{13}^{B/A} \\ -C_{23}^{B/A} & C_{13}^{B/A} & 0 \end{bmatrix} \begin{bmatrix} I_{11} & I_{12} & I_{13} \\ I_{21} & I_{22} & I_{23} \\ I_{31} & I_{32} & I_{33} \end{bmatrix} \begin{bmatrix} C_{13}^{B/A} \\ C_{23}^{B/A} \\ C_{33}^{B/A} \end{bmatrix} \quad (20)$$

A full description of the rotational motion of a rigid spacecraft requires both kinematic and dynamic equations of motion. For most modern spacecraft applications, quaternion kinematics [88-90] is preferred. The quaternion kinematic equations of the chaser is

$$\dot{\mathbf{q}} = \frac{1}{2} \Xi(\mathbf{q}) \boldsymbol{\omega} = \frac{1}{2} \Omega(\boldsymbol{\omega}) \mathbf{q} \quad (21)$$

where

$$\Xi(\mathbf{q}) = \begin{bmatrix} q_4 I_{3 \times 3} + [\boldsymbol{\rho} \times] \\ -\boldsymbol{\rho}^T \end{bmatrix}, \quad \Omega(\boldsymbol{\omega}) = \begin{bmatrix} -[\boldsymbol{\omega} \times] & \boldsymbol{\omega} \\ -\boldsymbol{\omega}^T & 0 \end{bmatrix} \quad (22)$$

The adopted quaternion [88] is defined by

$$\mathbf{q} = [\boldsymbol{\rho}^T \quad q_4]^T \quad (23)$$

where $\boldsymbol{\rho}$ is defined as $[q_1 \quad q_2 \quad q_3]^T = \mathbf{e} \sin(\vartheta/2)$, and $q_4 = \cos(\vartheta/2)$, where \mathbf{e} is the axis of rotation and ϑ is the angle of rotation. Euler's rotational equation of motion, including the gradient torque, is given by

$$\dot{\boldsymbol{\omega}} = -I^{-1}\tilde{\boldsymbol{\omega}}I\boldsymbol{\omega} + I^{-1}(\mathbf{T}_g + \mathbf{T}_d) + I^{-1}(\mathbf{T}_u) \quad (24)$$

where \mathbf{T}_u is the applied control torque and \mathbf{T}_d is the external disturbance torque which is modeled by white Gaussian-noise.

5. GUIDANCE FUNCTION

The Guidance function provides both translational and rotational guidance. The guidance for translational maneuvering determines commands designed to bring the chaser to a desired velocity. An automated terminal guidance scheme based on the CW state transition matrix is used to provide the reference trajectory for the closing transfer composed of three V-bar hops. This guidance scheme is also used to determine the transfer time and required ΔV in the closing phase. The general solution can be conveniently expressed in terms of the state vector as

$$\delta \mathbf{s}^T(t) = [\delta \mathbf{r}^T(t) \quad \delta \mathbf{v}^T(t)] = [x \quad y \quad z \quad \dot{x} \quad \dot{y} \quad \dot{z}] \quad (25)$$

by means of its 6×6 state transition matrix $\Phi(t)$ for which

$$\delta \mathbf{s}(t) = \Phi(t) \delta \mathbf{s}(0) \quad (26)$$

The state transition matrix for the CW equations [60-62] is

$$\Phi(t) = \begin{bmatrix} 4 - 3\cos n(t) & 0 & 0 & \frac{\sin n(t)}{n} & \frac{2}{n}(1 - \cos n(t)) & 0 \\ 6(\sin n(t) - nt) & 1 & 0 & -\frac{2}{n}(1 - \cos n(t)) & \frac{4\sin n(t) - 3\cos n(t)}{n} & 0 \\ 0 & 0 & \cos n(t) & 0 & 0 & \frac{\sin n(t)}{n} \\ 3n\sin n(t) & 0 & 0 & \cos n(t) & 2\sin n(t) & 0 \\ 6n(1 - \cos n(t)) & 0 & 0 & -2\sin n(t) & 4\cos n(t) - 3 & 0 \\ 0 & 0 & -n\sin n(t) & 0 & 0 & \cos n(t) \end{bmatrix} \quad (27)$$

where n is the mean motion of the target. The state transition matrix $\Phi(t)$ is partitioned into four 3×3 partitions as

$$\Phi(t) = \begin{bmatrix} M(t) & N(t) \\ S(t) & T(t) \end{bmatrix} \quad (28)$$

The necessary velocity to intercept the target at the initial time is obtained by [60], [61] as

$$\delta \mathbf{v}(0) = N(t_f)(\delta \mathbf{r}_d(t_f) - M(t_f)\delta \mathbf{r}(t_0)) \quad (29)$$

where $\delta \mathbf{r}_d(t_f)$ is the desired final location, $\delta \mathbf{r}(t_0)$ is the initial location and t_f is the transfer maneuver time. The reference state is propagated using Eq. (26) and Eq. (29). As the closing transfer time is made shorter, the approach velocity to S3 becomes higher. After the closing transfer reaches S3, stationkeeping then is performed for four minutes and is again performed at S41. The required time was predetermined using the exponential braking law and control techniques. This setting time can be varied to accommodate the autonomy of the GNC system if a longer time is required to stabilize the stationkeeping phase. When the stationkeeping phase is stabilized, the chaser vehicle follows bounded relative motion in three-dimensional spaces. The stationkeeping phases at S3 and S41 maintain the desired constant position and zero velocity. Since the vehicle has approach velocity at S3 along the $-\mathbf{R}$ -bar direction, retro-firing of thrusters is required. To nullify the approach velocity, the exponential braking law [63], characterized by an exponential change of velocity with time of type, is given as

$$\mathbf{v}(t) = \dot{X}_0 \mathbf{e}^{\left(-\frac{t-t_0}{\lambda}\right)} \quad (30)$$

where \dot{X}_0 is the initial range rate and λ is a tuned proportionality parameter. After the stationkeeping phases, two straight line forced motion trajectories are used for the \mathbf{V} -bar final approach with constant velocity from S4 to S41 and from S41 to the docking port. In this type of trajectory a constant relative velocity of V_x with respect to the target is maintained between x_0 and x_1 , with the velocity along the other directions zero. The basic equation for $x(t)$ along the \mathbf{V} -bar direction is given by

$$x(t) = x_0 + V_x t \quad (31)$$

where $x(t)$ at the terminal time becomes zero.

The rotational maneuver guidance is provided by onboard navigation and a local communication link. The quaternion, angular rate and angular acceleration become the chaser's desired ones to track for the required attitude alignment.

6. NAVIGATION FUNCTION

The navigation system is designed to satisfy the critical requirements for proximity operations and docking. It provides the estimated relative position and velocity for use in determining translational maneuvers, and absolute and relative attitudes for computing the rotational maneuvers. When transitioning from one phase to another along the approach, navigation sensor systems for the translational and rotational maneuvers are changed. The RELAVIS scanning system is used to estimate the relative position and velocity for the translational maneuvers executed from S2 to S4. Star trackers and three axis rate-integrating gyros are used to estimate the chaser absolute attitude for the rotational maneuvers executed from S2 to S4. The vision-based navigation (VISNAV) system is activated at S4 in place of the RELAVIS scanning system and the star trackers and three axis rate-integrating gyros to provide more accurate and more reliable state estimation. When the star trackers and gyros that estimate the absolute attitude of the chaser are replaced by the vision sensor, the relative quaternions between the target and chaser provided by the VISNAV system are transformed to the absolute quaternions using the quaternion product. The Navigation function uses a set of EKF filters whose general algorithm order is altered to process “the update” earlier than “the propagation” in the filter algorithm. Then the EKF can be stabilized earlier if the quality of the measurement is good.

In order to investigate the potential benefit of using a UKF filter, this study included simulations (separate from the GNC system) using a UKF filter subjected to realistic initial conditions and initial errors to compare to the use of the EKF filter.

6.1. NONLINEAR SYSTEM STATE ESTIMATION

The Extended Kalman Filter (EKF) has been widely used in state estimation. The EKF is based on the approximation of the state distribution as a Gaussian random variable (GRV) and the propagation of the approximation through first-order linearization of the nonlinear system. The EKF is a suboptimal filter due to the truncation of the higher-order terms when linearizing the system. This truncation can cause large errors in the true posterior mean and covariance of the transformed GRV, which may lead to

suboptimal performance and sometimes divergence of the filter. The EKF may not cope very well with realistic initial conditions leading to filter divergence. Alternatives that avoid the loss of higher-order terms are the unscented Kalman filter and the Particle Filter. In this study, the UKF is applied to state estimation, providing a robust filter under realistic initial conditions. The UKF is an extension of the traditional Kalman filter. It estimates nonlinear systems and performs the unscented transformation. The unscented transformation uses a set sample, or sigma points, that are determined from the *a priori* mean and covariance of the state. The sigma points completely capture the true mean and covariance of the GRV, and when propagated through the true nonlinear system, they capture the posterior mean and covariance accurately to third-order of the Taylor series expansion for any nonlinearity. The ability of the UKF to estimate nonlinearities accurately makes it attractive for spacecraft relative attitude estimation and navigation, as the state and observation models of spacecraft relative attitude estimation and navigation are of course inherently nonlinear.

6.1.1. Extended Kalman Filter Description. [64-77] The RELAVIS scanning system and the VISNAV system involve nonlinear continuous-time state and discrete-time measurements collected by a digital signal processor. The nonlinear system equation and measurement equation are represented by [64], [67] as

$$\dot{\mathbf{x}}(t) = \mathbf{f}(\mathbf{x}(t), u(t), t) + G(t)\mathbf{w}(t) \quad (32)$$

$$\tilde{\mathbf{Y}}_k = \mathbf{h}(\mathbf{x}_k, t_k) + \mathbf{v}_k \quad (33)$$

where $u(t)$ is the control input which is a deterministic quantity. Process noise $\mathbf{w}(t)$ and measurement noise \mathbf{v}_k are zero mean Gaussian noise process with covariances given by

$$E\{\mathbf{w}(t)\} = 0, \quad E\{\mathbf{w}(t)\mathbf{w}(t)^T\} = Q(t)\delta(t - \tau) \quad (34)$$

$$E\{\mathbf{v}_k(t)\} = 0, \quad E\{\mathbf{v}_k(t)\mathbf{v}_l(t)^T\} = R(t)\delta_{kl} \quad (35)$$

$$E\{\mathbf{v}(t)\mathbf{w}^T(\tau)\} = 0 \quad (36)$$

Equation (36) implies that $\mathbf{v}(t)$ and $\mathbf{w}(t)$ are uncorrelated. The structure of the EKF filter can be divided into two primary parts, propagation and update. The state estimation and error covariance matrix equation are propagated forward in time until a measurement occurs by numerically integrating

$$\dot{\hat{\mathbf{x}}}(t) = \mathbf{f}(\hat{\mathbf{x}}(t), u(t), t) \quad (37)$$

$$\dot{P}(t) = F(t)P(t) + P(t)F^T(t) + G(t)Q(t)G^T(t) \quad (38)$$

where $F(t)$ is the sensitivity matrix of the state equation with respect to the best current estimate

$$F(t) = \left[\frac{\partial \mathbf{f}}{\partial \mathbf{x}} \right]_{\hat{\mathbf{x}}(t)} \quad (39)$$

Given the new measurement at time t_k , the state and covariance can be updated using

$$\hat{\mathbf{x}}_k^+ = \hat{\mathbf{x}}_k^- + K_k [\tilde{\mathbf{Y}}_k - \mathbf{h}(\hat{\mathbf{x}}_k^-)] \quad (40)$$

$$P_k^+ = (I - K_k H_k(x_k^-)) P_k^- \quad (41)$$

where H_k is the sensitivity matrix of the measurement equations

$$H_k = \left[\frac{\partial \mathbf{h}}{\partial \mathbf{x}} \right]_{\hat{\mathbf{x}}_k^-} \quad (42)$$

The subscripts “+” and “-” denote the estimate after the measurement update and the propagated state at the update time, respectively. The optimal Kalman gain K_k can be determined that minimizes the norm of the estimation error and is equivalent to minimizing the trace of the error covariance P_k^+

$$\text{Min } J(K_k) = \text{Trace} \left[E \left\{ \left(\hat{\mathbf{x}}_k^+ - \hat{\mathbf{x}}_k^- \right) \left(\hat{\mathbf{x}}_k^+ - \hat{\mathbf{x}}_k^- \right)^T \right\} \right] = \text{Trace}(P_k^+) \quad (43)$$

The optimal Kalman gain K_k is then determined as

$$K_k = P_k^- H_k^T \left[H_k P_k^- H_k^T + R_k \right]^{-1} \quad (44)$$

A summary of the continuous-discrete extended Kalman filter is given in Table 6.1.

Table 6.1. Continuous-Discrete Extended Kalman Filter.

Model	$\dot{\mathbf{x}}(t) = \mathbf{f}(\mathbf{x}(t), u(t), t) + G(t)\mathbf{w}(t), \mathbf{w}(t) \sim N(\mathbf{0}, Q(t))$ $\tilde{\mathbf{Y}}_k = \mathbf{h}(\mathbf{x}_k) + \mathbf{v}_k, \mathbf{v}_k \sim N(\mathbf{0}, R_k)$
Initialize	$\hat{\mathbf{x}}(t_0) = \hat{\mathbf{x}}_0$ $P_0 = E \left\{ (\mathbf{x}(t_0) - \hat{\mathbf{x}}_0)(\mathbf{x}(t_0) - \hat{\mathbf{x}}_0)^T \right\}$
Gain	$K_k = P_k^- H_k^T \left[H_k P_k^- H_k^T + R_k \right]^{-1}$ $H_k = \left[\frac{\partial \mathbf{h}}{\partial \mathbf{x}} \right]_{\hat{\mathbf{x}}_k^-}$
Update	$\hat{\mathbf{x}}_k^+ = \hat{\mathbf{x}}_k^- + K_k \left[\tilde{\mathbf{Y}}_k - \mathbf{h}(\hat{\mathbf{x}}_k^-) \right]$ $P_k^+ = (I - K_k H_k(x_k^-)) P_k^-$
Propagation	$\dot{\hat{\mathbf{x}}}(t) = \mathbf{f}(\hat{\mathbf{x}}(t), u(t), t)$ $\dot{P}(t) = F(t)P(t) + P(t)F^T(t) + G(t)Q(t)G^T(t)$ $F(t) = \left[\frac{\partial \mathbf{f}}{\partial \mathbf{x}} \right]_{\hat{\mathbf{x}}(t)}$

6.1.2. Unscented Kalman Filter Description. [91-97] In this section the UKF filter is reviewed. Many difficulties in implementing the EKF filter arise from its use of linearization of the nonlinear system. To overcome the disadvantages of the EKF, the UKF filter uses an unscented transformation. Unlike the EKF, the UKF filter does not require Jacobian and Hessian computations. Rather, the UKF uses a minimal set of sigma points deterministically chosen from the error covariance and propagated through the true nonlinear system to capture the posterior mean and covariance of the Gaussian random variable accurately to third order of the Taylor series expansion for any nonlinearity. Consider the discrete-time system model of nonlinear equations

$$\mathbf{x}_{k+1} = \mathbf{f}(x_k, k) + G_k \mathbf{w}_k \quad (45)$$

$$\mathbf{y}_k = \mathbf{h}_k(\mathbf{x}_k, k) + \mathbf{v}_k \quad (46)$$

where \mathbf{x}_k is the $n \times 1$ state vector and \mathbf{y}_k is the $m \times 1$ observation vector. Note that a continuous time model can always be expressed in the form of Eq. (45) through an appropriate numerical integration scheme. The process noise vector \mathbf{w}_k and observation noise vector \mathbf{v}_k are assumed to be zero-mean and white Gaussian noise, and the covariance of these vectors is given by Q_k and R_k , respectively. From the $n \times n$ covariance P_k , the set of $(2n+1)$ sigma points $\boldsymbol{\chi}_k \in \mathcal{R}^{2n+1}$ can be generated by the columns of the matrices $\sqrt{(n+\lambda)P_k}$. The general formulation for the propagation equations begins with a set of sigma points with corresponding weights W_i , according to

$$\boldsymbol{\chi}_k(0) = \hat{\mathbf{x}}_k \quad (47a)$$

$$\boldsymbol{\chi}_k(i) = \hat{\mathbf{x}}_k + \left(\gamma \sqrt{(P_k + Q_k)} \right)_i \quad \text{for } i = 1, \dots, n \quad (47b)$$

$$\boldsymbol{\chi}_k(i) = \hat{\mathbf{x}}_k - \left(\gamma \sqrt{(P_k + Q_k)} \right)_i \quad \text{for } i = n+1, \dots, 2n \quad (47c)$$

$$W_0 = \frac{\lambda}{(n+\lambda)} \quad (48a)$$

$$W_i = \frac{1}{\{2(n + \lambda)\}} \quad i = 1, \dots, 2n \quad (48b)$$

where the matrix \bar{Q}_k is related to the process noise covariance and was defined in the previous section. Note $\gamma = \sqrt{n + \lambda}$ and λ are convenient parameters for exploiting whatever knowledge is available from the higher moments of the given distribution. In scalar systems, where $n = 1$, a value of $\lambda = 2$ leads to sixth order errors in mean and variance. For higher dimensional systems, choosing $\lambda = 3 - n$ minimizes the mean-squared-error up to the fourth order [92], [93]. However, caution is required when λ is negative since the predicted covariance may become a positive semi-definite covariance matrix. Also, when $n + \lambda$ tends to zero, the mean tends to that calculated by the truncated second-order filter. The matrix square root $\sqrt{(P_k + \bar{Q}_k)}$ can be calculated by a lower triangular Cholesky factorization [94-97]. From Eq. (44), a matrix χ_k of $2n+1$ sigma vectors $\chi_{i,k}$ is formed as

$$\chi_k = \left[\hat{\mathbf{x}}_k \quad \hat{\mathbf{x}}_k + \gamma \sqrt{(P_k + \bar{Q}_k)} \quad \hat{\mathbf{x}}_k - \gamma \sqrt{(P_k + \bar{Q}_k)} \right] \quad (49)$$

The transformed set of sigma points is evaluated for each of the points by

$$\chi_{k+1}(i) = \mathbf{f}(\chi_k(i), k) \quad (50)$$

where $\chi_{k+1}(i)$ is the i^{th} column of χ_k . The predicted mean $\hat{\mathbf{x}}_{k+1}^-$ and predicted covariance P_{k+1}^- are computed using a weighted sample mean and covariance of the posterior sigma point vectors as

$$\mathbf{x}_{k+1}^-(i) = \sum_{i=0}^{2n} W_i \chi_{k+1}(i) \quad (51)$$

where W_i is the weighting coefficient and

$$P_{k+1}^- = \sum_{i=0}^{2n} W_i \{ \boldsymbol{\chi}_{k+1}(i) - \mathbf{x}_{k+1}^-(i) \} \{ \boldsymbol{\chi}_{k+1}(i) - \mathbf{x}_{k+1}^-(i) \}^T + \bar{Q}_k \quad (52)$$

The mean observation is given by

$$\hat{\mathbf{y}}_{k+1}^- = \sum_{i=0}^{2n} W_i \mathbf{Y}_{k+1}(i) \quad (53)$$

where

$$\mathbf{Y}_{k+1}(i) = \mathbf{h}(\boldsymbol{\chi}_{k+1}(i), k+1) \quad (54)$$

The predicted output covariance P_{k+1}^{yy} is given by

$$P_{k+1}^{yy} = \sum_{i=0}^{2n} W_i \{ \mathbf{Y}_{k+1}(i) - \hat{\mathbf{y}}_{k+1}^-(i) \} \{ \mathbf{Y}_{k+1}(i) - \hat{\mathbf{y}}_{k+1}^-(i) \}^T \quad (55)$$

The innovation covariance P_{k+1}^{vv} is then computed by

$$P_{k+1}^{vv} = P_{k+1}^{yy} + R_{k+1} \quad (56)$$

The filter gain K_{k+1} is computed by

$$K_{k+1} = P_{k+1}^{xy} (P_{k+1}^{vv})^{-1} \quad (57)$$

and the cross correlation matrix is given by

$$\mathbf{P}_{k+1}^{xy} = \sum_{i=0}^{2n} W_i \{ \boldsymbol{\chi}_{k+1}(i) - \mathbf{y}_{k+1}(i) \} \{ \boldsymbol{\chi}_{k+1}(i) - \mathbf{y}_{k+1}(i) \}^T \quad (58)$$

The estimated state vector $\hat{\mathbf{x}}_{k+1}^+$ and updated covariance P_{k+1}^+ are given by

$$\hat{\mathbf{x}}_{k+1}^+ = \hat{\mathbf{x}}_{k+1}^- + K_{k+1}(y_{k+1} - \hat{y}_{k+1}^-) \quad (59)$$

$$P_{k+1}^+ = P_{k+1}^- - K_{k+1} P_{k+1}^{vv} K_{k+1}^T \quad (60)$$

A summary of the discrete unscented Kalman filter is given in Table 6.2.

Table 6.2. Discrete Unscented Kalman Filter.

Model	$\mathbf{x}_{k+1} = \mathbf{f}(x_k, k) + G_k \mathbf{w}_k, \mathbf{w}(t) \sim N(\mathbf{0}, Q(t))$ $\mathbf{y}_k = \mathbf{h}_k(\mathbf{x}_k, k) + \mathbf{v}_k, \mathbf{v}_k \sim N(\mathbf{0}, R_k)$
Initialize	$\hat{\mathbf{x}}_0 = E\{\hat{\mathbf{x}}_0\}$ $P_0 = P_k$ <p>Calculate sigma points:</p> $\boldsymbol{\chi}_k(i) = \hat{\mathbf{x}}_k + \left(\gamma \sqrt{\mathbf{P}_k + \mathbf{Q}_k} \right)_i \quad \text{for } i = 1, \dots, n$ $\boldsymbol{\chi}_k(i) = \hat{\mathbf{x}}_k - \left(\gamma \sqrt{\mathbf{P}_k + \mathbf{Q}_k} \right)_i \quad \text{for } i = n + 1, \dots, 2n$
Time Update	$\boldsymbol{\chi}_{k+1}(i) = \mathbf{f}(\boldsymbol{\chi}_k(i), k)$ $\mathbf{x}_{k+1}^- = \sum_{i=0}^{2n} W_i \boldsymbol{\chi}_{k+1}(i)$ $P_{k+1}^- = \sum_{i=0}^{2n} W_i \left\{ \boldsymbol{\chi}_{k+1}(i) - \mathbf{x}_{k+1}^- \right\} \left\{ \boldsymbol{\chi}_{k+1}(i) - \mathbf{x}_{k+1}^- \right\}^T + \bar{Q}_k$ $\mathbf{Y}_{k+1}(i) = \mathbf{h}(\boldsymbol{\chi}_{k+1}(i), k + 1)$ $\hat{y}_{k+1}^- = \sum_{i=0}^{2n} W_i \mathbf{Y}_{k+1}(i)$

Table 6.2. (Continued)

Measurement Update	$P_{k+1}^{yy} = \sum_{i=0}^{2n} W_i \{ \mathbf{Y}_{k+1}(i) - \hat{\mathbf{y}}_{k+1}^- \} \{ \mathbf{Y}_{k+1}(i) - \hat{\mathbf{y}}_{k+1}^- \}^T$ $P_{k+1}^{vv} = P_{k+1}^{yy} + R_{k+1}$ $P_{k+1}^{xy} = \sum_{i=0}^{2n} W_i \{ \mathbf{X}_{k+1}(i) - \mathbf{y}_{k+1} \} \{ \mathbf{X}_{k+1}(i) - \mathbf{y}_{k+1} \}^T$ $K_{k+1} = P_{k+1}^{xy} (P_{k+1}^{vv})^{-1}$ $\hat{\mathbf{x}}_{k+1}^+ = \hat{\mathbf{x}}_{k+1}^- + K_{k+1} (\mathbf{y}_{k+1} - \hat{\mathbf{y}}_{k+1}^-)$ $P_{k+1}^+ = P_{k+1}^- - K_{k+1} P_{k+1}^{vv} K_{k+1}^T$
---------------------------	---

A simple example is shown in Figure 6.1 for a two-dimensional system: the left hand plot shows the true mean and covariance propagation using Monte-Carlo sampling; the center plots show the results using a linearization approach as would be done in the EKF filter; and the right-hand plots show the performance of the unscented transformation (note only five sigma points are required). The superior performance of the unscented transformation is clear.

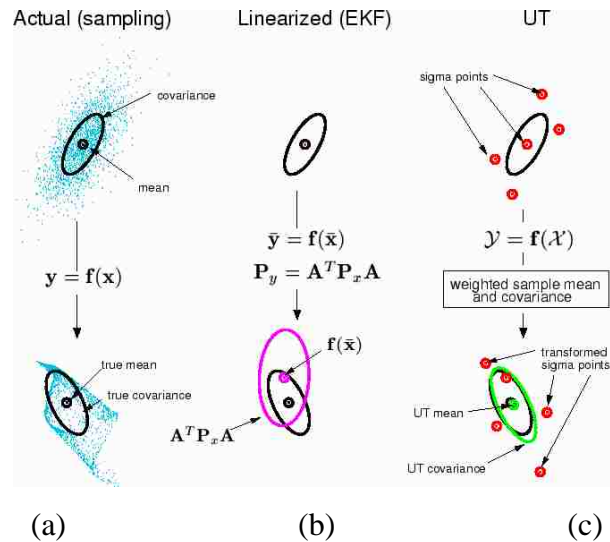


Figure 6.1. Example of the UT for Mean and Covariance Propagation. a) Actual, b) First-Order Linearization (EKF), c) UT. (Figure Taken from Reference [95])

6.2 RELAVIS SCANNING SYSTEM-BASED RELATIVE STATE ESTIMATION USING THE EXTENDED KALMAN FILTER

6.2.1 LIDAR Measurements. The RELAVIS scanning system also has the unique capability of producing highly accurate measurements over a range of 0.5 m to 5 km, providing range and bearing (azimuth and elevation angles) of the target with centimeter-level accuracy in range and about 0.02 degree in bearing [30-33]. The sensor specifications are shown in Table 1. The range, bearing accuracies, and FOV in Table 1 are of particular interest. It is important to note that the range accuracy is largely independent of the range itself unlike the traditional LIDAR sensor [30-33]. However, the navigation solution accuracy can improve since the bearing measurement yields a better knowledge of the target three-dimensional position as the two vehicles get closer. Laser range finder types of sensors have a limited FOV. Since the closing transfer in the original ATV program exceeds the FOV constraint in Table 6.3, the use of RELVIS would not be appropriate. In order to facilitate the use of RELVIS, the one-hop V-bar approach in the closing transfer is modified to three hops using the CW terminal guidance so that the nominal approach trajectory does meet the FOV constraint. The minimum and maximum ranges can cover the ranges between S2 and S4, respectively.

Table 6.3. RELAVIS LIDAR Sensor Specifications (Optech Inc.) [30-33].

Minimum range	0.5 m
Maximum range	5 km
Mass	Less than 15 kg
Volume	Less than 9 liters
Field of View	20 × 20 degrees
Maximum data sensing rate	8-10 kHz
Range Accuracy	1 cm
Bearing Accuracy	0.35 mrad
Power Consumption	Less than 125 W

The measurement errors are simulated as white Gaussian noise with zero mean. The bias error is not included since the error is relatively small and is ignored compared to the random errors. As the two vehicles get closer, the bearing error actually decreases, however, a constant bearing error is conservatively adopted in this study. The range-angles measurement model consisting of range, azimuth and elevation angles is defined as

$$\begin{aligned}
 r &= \sqrt{x^2 + y^2 + z^2} \\
 Az &= \tan^{-1}\left(\frac{y}{x}\right) \\
 El &= \tan^{-1}\left(\frac{z}{\sqrt{x^2 + y^2}}\right) = \sin^{-1}\left(\frac{z}{r}\right)
 \end{aligned} \tag{61}$$

The measurement vector at t_k is then given as

$$\mathbf{Y}_k(\mathbf{X}, t) = \begin{bmatrix} \sqrt{x^2 + y^2 + z^2} \\ \tan^{-1}\left(\frac{y}{x}\right) \\ \tan^{-1}\left(\frac{y}{\sqrt{x^2 + y^2}}\right) \end{bmatrix}_{t_k} + \boldsymbol{\varepsilon}_k \tag{62}$$

where $\boldsymbol{\varepsilon}_k$ is the measurement error vector. The errors are simulated as zero mean Gaussian noise.

6.2.2. Relative Position and Velocity Estimation. An EKF filter is used to sequentially estimate the relative position and velocity using the RELAVIS scanning system. The order of a conventional EKF algorithm is modified so that measurement updates are processed first. The state vector is defined as

$$\mathbf{X} = [x \quad y \quad z \quad \dot{x} \quad \dot{y} \quad \dot{z}]^T \tag{63}$$

The partial derivative matrix for the nonlinear state-space model in Eq. (13), omitting the relative perturbation terms for simplicity, is given as

$$F(\hat{\mathbf{X}}(t), t) = \begin{bmatrix} 0 & 0 & 0 & 1 & 0 & 0 \\ 0 & 0 & 0 & 0 & 1 & 0 \\ 0 & 0 & 0 & 0 & 0 & 1 \\ \dot{f}^2 + \frac{3\mu(r_t + x)^2}{r_c^5} - \frac{\mu}{r_c^3} & -2\dot{f} \frac{\dot{r}_t}{r_t} + \frac{3\mu y(r_t + x)}{r_c^5} & \frac{3\mu z(r_t + x)}{r_c^5} & 0 & 0 & 0 \\ 2\dot{f} \frac{\dot{r}_t}{r_t} + \frac{3\mu y^2 y(r_t + x)}{r_c^5} & \dot{f}^2 + \frac{3\mu y^2}{r_c^5} - \frac{\mu}{r_c^3} & \frac{3\mu yz}{r_c^5} & -2\dot{f} & 0 & 0 \\ \frac{3\mu z(r_t + x)}{r_c^5} & \frac{3\mu yz}{r_c^5} & \frac{3\mu z^2}{r_c^5} - \frac{\mu}{r_c^3} & 0 & 0 & 0 \end{bmatrix} \quad (64)$$

where the “hat” symbol “^” denotes the estimated state. Then the nonlinear state-space model follows Eq. (13). The error covariance for the system process noise is given by

$$Q = \text{diag}[0 \quad 0 \quad 0 \quad w_x^2 \quad w_x^2 \quad w_z^2] \quad (65)$$

where w_x, w_y and w_z are system process noise. The matrices F and Q are used for covariance propagation. By taking the partial derivative of the measurement vector, the measurement sensitivity matrix at t_k is given by

$$H_k(\hat{\mathbf{X}}_k) = \begin{bmatrix} \frac{x}{r} & \frac{y}{r} & \frac{z}{r} & 0 & 0 & 0 \\ -\frac{y}{\sqrt{x^2 + y^2}} & \frac{x}{\sqrt{x^2 + y^2}} & 0 & 0 & 0 & 0 \\ -\frac{xz}{r^2 \sqrt{x^2 + y^2}} & -\frac{yz}{r^2 \sqrt{x^2 + y^2}} & \frac{\sqrt{x^2 + y^2}}{r^2} & 0 & 0 & 0 \end{bmatrix}_{t_k} \quad (66)$$

The EKF filter using the RELAVIS scanning system can now be executed with these quantities to estimate the relative attitude, position and velocity.

6.3. ABSOLUTE ATTITUDE ESTIMATION USING STAR TRACKERS AND GYROSCOPES

6.3.1. Star Tracker Measurements. The sensors used here include three axis gyroscopes (gyros) and star trackers whose output is the attitude quaternion referenced to J2000 inertial coordinates. The noise parameters for the gyro measurements were given in the previous section as the chaser's gyro measurements. A combined quaternion from two star trackers is used as the measurement. To generate synthetic measurements, the following model [67]

$$\mathbf{q}_m = \begin{bmatrix} 0.5\mathbf{v} \\ 1 \end{bmatrix} \otimes \mathbf{q} \quad (67)$$

is used where \otimes denotes quaternion multiplication. This work adopts the convention of Lefferts, Markley, and Shuster [88] who multiply the quaternions in the same order as the attitude matrix multiplication. The variable \mathbf{q}_m is the quaternion measurement, \mathbf{q} is the truth, and \mathbf{v} is the measurement noise, which is assumed to be a zero-mean Gaussian noise process with covariance of $0.001I_{3 \times 3} \text{ deg}^2$. The measured quaternion is normalized to ensure a normalized measurement. An error quaternion between the measured quaternion and the estimated quaternion is used for measurement in the filter. This is computed using the error quaternion

$$\delta\mathbf{q} = \begin{bmatrix} \delta\mathbf{p} \\ \delta q_4 \end{bmatrix} = \mathbf{q}_m \otimes \mathbf{q}_e^{-1} \quad (68)$$

where \mathbf{q}_e is the estimated quaternion of the chaser spacecraft. For small angles the vector portion of the quaternion is approximately equal to half angles so that $\delta\mathbf{p} \approx \boldsymbol{\alpha}/2$ and

$\delta q_4 = 1$. The spacecraft desired motion includes a constant angular velocity given as $\omega_d = [0 \ n \ 0]^T$ rad/sec where n is mean motion corresponding to Earth-pointing spacecraft in low-Earth orbit such as the ISS [67].

6.3.2 Absolute Attitude Estimation [67]. An EKF filter is used to estimate the attitude and the rate of the chaser vehicle using star trackers and three-axis strapdown gyroscopes. The EKF filter for attitude estimation begins with the quaternion kinematic model in Eq. (21). A multiplicative error quaternion in the body-fixed frame is given as

$$\delta \mathbf{q} = \mathbf{q} \otimes \hat{\mathbf{q}}^{-1} \quad (69)$$

with $\delta \mathbf{q} = [\delta \mathbf{p}^T \ \delta q_4]^T$. Also, the quaternion inverse is defined by

$$\mathbf{q}^{-1} = [-\mathbf{p} \ q_4] \quad (70)$$

Taking the time derivative of Eq. (69) gives

$$\delta \dot{\mathbf{q}} = \dot{\mathbf{q}} \otimes \hat{\mathbf{q}}^{-1} + \mathbf{q} \otimes \dot{\hat{\mathbf{q}}}^{-1} \quad (71)$$

The estimated quaternion kinematics model is

$$\dot{\hat{\mathbf{q}}} = \frac{1}{2} \Xi(\hat{\mathbf{q}}) \hat{\boldsymbol{\omega}} = \frac{1}{2} \Omega(\hat{\boldsymbol{\omega}}) \hat{\mathbf{q}} \quad (72)$$

Taking the time derivative of $\hat{\mathbf{q}} \otimes \hat{\mathbf{q}}^{-1} = [0 \ 0 \ 0 \ 1]^T$ gives

$$\dot{\hat{\mathbf{q}}} \otimes \hat{\mathbf{q}}^{-1} + \hat{\mathbf{q}} \otimes \dot{\hat{\mathbf{q}}}^{-1} = \mathbf{0} \quad (73)$$

Substituting Eq. (72) into Eq. (73) gives

$$\frac{1}{2}\Omega(\hat{\boldsymbol{\omega}})\hat{\mathbf{q}} \otimes \hat{\mathbf{q}}^{-1} + \hat{\mathbf{q}} \otimes \dot{\hat{\mathbf{q}}}^{-1} = \mathbf{0} \quad (74)$$

Using the definition of $\Omega(\hat{\boldsymbol{\omega}})$ in Eq. (22) and $\hat{\mathbf{q}} \otimes \hat{\mathbf{q}}^{-1} = [0 \ 0 \ 0 \ 1]^T$, Eq. (74) reduces to

$$\frac{1}{2} \begin{bmatrix} \hat{\boldsymbol{\omega}} \\ 0 \end{bmatrix} + \hat{\mathbf{q}} \otimes \dot{\hat{\mathbf{q}}}^{-1} = \mathbf{0} \quad (75)$$

Solving Eq. (75) for $\dot{\hat{\mathbf{q}}}^{-1}$ yields

$$\dot{\hat{\mathbf{q}}}^{-1} = -\frac{1}{2}\hat{\mathbf{q}}^{-1} \otimes \begin{bmatrix} \hat{\boldsymbol{\omega}} \\ 0 \end{bmatrix} \quad (76)$$

Also, a useful identity is given by

$$\dot{\mathbf{q}}^{-1} = \frac{1}{2}\Omega(\boldsymbol{\omega})\mathbf{q} = \frac{1}{2} \begin{bmatrix} \hat{\boldsymbol{\omega}} \\ 0 \end{bmatrix} \otimes \mathbf{q} \quad (77)$$

Substituting Eq. (76) and Eq. (77) into Eq. (71), and using Eq. (69) gives

$$\delta\dot{\mathbf{q}} = \frac{1}{2} \left\{ \begin{bmatrix} \boldsymbol{\omega} \\ 0 \end{bmatrix} \otimes \delta\mathbf{q} - \delta\mathbf{q} \otimes \begin{bmatrix} \hat{\boldsymbol{\omega}} \\ 0 \end{bmatrix} \right\} \quad (78)$$

Define the following error angular velocity as $\delta\boldsymbol{\omega} = \boldsymbol{\omega} - \hat{\boldsymbol{\omega}}$. Substituting $\boldsymbol{\omega} = \delta\boldsymbol{\omega} + \hat{\boldsymbol{\omega}}$ into Eq. (81) leads to

$$\delta\dot{\mathbf{q}} = \frac{1}{2} \left\{ \begin{bmatrix} \hat{\boldsymbol{\omega}} \\ 0 \end{bmatrix} \otimes \delta\mathbf{q} - \delta\mathbf{q} \otimes \begin{bmatrix} \hat{\boldsymbol{\omega}} \\ 0 \end{bmatrix} \right\} + \frac{1}{2} \begin{bmatrix} \delta\boldsymbol{\omega} \\ 0 \end{bmatrix} \otimes \delta\mathbf{q} \quad (79)$$

Next, consider the following useful identities

$$\begin{bmatrix} \hat{\boldsymbol{\omega}} \\ 0 \end{bmatrix} \otimes \delta \mathbf{q} = \Omega(\hat{\boldsymbol{\omega}}) \delta \mathbf{q} \quad (80a)$$

$$\delta \mathbf{q} \otimes \begin{bmatrix} \hat{\boldsymbol{\omega}} \\ 0 \end{bmatrix} = \Gamma(\hat{\boldsymbol{\omega}}) \delta \mathbf{q} \quad (80b)$$

where

$$\Gamma(\hat{\boldsymbol{\omega}}) = \begin{bmatrix} [\boldsymbol{\omega} \times] & \boldsymbol{\omega} \\ -\boldsymbol{\omega}^T & 0 \end{bmatrix} \quad (81)$$

Substituting Eq. (80) into Eq. (79) with some algebraic manipulations leads to

$$\delta \dot{\mathbf{q}} = \frac{1}{2} \begin{bmatrix} [\hat{\boldsymbol{\omega}} \times] \delta \mathbf{q} \\ 0 \end{bmatrix} + \frac{1}{2} \begin{bmatrix} \delta \boldsymbol{\omega} \\ 0 \end{bmatrix} \otimes \delta \mathbf{q} \quad (82)$$

The nonlinear term is present only in the last term on the right-hand side of Eq. (82) and its first-order approximation is given by

$$\frac{1}{2} \begin{bmatrix} \delta \boldsymbol{\omega} \\ 0 \end{bmatrix} \otimes \delta \mathbf{q} \approx \frac{1}{2} \begin{bmatrix} \delta \boldsymbol{\omega} \\ 0 \end{bmatrix} \quad (83)$$

Substituting Eq. (83) into Eq. (82) leads to the linearized model

$$\begin{aligned} \delta \dot{\mathbf{p}} &= -[\hat{\boldsymbol{\omega}} \times] \delta \mathbf{q} + \frac{1}{2} \delta \boldsymbol{\omega} \\ \delta \dot{q}_4 &= 0 \end{aligned} \quad (84)$$

The first-order approximation, which assumes that the true quaternion is “close” to the estimated quaternion, gives $\delta q_4 = 1$. This allows to the reduction of the order of the system in the EKF filter by one state. The linearization using Eq. (69) maintains

quaternion normalization to within first-order if the estimated quaternion is “close” to the true quaternion, which is within the first-order approximation in the EKF filter.

A common sensor that measures the angular rate is a rate-integrating gyroscope. For this sensor, a widely used model is given by

$$\tilde{\boldsymbol{\omega}} = \boldsymbol{\omega} + \boldsymbol{\beta} + \boldsymbol{\eta}_v \quad (85a)$$

$$\dot{\boldsymbol{\beta}} = \boldsymbol{\eta}_u \quad (85b)$$

where $\tilde{\boldsymbol{\omega}}$ is the continuous-time measured angular rate, $\boldsymbol{\beta}$ is the drift rate, and $\boldsymbol{\eta}_v$ and $\boldsymbol{\eta}_u$ are independent zero-mean Gaussian white noise processes with

$$E\{\boldsymbol{\eta}_v(t)\boldsymbol{\eta}_v^T(t)\} = I_{3 \times 3} \sigma_v^2 \delta(t - \tau) \quad (86a)$$

$$E\{\boldsymbol{\eta}_u(t)\boldsymbol{\eta}_u^T(t)\} = I_{3 \times 3} \sigma_u^2 \delta(t - \tau) \quad (86b)$$

where $\delta(t - \tau)$ is the Dirac delta function. The estimated angular velocity is given by

$$\hat{\boldsymbol{\omega}} = \tilde{\boldsymbol{\omega}} - \hat{\boldsymbol{\beta}} \quad (87)$$

Also, the estimated bias differential equation follows as

$$\dot{\hat{\boldsymbol{\beta}}} = \mathbf{0} \quad (88)$$

Substituting Eqs. (85a) and (87) into $\delta\boldsymbol{\omega} = \boldsymbol{\omega} - \hat{\boldsymbol{\omega}}$ gives

$$\delta\boldsymbol{\omega} = -(\Delta\boldsymbol{\beta} + \boldsymbol{\eta}_v) \quad (89)$$

$$\delta\dot{\boldsymbol{p}} = -[\hat{\boldsymbol{\omega}} \times] \delta\boldsymbol{p} - \frac{1}{2}(\Delta\boldsymbol{\beta} + \boldsymbol{\eta}_v) \quad (90)$$

For small angles the vector component of the quaternion is approximately equal to half angles $\delta\mathbf{p} \approx \delta\mathbf{a}/2$, and the scalar part of quaternion is equal to 1. $\delta\mathbf{a}$ has components of roll, pitch, and yaw errors for any rotation sequences. Using this simplification in Eq. (91) gives

$$\delta\ddot{\mathbf{a}} = -[\hat{\boldsymbol{\omega}} \times] \delta\dot{\mathbf{a}} - (\Delta\boldsymbol{\beta} + \boldsymbol{\eta}_v) \quad (91)$$

This approach minimizes the use of the factors 1/2 and 2 in the EKF, and also gives a direct physical meaning to the state error-covariance, which can be used to directly determine the 3σ bounds of the actual attitude errors. The EKF error model is now given by

$$\Delta\dot{\tilde{\mathbf{x}}}(t) = F(\hat{\mathbf{x}}(t), t)\Delta\tilde{\mathbf{x}}(t) + G(t)\mathbf{w}(t) \quad (92)$$

where $\Delta\mathbf{x}(t) = [\delta\mathbf{a}^T \quad \delta\mathbf{p}^T]^T$, $\mathbf{w}(t) = [\boldsymbol{\eta}_v^T(t) \quad \boldsymbol{\eta}_u^T(t)]^T$, $F(\hat{\mathbf{x}}(t), t)$, $G(t)$ and $Q(t)$ are given by

$$F(\hat{\mathbf{x}}(t), t) = \begin{bmatrix} -[\hat{\boldsymbol{\omega}} \times] & -I_{3 \times 3} \\ \mathbf{0}_{3 \times 3} & \mathbf{0}_{3 \times 3} \end{bmatrix} \quad (93a)$$

$$G(t) = \begin{bmatrix} -I_{3 \times 3} & \mathbf{0}_{3 \times 3} \\ \mathbf{0}_{3 \times 3} & I_{3 \times 3} \end{bmatrix} \quad (93b)$$

$$Q(t) = \begin{bmatrix} \sigma_v^2 I_{3 \times 3} & \mathbf{0}_{3 \times 3} \\ \mathbf{0}_{3 \times 3} & \sigma_u^2 I_{3 \times 3} \end{bmatrix} \quad (93c)$$

where the gyro noise parameters are given by $\sigma_u = \sqrt{10} \times 10^{-10}$ rad/sec^{3/2} and $\sigma_v = \sqrt{10} \times 10^{-5}$ rad/sec^{1/2} [56]. The error quaternion in Eq. (68) is given as measurement vector in the EKF filter.

$$\tilde{\mathbf{y}}_k = [\delta\mathbf{a}/2] = \mathbf{h}_k(\hat{\mathbf{x}}_k) + \mathbf{v}_k \quad (94)$$

The error covariance corresponding to star tracker measurements is given by

$$R = \text{diag}[\sigma_1^2 I_{3 \times 3} \quad \sigma_2^2 I_{3 \times 3} \quad \cdots \quad \sigma_n^2 I_{3 \times 3}] \quad (95)$$

where all diagonal coefficients are 0.001 degrees. The sensitivity matrix for all measurement set is given by

$$H_k(\hat{\mathbf{x}}_k^-) = \begin{bmatrix} \frac{1}{2} I_{3 \times 3} & \mathbf{0}_{3 \times 3} \end{bmatrix} \quad (96)$$

The attitude estimation algorithm is summarized in Table 6.4.

Table 6.4. Extended Kalman Filter for Absolute Attitude Estimation.

Initialize	$\hat{\mathbf{q}}(t_0) = \hat{\mathbf{q}}_0, \quad \hat{\boldsymbol{\beta}}(t_0) = \hat{\boldsymbol{\beta}}_0$ $P(t_0) = P_0$
Gain	$K_k = P_k^- H_k^T(\hat{\mathbf{x}}_k^-) [H_k(\hat{\mathbf{x}}_k^-) P_k^- H_k^T(\hat{\mathbf{x}}_k^-) + R]^{-1}$ $H_k(\hat{\mathbf{x}}_k^-) = \begin{bmatrix} \frac{1}{2} I_{3 \times 3} & \mathbf{0}_{3 \times 3} \end{bmatrix}$
Update	$P_k^+ = [I - K_k H_k(\hat{\mathbf{x}}_k^-)] P_k^-$ $\Delta \hat{\mathbf{x}}_k^+ = K_k [\tilde{\mathbf{y}}_k - \mathbf{h}_k(\hat{\mathbf{x}}_k^-)],$ $\Delta \hat{\mathbf{x}}_k^+ = \begin{bmatrix} \delta \hat{\boldsymbol{\alpha}}_k^{+T} & \Delta \hat{\boldsymbol{\beta}}_k^{+T} \end{bmatrix}^T$ $\mathbf{h}_k(\hat{\mathbf{x}}_k^-) = \begin{bmatrix} \frac{\delta \hat{\boldsymbol{\alpha}}_k^-}{2} \end{bmatrix}$ $\hat{\mathbf{q}}_k^+ = \hat{\mathbf{q}}_k^- + \frac{1}{2} \Xi(\hat{\mathbf{q}}_k^-) \delta \hat{\boldsymbol{\alpha}}_k^{+T}, \text{ renormalize quaternion}$ $\hat{\boldsymbol{\beta}}_k^+ = \hat{\boldsymbol{\beta}}_k^- + \Delta \hat{\boldsymbol{\beta}}_k^+$

Table 6.4. (Continued)

Propagation	$\hat{\omega} = \tilde{\omega} - \Delta\hat{\beta}(t)$ $\dot{\hat{q}}(t) = \frac{1}{2}\Xi(\hat{q}(t))\hat{\omega}(t)$ $\dot{P}(t) = F(\hat{x}(t),t)P(t) + P(t)F^T(\hat{x}(t),t) + G(t)Q(t)G^T(t)$ $F(\hat{x}(t),t) = \begin{bmatrix} -[\hat{\omega} \times] & -I_{3 \times 3} \\ 0_{3 \times 3} & 0_{3 \times 3} \end{bmatrix}, G(t) = \begin{bmatrix} -I_{3 \times 3} & 0_{3 \times 3} \\ 0_{3 \times 3} & I_{3 \times 3} \end{bmatrix}$
--------------------	---

6.4. VISION-BASED RELATIVE STATE ESTIMATION USING THE EXTENDED KALMAN FILTER

6.4.1. Vision-Based Navigation System and Gyro Model. Photogrammetry is the technique of measuring objects (2D or 3D), photographic images, or line of sight (LOS) observations. Photogrammetry can generally be divided into two categories: far range photogrammetry with camera distance setting to infinity (commonly used in star cameras), and close range photogrammetry with camera distance settings to finite values. In general, close-range photogrammetry can be used to determine both the position and attitude of an object, while far range photogrammetry can be only used to determine attitude. The VISNAV system consists of a new kind of optical sensor combined with specific light source beacons, each radiating bursts of modulated light. This sensor can be used for close-range photogrammetry-type applications. The relationship between the position/attitude and observations used in photogrammetry involves a set of colinearity equations. The VISNAV system uses measurements from a positioning sensing diode (PSD) sensor. A small PSD diode senses these light sources, and electronics control both the beacons and the PSD sensor. It calculates six-degrees of freedom estimates of the sensor location and orientation. The hardware and working principles of the VISNAV system are described in References [51], [52]. A spacecraft docking scenario using the VISNAV system is illustrated in Figure 6.2.

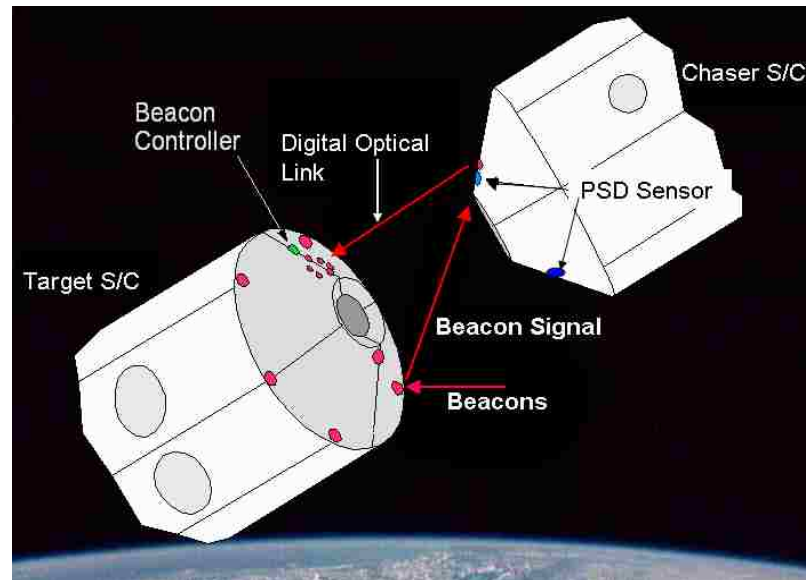


Figure 6.2. VISNAV System for Proximity Operations and Docking. (Figure Adapted from Reference [52])

Six beacons on the target docking port are arrayed in the configuration shown in Figure 6.3. These beacons are arranged to be visible to the PSD on the chaser throughout the final approach phase.

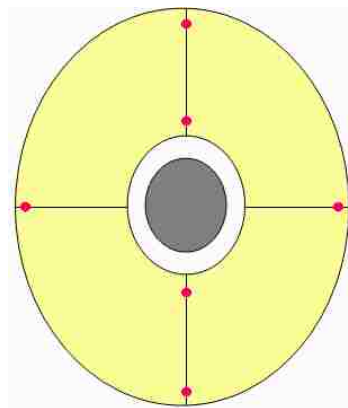


Figure 6.3. Beacons Configuration on the Target Docking Port.

The location of the sensor focal plane, which is usually obtained through calibration, is assumed to be known within the chaser spacecraft coordinate system. Also, without loss

of generality, the frame of the target spacecraft is assumed to coincide with the frame described in Figure 4.2. If the z -axis of the sensor coordinate system is directed outward along the boresight, then, given the object space and image space coordinate frames, the ideal object-to-image space projective transformation (noiseless) can be written as [51], [52]

$$\chi_i = -fl \frac{A_{11}(X_i - x) + A_{12}(Y_i - y) + A_{13}(Z_i - z)}{A_{31}(X_i - x) + A_{32}(Y_i - y) + A_{33}(Z_i - z)}, \quad i = 1, 2, \dots, N \quad (97a)$$

$$\gamma_i = -fl \frac{A_{21}(X_i - x) + A_{22}(Y_i - y) + A_{23}(Z_i - z)}{A_{31}(X_i - x) + A_{32}(Y_i - y) + A_{33}(Z_i - z)}, \quad i = 1, 2, \dots, N \quad (97b)$$

where N is the total number of observations, (χ_i, γ_i) are the image space observations for the i^{th} LOS, (X_i, Y_i, Z_i) are the known object space locations of the i^{th} beacon, (x, y, z) are the unknown object space locations of the sensor modeled by Eq. (2), fl is the known focal length, and A_{jk} are the unknown coefficients of the attitude matrix, A , associated with the orientation from the object plane (target) to the image plane (chaser). The goal of the inverse problem is given observations (χ_i, γ_i) , and object space locations (X_i, Y_i, Z_i) , for $i = 1, 2, \dots, N$, determine the attitude (A) and position (x, y, z) . The observation can be reconstructed in unit vector form as [66]

$$\mathbf{b}_i = A\mathbf{r}_i, \quad i = 1, 2, \dots, N \quad (98)$$

where

$$\mathbf{b}_i = \frac{1}{\sqrt{fl^2 + \chi_i^2 + \gamma_i^2}} \begin{bmatrix} -\chi_i \\ -\gamma_i \\ fl \end{bmatrix} \quad (99a)$$

$$\mathbf{r}_i = \frac{1}{\sqrt{(X_i - x)^2 + (Y_i - y)^2 + (Z_i - z)^2}} \begin{bmatrix} X_i - x \\ Y_i - y \\ Z_i - z \end{bmatrix} \quad (99b)$$

When observation noise is present, Shuster [98] has shown that the greatest error probability is concentrated in a very small area about the direction of $A\mathbf{r}_i$; therefore, the sphere containing that point can be approximated by a tangent plane, characterized by

$$\tilde{\mathbf{b}}_i = A\mathbf{r}_i + \mathbf{v}_i, \quad \mathbf{v}_i^T A\mathbf{r}_i = 0 \quad (100)$$

where $\tilde{\mathbf{b}}_i$ denotes the i^{th} observation and the sensor error \mathbf{v}_i is approximately Gaussian. This satisfies

$$E\{\mathbf{v}_i\} = 0 \quad (101a)$$

$$E\{\mathbf{v}_i \mathbf{v}_i^T\} = \sigma_i^2 [I_{3 \times 3} - (A\mathbf{r}_i)(A\mathbf{r}_i)^T] \quad (101b)$$

where $E\{\}$ denotes expectation and $I_{3 \times 3}$ denotes the 3×3 identity matrix. Eq. (101b) makes the small field-of-view assumption used in References [51-53]. However, for a large FOV lens with significant radial distortion, this covariance model should be modified appropriately. The advantage of using the mode in Eq. (101) is that the observation covariance in the EKF filter and UKF filter formulation can effectively be replaced by a nonsingular matrix given by $\sigma_i^2 I_{3 \times 3}$ [51-53]. Hence, the observation covariance matrix used in the estimator from all available LOS vectors is given by

$$R_k = \text{diag}[\sigma_1^2 \quad \sigma_2^2 \quad \dots \quad \sigma_N^2] \quad (102)$$

Multiple (N) vector observations can be concatenated to form

$$\tilde{\mathbf{y}}_k = \begin{bmatrix} A(\mathbf{q})\mathbf{r}_1 \\ A(\mathbf{q})\mathbf{r}_2 \\ \vdots \\ A(\mathbf{q})\mathbf{r}_N \end{bmatrix} + \begin{bmatrix} \mathbf{v}_1 \\ \mathbf{v}_2 \\ \vdots \\ \mathbf{v}_N \end{bmatrix} \quad (103)$$

A common sensor that measures the angular rate is a rate-integrating gyroscope. For this sensor, a widely used model is given by Eq. (85). In this study, $(\boldsymbol{\eta}_{rv}, \boldsymbol{\eta}_{ru})$ and $(\boldsymbol{\eta}_{cv}, \boldsymbol{\eta}_{cu})$ denote target and chaser gyros parameters, respectively. Gyro measurements are expressed in the inertial frame. The gyro noise parameters are given by

$\sigma_{tu} = \sigma_{cu} = \sqrt{10} \times 10^{-10}$ rad/sec^{3/2} and $\sigma_{cv} = \sigma_{cv} = \sqrt{10} \times 10^{-5}$ rad/sec^{1/2} [66]. The initial biases for each axis of both the target and the chaser gyros are given as 1 deg/hr.

6.4.2. Relative State Estimation. An EKF filter is used to sequentially estimate the relative position, velocity and relative attitude. A formulation for the relative attitude estimation, as well as the target and chaser gyro biases, are derived. The true equations are given by [66] as

$$\mathbf{q}_{rel} = \mathbf{q}_c \otimes \mathbf{q}_t^{-1} \quad (104a)$$

$$\dot{\mathbf{q}}_{rel} = \frac{1}{2} \Xi(\mathbf{q}_{rel}) \boldsymbol{\omega}_{ct} \quad (104b)$$

$$\boldsymbol{\omega}_{ct} = \boldsymbol{\omega}_c - A(\mathbf{q}_{rel}) \boldsymbol{\omega}_t \quad (104c)$$

$$\dot{\boldsymbol{\beta}}_t = \boldsymbol{\eta}_{tu} \quad (104d)$$

$$\dot{\boldsymbol{\beta}}_c = \boldsymbol{\eta}_{cu} \quad (104e)$$

$$\boldsymbol{\omega}_t = \tilde{\boldsymbol{\omega}}_t - \boldsymbol{\beta}_t - \boldsymbol{\eta}_{tu} \quad (104f)$$

$$\boldsymbol{\omega}_c = \tilde{\boldsymbol{\omega}}_c - \boldsymbol{\beta}_c - \boldsymbol{\eta}_{cu} \quad (104g)$$

where subscripts t and c denote the target and chaser vehicles. The quaternion \mathbf{q}_{rel} describes the relative attitude between the target and chaser. The relative angular rate is denoted $\boldsymbol{\omega}_{ct}$. The error quaternion and its derivatives are given by

$$\delta \mathbf{q}_{rel} = \mathbf{q}_{rel} \otimes \hat{\mathbf{q}}_{rel}^{-1} \quad (105a)$$

$$\delta \mathbf{q}_{rel} = \begin{bmatrix} 1 \\ 2 \\ 1 \end{bmatrix} \delta \boldsymbol{\alpha} \quad (105b)$$

where $\delta \boldsymbol{\alpha}$ represents roll, pitch and yaw error angles needing correction. This study uses the error-state dynamics for attitude estimation derived in Reference [66] as

$$\Delta \dot{\boldsymbol{\alpha}} = -[\hat{\boldsymbol{\omega}}_c] \delta \boldsymbol{\alpha} - \Delta \boldsymbol{\beta}_c + A(\hat{\mathbf{q}}) \Delta \boldsymbol{\beta}_t + A(\hat{\mathbf{q}}_{rel}) \Delta \boldsymbol{\eta}_{tv} - \boldsymbol{\eta}_{cv} \quad (106)$$

The error-state vector for the relative attitude estimation is augmented to include the relative position and velocity vectors in Eq. (66). The state vector for attitude estimation is appended to include the relative position and velocity. The error-state equation for the relative attitude estimation is combined with the nonlinear equation of motion in Eq. (13) adding the process noise. The augmented error-dynamics is then expressed by in state-space form as

$$\Delta \mathbf{x} = F_{aug} \Delta \mathbf{x} + G \mathbf{w} \quad (107)$$

with

$$\Delta \mathbf{x} = \left[\Delta \boldsymbol{\alpha}^T \quad \Delta \boldsymbol{\beta}_t^T \quad \Delta \boldsymbol{\beta}_c^T \quad \Delta \boldsymbol{\rho}^T \quad \Delta \dot{\boldsymbol{\rho}}^T \right]^T \quad (108a)$$

$$\mathbf{w} = \left[\boldsymbol{\eta}_{tv}^T \quad \boldsymbol{\eta}_{cv}^T \quad \boldsymbol{\eta}_{tu}^T \quad \boldsymbol{\eta}_{cu}^T \quad w_x \quad w_y \quad w_z \right]^T \quad (108b)$$

where $\Delta \boldsymbol{\rho}^T$ and $\Delta \dot{\boldsymbol{\rho}}^T$ are the error-state vector for the relative position and velocity estimation. The matrices F_{aug} and G_{aug} used in the EKF covariance propagation are given by

$$F_{aug} = \begin{bmatrix} -[\hat{\boldsymbol{\omega}}_c \times] & A(\hat{\mathbf{q}}) & -I_{3 \times 3} & \mathbf{0}_{3 \times 6} \\ \mathbf{0}_{3 \times 3} & \mathbf{0}_{3 \times 3} & \mathbf{0}_{3 \times 3} & \mathbf{0}_{3 \times 6} \\ \mathbf{0}_{3 \times 3} & \mathbf{0}_{3 \times 3} & \mathbf{0}_{3 \times 3} & \mathbf{0}_{3 \times 6} \\ \mathbf{0}_{3 \times 3} & \mathbf{0}_{3 \times 3} & \mathbf{0}_{3 \times 3} & [\partial \mathbf{f}(\mathbf{X}) / \partial \mathbf{X}]_{\hat{\mathbf{x}}} \end{bmatrix} \quad (109a)$$

where the partial derivative matrix, $\partial \mathbf{f}(\mathbf{X}) / \partial \mathbf{X}$ is equal to Eq. (67).

$$G_{aug} = \begin{bmatrix} A(\hat{\mathbf{q}}) & -I_{3 \times 3} & \mathbf{0}_{3 \times 3} & \mathbf{0}_{3 \times 3} & \mathbf{0}_{3 \times 3} \\ \mathbf{0}_{3 \times 3} & \mathbf{0}_{3 \times 3} & I_{3 \times 3} & \mathbf{0}_{3 \times 3} & \mathbf{0}_{3 \times 3} \\ \mathbf{0}_{3 \times 3} & \mathbf{0}_{3 \times 3} & \mathbf{0}_{3 \times 3} & I_{3 \times 3} & \mathbf{0}_{3 \times 3} \\ \mathbf{0}_{3 \times 3} & \mathbf{0}_{3 \times 3} & \mathbf{0}_{3 \times 3} & \mathbf{0}_{3 \times 3} & \mathbf{0}_{3 \times 3} \\ \mathbf{0}_{3 \times 3} & \mathbf{0}_{3 \times 3} & \mathbf{0}_{3 \times 3} & \mathbf{0}_{3 \times 3} & I_{3 \times 3} \end{bmatrix} \quad (109b)$$

The new augmented matrix Q_{aug} corresponding to new process noise vector defined in Eq. (107) is given by

$$Q_{aug} = \begin{bmatrix} \sigma_{iv}^2 I_{3 \times 3} & 0_{3 \times 3} & 0_{3 \times 3} & 0_{3 \times 3} & 0_{3 \times 1} & 0_{3 \times 1} & 0_{3 \times 1} \\ 0_{3 \times 3} & \sigma_{cv}^2 I_{3 \times 3} & 0_{3 \times 3} & 0_{3 \times 3} & 0_{3 \times 1} & 0_{3 \times 1} & 0_{3 \times 1} \\ 0_{3 \times 3} & 0_{3 \times 3} & \sigma_{uv}^2 I_{3 \times 3} & 0_{3 \times 3} & 0_{3 \times 1} & 0_{3 \times 1} & 0_{3 \times 1} \\ 0_{3 \times 3} & 0_{3 \times 3} & 0_{3 \times 3} & \sigma_{cu}^2 I_{3 \times 3} & 0_{3 \times 1} & 0_{3 \times 1} & 0_{3 \times 1} \\ 0_{1 \times 3} & 0_{1 \times 3} & 0_{1 \times 3} & 0_{1 \times 3} & w_x^2 & 0 & 0 \\ 0_{1 \times 3} & 0_{1 \times 3} & 0_{1 \times 3} & 0_{1 \times 3} & 0 & w_y^2 & 0 \\ 0_{1 \times 3} & 0_{1 \times 3} & 0_{1 \times 3} & 0_{1 \times 3} & 0 & 0 & w_z^2 \end{bmatrix} \quad (110)$$

The state transition matrix for the error covariance can be computed numerically by van Loan's method [64], [99] as

$$\bar{A} = \begin{bmatrix} -F_{aug} & G_{aug} Q G_{aug}^T \\ 0_{15 \times 15} & F_{aug}^T \end{bmatrix} \Delta t \quad (111)$$

Then, the matrix exponential of Eq. (111) is computed as

$$\bar{B} = e^{\bar{A}} = \begin{bmatrix} \bar{B}_{11} & \bar{B}_{12} \\ 0_{15 \times 15} & \bar{B}_{22} \end{bmatrix} = \begin{bmatrix} \bar{B}_{11} & \Phi^{-1} \bar{B}_{12} \\ 0 & \Phi^T \end{bmatrix} \quad (112)$$

where Φ is the state transition matrix of F_{aug} and \bar{Q} is the discrete-time covariance matrix. The state transition matrix and discrete-time process noise covariance are then given by

$$\Phi^{-1} = \bar{B}_{22}^T \quad (113a)$$

$$\bar{Q} = \Phi \bar{B}_{12} \quad (113b)$$

The measurement sensitivity matrix is given by [66]

$$H_k(\hat{\mathbf{q}}_{rel}^-, \hat{\mathbf{p}}_k^-) = \begin{bmatrix} [A(\hat{\mathbf{q}}_{rel}^-) \hat{\mathbf{r}}_1^- \times] & \mathbf{0}_{3 \times 3} & \mathbf{0}_{3 \times 3} & \frac{\partial \hat{\mathbf{b}}_1^-}{\partial \hat{\mathbf{p}}^-} & \mathbf{0}_{3 \times 3} \\ \vdots & \vdots & \vdots & \vdots & \vdots \\ [A(\hat{\mathbf{q}}_{rel}^-) \hat{\mathbf{r}}_N^- \times] & \mathbf{0}_{3 \times 3} & \mathbf{0}_{3 \times 3} & \frac{\partial \hat{\mathbf{b}}_N^-}{\partial \hat{\mathbf{p}}^-} & \mathbf{0}_{3 \times 3} \end{bmatrix}_{l_k} \quad (114)$$

where $\hat{\mathbf{r}}_i^-$ is given by Eq. (99b) evaluated at $\hat{\mathbf{p}}^- = [\hat{x}^- \quad \hat{y}^- \quad \hat{z}^-]^T$ and the partial matrix $\partial \hat{\mathbf{b}}_i^- / \partial \hat{\rho}^-$ is given by

$$\frac{\partial \hat{\mathbf{b}}_i^-}{\partial \hat{\rho}^-} = A(\hat{\mathbf{q}}^-) \frac{\partial \hat{\mathbf{r}}_i^-}{\partial \hat{\rho}^-} \quad (115)$$

where

$$\frac{\partial \hat{\mathbf{r}}_i^-}{\partial \hat{\rho}^-} = \frac{1}{\hat{s}_i^-} \times \begin{bmatrix} -[(Y_i - \hat{y}^-)^2 + (Z_i - \hat{z}^-)^2] & (X_i - \hat{x}^-)(Y_i - \hat{y}^-) & (X_i - \hat{x}^-)(Z_i - \hat{z}^-) \\ (X_i - \hat{x}^-)(Y_i - \hat{y}^-) & -[(Y_i - \hat{y}^-)^2 + (Z_i - \hat{z}^-)^2] & (Y_i - \hat{y}^-)(Z_i - \hat{z}^-) \\ (X_i - \hat{x}^-)(Z_i - \hat{z}^-) & (Y_i - \hat{y}^-)(Z_i - \hat{z}^-) & -[(X_i - \hat{x}^-)^2 + (Z_i - \hat{z}^-)^2] \end{bmatrix} \quad (116)$$

with $\hat{s}_i^- = [(X_i - \hat{x}^-)^2 + (Y_i - \hat{y}^-)^2 + (Z_i - \hat{z}^-)^2]^{3/2}$.

The EKF filter using the vision sensor system can now be executed with these quantities to estimate the relative attitude, position and velocity. The estimated relative quaternion $\hat{\mathbf{q}}_{rel}$ is then used to compute the absolute chaser quaternion using Eq. (104a) by multiplying the known target quaternions using onboard navigation data. The absolute chaser quaternion $\hat{\mathbf{q}}_c$ is computed by Eq. (117) as

$$\hat{\mathbf{q}}_c \cong \hat{\mathbf{q}}_{rel} \otimes \hat{\mathbf{q}}_t = (\hat{\mathbf{q}}_c \otimes \hat{\mathbf{q}}_t^{-1}) \otimes \hat{\mathbf{q}}_t \quad (117)$$

A summary of the EKF filter equations for the relative attitude estimation using vision sensor measurement is shown in Table 6.5 [66].

Table 6.5. Extended Kalman Filter for Relative Attitude Estimation.

Initialize	$\hat{\mathbf{q}}(t_0) = \hat{\mathbf{q}}_0, \quad \hat{\boldsymbol{\beta}}_t(t_0) = \hat{\boldsymbol{\beta}}_{t_0}, \quad \hat{\boldsymbol{\beta}}_c(t_0) = \hat{\boldsymbol{\beta}}_{c_0}$ $P(t_0) = P_0$
Gain	$K_k = P_k^- H_k^T(\hat{\mathbf{x}}_k^-) [H_k(\hat{\mathbf{x}}_k^-) P_k^- H_k^T(\hat{\mathbf{x}}_k^-) + R]^{-1}$ $H_k(\hat{\mathbf{q}}_{rel_k}^-, \hat{\boldsymbol{\beta}}_k^-) = \begin{bmatrix} [A(\hat{\mathbf{q}}_{rel}^-) \hat{\mathbf{r}}_1^- \times] & 0_{3 \times 3} & 0_{3 \times 3} & \frac{\partial \hat{\mathbf{b}}_1^-}{\partial \hat{\boldsymbol{\rho}}^-} & 0_{3 \times 3} \\ \vdots & \vdots & \vdots & \vdots & \vdots \\ [A(\hat{\mathbf{q}}_{rel}^-) \hat{\mathbf{r}}_N^- \times] & 0_{3 \times 3} & 0_{3 \times 3} & \frac{\partial \hat{\mathbf{b}}_N^-}{\partial \hat{\boldsymbol{\rho}}^-} & 0_{3 \times 3} \end{bmatrix}_{t_k}$
Update	$P_k^+ = [I - K_k H_k(\hat{\mathbf{x}}_k^-)] P_k^-$ $\Delta \hat{\mathbf{x}}_k^+ = K_k [\mathbf{y}_k - \mathbf{h}_k(\hat{\mathbf{x}}_k^-)],$ $\Delta \hat{\mathbf{x}}_k^+ = [\delta \hat{\boldsymbol{\alpha}}_k^{+T} \quad \Delta \hat{\boldsymbol{\beta}}_k^{+T}]^T$ $\mathbf{h}_k(\hat{\mathbf{x}}_k^-) = \begin{bmatrix} A(\mathbf{q}) \mathbf{r}_1 \\ A(\mathbf{q}) \mathbf{r}_2 \\ \vdots \\ A(\mathbf{q}) \mathbf{r}_N \end{bmatrix}$ $\hat{\mathbf{q}}_{rel_k}^+ = \hat{\mathbf{q}}_{rel_k}^- + \frac{1}{2} \Xi(\hat{\mathbf{q}}_{rel_k}^-) \delta \hat{\boldsymbol{\alpha}}_k^{+T}, \text{ renormalize quaternion}$ $\hat{\boldsymbol{\beta}}_{t_k}^+ = \hat{\boldsymbol{\beta}}_{t_k}^- + \Delta \hat{\boldsymbol{\beta}}_{t_k}^+$ $\hat{\boldsymbol{\beta}}_{c_k}^+ = \hat{\boldsymbol{\beta}}_{c_k}^- + \Delta \hat{\boldsymbol{\beta}}_{c_k}^+$
Propagation	$\hat{\boldsymbol{\omega}}_{t_k}^+ = \tilde{\boldsymbol{\omega}}_{t_k}^+ - \hat{\boldsymbol{\beta}}_{t_k}^+$ $\hat{\boldsymbol{\omega}}_{c_k}^+ = \tilde{\boldsymbol{\omega}}_{c_k}^+ - \hat{\boldsymbol{\beta}}_{c_k}^+$ $\hat{\mathbf{q}}_{k+1}^- = \tilde{\Omega}(\hat{\boldsymbol{\omega}}_{c_k}^+) \Gamma(\hat{\boldsymbol{\omega}}_{t_k}^+) \hat{\mathbf{q}}_k^+$ $P_{k+1}^- = \Phi_k P_k^{+1} \Phi_k^T + \bar{Q}_k$

Given the post update $\hat{\mathbf{w}}_k^+$ and $\hat{\mathbf{q}}_k^+$, the discrete-time propagation of the kinematic equation of Eq. (72) is given by [56] as

$$\mathbf{q}_{k+1} = \bar{\mathcal{Q}}(\hat{\mathbf{w}}_{t_k}) \bar{\Gamma}(\hat{\mathbf{w}}_{t_k}) \mathbf{q}_k \quad (118)$$

with

$$\bar{\mathcal{Q}}(\mathbf{w}_{c_k}) = \begin{bmatrix} \cos\left(\frac{1}{2}\|\mathbf{w}_{c_k}\|\Delta t\right) I_{3 \times 3} - [\boldsymbol{\psi}_k \times] & \boldsymbol{\psi}_k \\ -\boldsymbol{\psi}_k^T & \cos\left(\frac{1}{2}\|\mathbf{w}_{c_k}\|\Delta t\right) \end{bmatrix} \quad (119a)$$

$$\bar{\Gamma}(\mathbf{w}_{t_k}) = \begin{bmatrix} \cos\left(\frac{1}{2}\|\mathbf{w}_{t_k}\|\Delta t\right) I_{3 \times 3} - [\boldsymbol{\zeta}_k \times] & -\boldsymbol{\zeta}_k \\ -\boldsymbol{\zeta}_k^T & \cos\left(\frac{1}{2}\|\mathbf{w}_{t_k}\|\Delta t\right) \end{bmatrix} \quad (119b)$$

where

$$\boldsymbol{\psi}_k = \frac{\sin\left(\frac{1}{2}\|\mathbf{w}_{c_k}\|\Delta t\right) \mathbf{w}_{c_k}}{\|\mathbf{w}_{c_k}\|} \quad (120a)$$

$$\boldsymbol{\zeta}_k = \frac{\sin\left(\frac{1}{2}\|\mathbf{w}_{t_k}\|\Delta t\right) \mathbf{w}_{t_k}}{\|\mathbf{w}_{t_k}\|} \quad (120b)$$

and Δt is the sampling interval. Note that the matrices $\bar{\mathcal{Q}}(\mathbf{w}_{d_k})$ and $\bar{\Gamma}(\mathbf{w}_{c_k})$ also commute.

6.5. VISION-BASED RELATIVE STATE ESTIMATION USING THE UNSCENTED KALMAN FILTER

The local error-quaternion, denoted by $\delta \mathbf{q} = [\delta \boldsymbol{\rho}^T \ \delta q_4]$ and defined in the UKF formulation, is represented using a vector of generalized Rodrigues parameters [92], [100]

$$\delta \mathbf{p} = g \frac{\delta \mathbf{p}}{a + \delta q_4} \quad (121)$$

where a is a parameter from 0 to 1, and g is a scale factor. Note when $a = 0$ and $g = 1$ then Eq. (121) gives the Gibbs vector. Further, with $a = g = 1$ then Eq. (121) gives the standard vector of MRPs. For small errors the attitude portion of the covariance is closely related to the attitude estimation errors for any rotation sequence, given by a simple factor [91]. For example, the Gibbs vector linearizes the half angles. The choice of $g = 2(a + 1)$ is made so that $\|\delta \mathbf{p}\|$ is equal to \mathcal{G} for small errors. The inverse transformation from $\|\delta \mathbf{p}\|$ to $\delta \mathbf{q}$ is given by [92] as

$$\delta q_4 = \frac{-a\|\delta \mathbf{p}\|^2 + g\sqrt{g^2 + (1 - a^2)\|\delta \mathbf{p}\|^2}}{g^2 + \|\delta \mathbf{p}\|^2} \quad (122a)$$

$$\delta \mathbf{p} = g^{-1}(a + \delta q_4)\delta \mathbf{p} \quad (122b)$$

A common sensor that measures the angular rate is a rate-integrating gyroscope as described in the previous section. In the standard EKF filter formulation, given a post-update estimate $\hat{\boldsymbol{\beta}}_k^+$, the post-update angular velocity of the target or chaser and its propagated gyro bias are

$$\hat{\boldsymbol{\omega}}_k^+ = \tilde{\boldsymbol{\omega}}_k - \hat{\boldsymbol{\beta}}_k^+ \quad (123a)$$

$$\hat{\boldsymbol{\beta}}_{k+1} = \hat{\boldsymbol{\beta}}_k \quad (123b)$$

In general, a UKF filter cannot be implemented directly with the equations in Section 6.1.2 because of the violation of the unit quaternion constraint. The difficulty with computing the means of a set of sigma points lies in the fact that the rotation represented by the quaternion does not belong to a vector space, but lies on a nonlinear manifold. Further, the quaternion is constrained to the three-dimensional unit sphere of a four-dimensional Euclidian space. The quaternion predicted mean using Eq. (54) is not

guaranteed to maintain a unit quaternion because the quaternion is not mathematically closed for addition and scalar multiplication. This limitation makes the straightforward implementation of the UKF filter with quaternions undesirable. On the other hand, an EKF filter can be designed using this approach in which the quaternion normalization is performed by “brute force.” To use the UKF filter, an unconstrained three component vector is used to represent an attitude error quaternion. First, the state vector is defined as

$$\boldsymbol{\chi}_k(0) = \hat{\mathbf{x}}_k = \begin{bmatrix} \delta \hat{\mathbf{p}}_k^+ \\ \hat{\boldsymbol{\beta}}_{c_k}^+ \\ \hat{\boldsymbol{\beta}}_{d_k}^+ \end{bmatrix} \quad (124)$$

where $\delta \hat{\mathbf{p}}_k^+$ is the updated vector of generalized Rodrigues parameters, and $\hat{\boldsymbol{\beta}}_{c_k}^+$ and $\hat{\boldsymbol{\beta}}_{d_k}^+$ are the updated gyro bias of the target and the chaser spacecraft, respectively. Using $\delta \hat{\mathbf{p}}_k^+$ from Eq. (121), the nominal quaternion is propagated and updated. The overall covariance is a 9×9 matrix, and this three-dimensional representation is unconstrained. The use of Eq. (51) causes no difficulty, providing an attractive method of attitude representation. First, the vector $\boldsymbol{\chi}_k(i)$ in Eq. (47) is partitioned into

$$\boldsymbol{\chi}_k(i) = \begin{bmatrix} \boldsymbol{\chi}_k^{\delta p}(i) \\ \boldsymbol{\chi}_k^{\beta_t}(i) \\ \boldsymbol{\chi}_k^{\beta_c}(i) \end{bmatrix}, \quad i = 0, 1, \dots, 18 \quad (125)$$

where $\boldsymbol{\chi}_k^{\delta p}$ is the attitude-error, $\boldsymbol{\chi}_k^{\beta_t}(i)$ is the target gyro bias and $\boldsymbol{\chi}_k^{\beta_c}(i)$ is the chaser gyro bias. Since the unit quaternion is not closed for addition and subtraction, the transformed sigma points of the quaternion are not simply constructed but are computed using Eq. (126), while the sigma points for the gyro bias calculated by Eq. (47). Rather, the transformed sigma points of the quaternion are also quaternions satisfying the normalization constraints and should be scattered around the current quaternion estimate on the unit sphere. Therefore, the transformed quaternion sigma points are generated by

multiplying an error quaternion by the current estimate. To generate quaternion samples evenly on the unit sphere around the current quaternion estimate, both the error quaternion and the inverse of the quaternion $\delta\mathbf{q}_{i,k}^+$ and $(\delta\mathbf{q}_{i,k}^+)^{-1}$ are used. The sigma point quaternions are then computed using

$$\boldsymbol{\chi}_{0,k}^q = \hat{\mathbf{q}}_k^+ \quad (126a)$$

$$\boldsymbol{\chi}_{i,k}^q = \delta\hat{\mathbf{q}}_{i,k}^+ \otimes \hat{\mathbf{q}}_k^+ \quad \text{for } i=1,\dots,9 \quad (126b)$$

$$\boldsymbol{\chi}_{0,k}^q = (\delta\hat{\mathbf{q}}_k^+)^{-1} \otimes \hat{\mathbf{q}}_{i,k}^+ \quad \text{for } i=10,\dots,18 \quad (126c)$$

where $\delta\mathbf{q}_k^+(i) = [\delta\boldsymbol{\rho}_k^{+T} \quad \delta q_{4,k}^+(i)]^T$ is represented by Eq. (38) as

$$\delta q_{4,k}^+(i) = \frac{-a\|\boldsymbol{\chi}_k^{\delta p}(i)\|^2 + g\sqrt{g^2 + (1-a^2)\|\boldsymbol{\chi}_k^{\delta p}(i)\|^2}}{g^2 + \|\boldsymbol{\chi}_k^{\delta p}(i)\|^2} \quad \text{for } i = 1, 2, \dots, 18 \quad (127a)$$

$$\delta\boldsymbol{\rho}_k^+(i) = g^{-1} [a + \delta q_{4,k}^+(i)] \boldsymbol{\chi}_k^{\delta p}(i) \quad \text{for } i = 1, 2, \dots, 18 \quad (127b)$$

Eq. (126a) clearly requires that $\boldsymbol{\chi}_k^{\delta p}(0)$ be zero since the attitude error is reset to zero after the update, which moves information from one part of the estimate to another part. For the definition of sigma points, the gyro bias part of the target and the chaser from $\gamma\sqrt{P_k + \bar{Q}_k}$ in Eq. (49) are denoted as $\zeta_k^{\beta_t}$ and $\zeta_k^{\beta_c}$, respectively. The sigma points corresponding to the quaternion actually depend on the quaternion itself regardless of the target and the chaser bias. All sigma points are constructed as

$$\boldsymbol{\chi}_k(i) = \begin{bmatrix} \boldsymbol{\chi}_k^{\delta p}(i) \\ \boldsymbol{\chi}_k^{\beta_t}(i) \\ \boldsymbol{\chi}_k^{\beta_c}(i) \end{bmatrix} = \begin{bmatrix} \hat{\mathbf{q}}_k^+ & \delta\hat{\mathbf{q}}_k^+ \oplus \hat{\mathbf{q}}_k^+ & (\delta\hat{\mathbf{q}}_k^+)^{-1} \oplus \hat{\mathbf{q}}_k^+ \\ \hat{\boldsymbol{\beta}}_{c_k}^+ & \hat{\boldsymbol{\beta}}_k^+ + \zeta_k^{\beta_t} & \hat{\boldsymbol{\beta}}_k^+ - \zeta_k^{\beta_t} \\ \hat{\boldsymbol{\beta}}_{d_k}^+ & \hat{\boldsymbol{\beta}}_k^+ + \zeta_k^{\beta_c} & \hat{\boldsymbol{\beta}}_k^+ - \zeta_k^{\beta_c} \end{bmatrix} \quad (128)$$

Now these transformed quaternions are propagated forward to $k+1$ by Eq. (129) as

$$\mathbf{q}_{k+1}(i) = \overline{\mathcal{Q}}(\hat{\boldsymbol{\omega}}_{c_k}) \overline{\Gamma}(\hat{\boldsymbol{\omega}}_{t_k}) \mathbf{q}_k(i) \quad i=0, 1, \dots, 18 \quad (129)$$

where the estimated angular velocities of the target and the chaser are given by Eq. (130) as

$$\hat{\boldsymbol{\omega}}_{t_k}^+(i) = \tilde{\boldsymbol{\omega}}_{t_k}(i) - \boldsymbol{\chi}_k^{\beta_t}(i) \quad i = 0, 1, \dots, 18 \quad (130a)$$

$$\hat{\boldsymbol{\omega}}_{c_k}^+(i) = \tilde{\boldsymbol{\omega}}_{c_k}(i) - \boldsymbol{\chi}_k^{\beta_c}(i) \quad i = 0, 1, \dots, 18 \quad (130b)$$

Note that $\boldsymbol{\chi}_k^{\beta_c}(0)$ is the zeroth-bias sigma point given by the current estimates $\boldsymbol{\chi}_k^{\beta_c}(0) = \hat{\boldsymbol{\beta}}_{c_k}^+$, $\boldsymbol{\chi}_k^{\beta_d}(0) = \hat{\boldsymbol{\beta}}_{d_k}^+$. The propagated quaternion is computed using

$$\delta \hat{\mathbf{q}}_{i,k}^- = \delta \tilde{\mathbf{q}}_{i,k}^- \otimes [\hat{\mathbf{q}}_k^-(0)]^{-1}, \quad i = 0, 1, \dots, 18 \quad (131)$$

Note that $\hat{\mathbf{q}}_k^-(0)$ is the identity quaternion. Finally, the propagated sigma points can be computed using the representation in Eq. (118) as

$$\boldsymbol{\chi}_{k+1}^{\delta p}(0) = \mathbf{0}_{3 \times 1} \quad (132a)$$

$$\boldsymbol{\chi}_{k+1}^{\delta p}(i) = g \frac{\delta \mathbf{p}_{k+1}^-(i)}{a + \delta q_{4,k+1}^-(i)}, \quad i = 0, 1, \dots, 18 \quad (132b)$$

with $[\delta \mathbf{p}_{k+1}^{-T}(i) \quad \delta q_{4,k+1}^-(i)]^T = \delta \mathbf{q}_{k+1}^{-T}(i)$. Furthermore, from Eq. 41(b)

$$\boldsymbol{\chi}_{k+1}^{\beta_t}(i) = \boldsymbol{\chi}_k^{\beta_t}(i), \quad i = 0, 1, \dots, 18 \quad (129a)$$

$$\boldsymbol{\chi}_{k+1}^{\beta_c}(i) = \boldsymbol{\chi}_k^{\beta_c}(i), \quad i = 0, 1, \dots, 18 \quad (129b)$$

The predicted mean and covariance can now be computed using Eqs. (51) and (53). The output covariance, innovation covariance and cross-correlation matrices are computed using Eqs. (52), (55), and (56). Next, the state vector and covariance are updated using Eqs. (59) and (60) with $\hat{\mathbf{x}}_{k+1}^+ = \begin{bmatrix} \delta \hat{\mathbf{p}}_k^{+T} & \hat{\mathbf{p}}_{t_k}^{+T} & \hat{\mathbf{p}}_{c_k}^{+T} \end{bmatrix}^T$. The quaternion is then updated using

$$\hat{\mathbf{q}}_{k+1}^+ = \delta \hat{\mathbf{q}}_{k+1}^+ \otimes \hat{\mathbf{q}}_{k+1}^- (0) \quad (130)$$

Note that $\delta \mathbf{q}_{k+1}^+ = \begin{bmatrix} \delta \mathbf{p}_{k+1}^{+T} & \delta q_{4_{k+1}}^+ \end{bmatrix}^T$ is represented by Eq. (122) as

$$\delta q_{4_{k+1}}^+ = \frac{-a \|\delta \hat{\mathbf{p}}_{k+1}^+\|^2 + g \sqrt{g^2 + (1-a^2)} \|\delta \hat{\mathbf{p}}_{k+1}^+\|^2}{g^2 + \|\delta \hat{\mathbf{p}}_{k+1}^+\|^2} \quad (131a)$$

$$\delta \mathbf{p}_{k+1}^+ = g^{-1} (a + \delta q_{4_{k+1}}^+) \delta \mathbf{p} \quad (131b)$$

Finally, $\delta \hat{\mathbf{p}}_{k+1}^+$ is reset to zero for the next propagation. The relative position and velocity estimation can be augmented and estimated with the relative attitude estimation by the previously described in the section 6.4.2. The UKF algorithm is then designed using Table 6.2.

6.6. SIMULATION RESULTS AND ANALYSIS

This section shows simulation results and analysis for bounded relative motion and rendezvous maneuver when using the UKF filter separately from the GNC system.

6.6.1. Bounded Relative Motion. In this section several performance comparisons are made between UKF and EKF approaches through simulated examples using STK for realistic relative navigation between the target and the chaser. For this simulation, a bounded relative motion constraint is applied using Eq. (5). The ground tracks and orbits of the two spacecraft appear almost identical. The scenario begins at perigee of the target and proceeds over ten hours of bounded relative motion. The ground

tracks and orbits of both the target and the chaser are illustrated in Figures 6.4 and 6.5. The initial condition for the vector \mathbf{X} in appropriate units of meters, meters per second, radians and radians per second is given by

$$\mathbf{X}(t_0) = \begin{bmatrix} 200 & 200 & 100 & 0.01 & -0.45723 & 0.01 & 6.7317488 \times 10^6 & 0 & 0 & 0.0011437 \end{bmatrix}^T \quad (132)$$

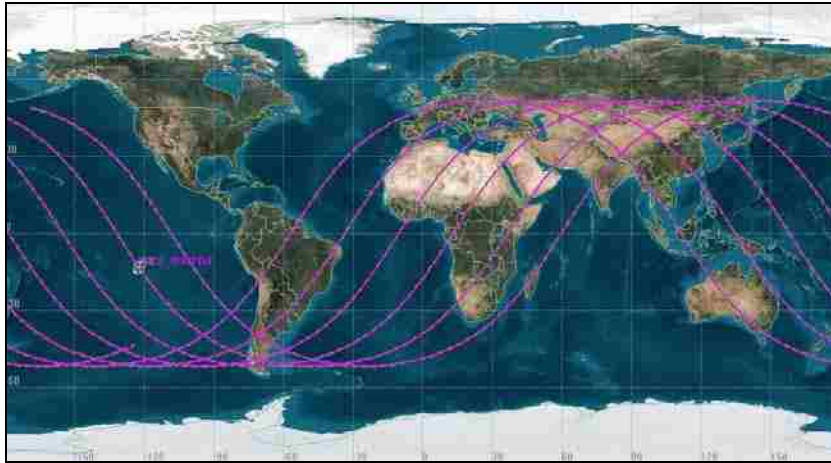


Figure 6.4. Ground Tracks of Target and Chaser.

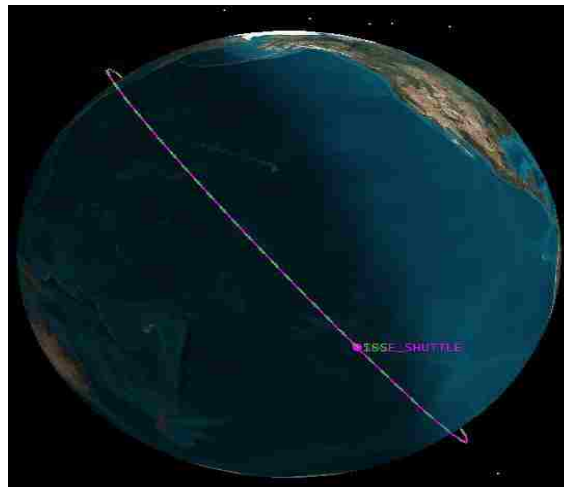


Figure 6.5. Orbits of Target and Chaser.

The simulation time for the relative motion between the two spacecraft is 600 minutes, and the step size is 10 seconds. The orbit period of the target is nearly 92 minutes. For the

entire simulation, the true relative attitude is simulated by propagating Eq. (118) using an initial quaternion given by $\mathbf{q}_{rel}(t_0) = [\sqrt{2}/2 \ 0 \ 0 \ \sqrt{2}/2]^T$ and angular velocities given by $\boldsymbol{\omega}_t = [0 \ 0.0011 \ -0.0011]$ rad/sec and $\boldsymbol{\omega}_c = [-0.002 \ 0 \ 0.0011]$ rad/sec. Six beacons are assumed to be located on the target, and their configuration is shown in Figure 6.6. Six beacons are assumed to be visible to the PSD on the chaser throughout the entire simulation. Simulated VISNAV observations are generated using Eq. (100) with a standard observation deviation of 0.0005 degrees. Each individual covariance sub-matrix for attitude, gyro biases, position and velocity is assumed to be isotropic, a diagonal matrix with equal elements. To validate the estimated relative position and velocity, a simulation truth model is generated with Eq. (3) adding acceleration disturbances to the right side, which are modeled as zero-mean Gaussian white-noise process. However, this model may not be sufficiently realistic. To address this issue, a high-fidelity propagator may be used instead to generate “true” spacecraft ephemerides. For a more realistic validation, both spacecraft are modeled with HPOP of STK [72] using the force model in Table 6.6. The simulated truth model is computed using Eq. (4.8).

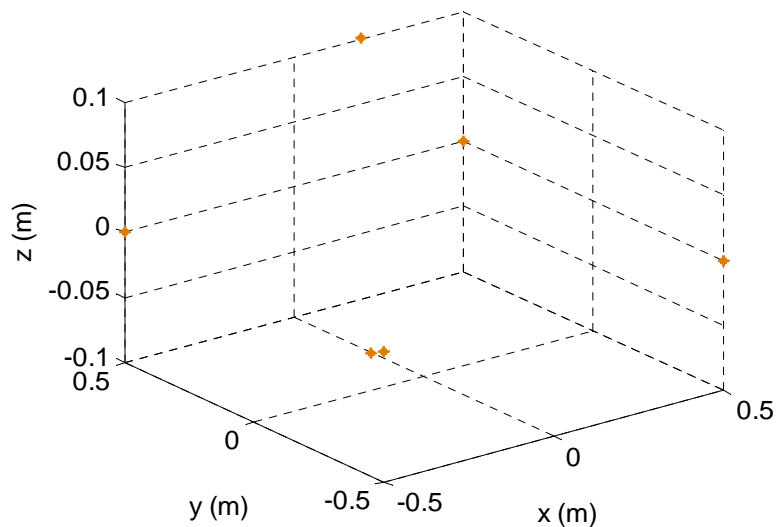


Figure 6.6. Beacons Configuration in the CW Frame.

Table 6.6. Inertial Propagation Force Model.

HPOP
Gravity Field Degree and Order (70×70)
Atmospheric Drag
Solar Radiation Drag
Third Body Gravity (Moon and Sun)

The first simulations with both the UKF and the EKF filters are performed under ideal conditions, i.e. with no initial attitude errors, initial bias estimates set to zero and no initial position and velocity errors. The initial attitude covariance is set to $P_{att} = I_{3 \times 3} (\text{deg})^2$, and the initial target and chaser gyro bias covariance are each set to $P_{bias} = 4I_{3 \times 3} (\text{deg/hr})^2$, the initial position covariance is set to $P_{pos} = 5I_{3 \times 3} \text{m}^2$ and the initial velocity covariance is set to $P_{vel} = 0.02I_{3 \times 3} (\text{m/s})^2$. The initial variance for the target position is set to $1,000 \text{m}^2$ and the velocity variance is set to $0.01 (\text{m/s})^2$. The initial variance for the true anomaly is set to $1 \times 10^{-4} (\text{rad})^2$, and the rate variance is set to $1 \times 10^{-4} (\text{rad/sec})^2$. The gyroscope and LOS measurements are both sampled at 10 sec intervals for 600 minutes. Also, $a = 1$ with $g = 4$, which gives four times the vector of MRPs for the error representation, and $\lambda = 1$ is chosen for these simulations. Figures 6.7 and 6.8 show that the target and chaser biases are estimated accurately. Figures 6.9 and 6.10 show the attitude errors and respective 3σ bounds derived from the UKF and the EKF filters. Figure 6.11 shows that the attitude norm errors are less than 10^{-1}deg . Figure 6.12, the estimated relative orbit, shows that the error is bounded by less than $\pm 0.5 \text{m}$ in three-dimensional space.

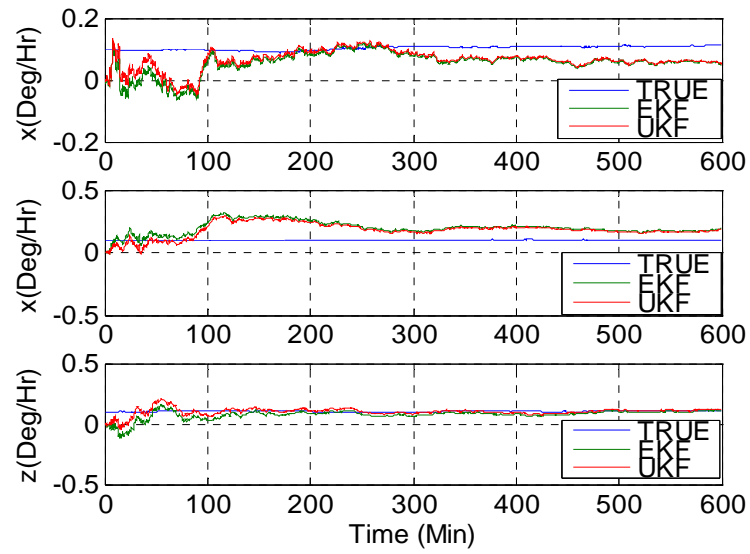


Figure 6.7. Target Gyro Bias Estimate.

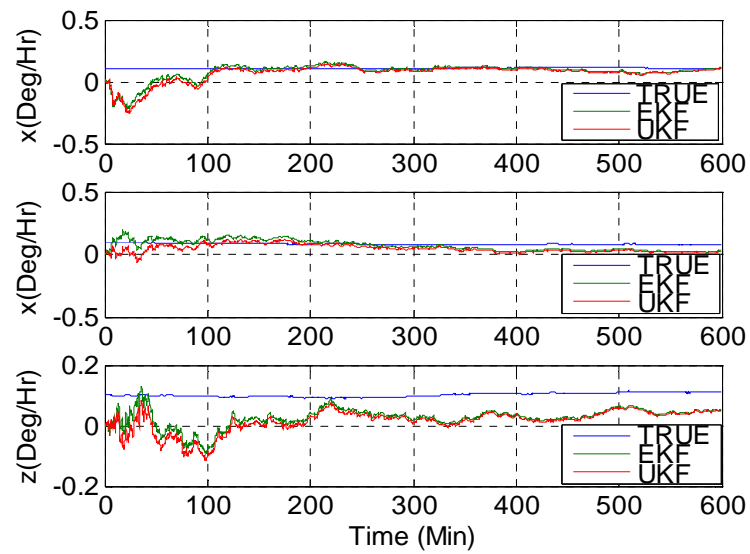


Figure 6.8. Chaser Gyro Bias Estimate.

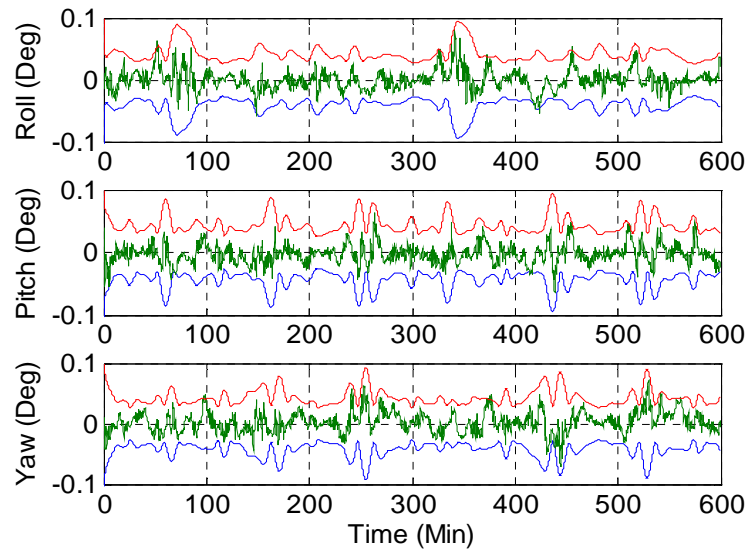


Figure 6.9. Attitude Errors and 3σ Bounds by EKF Filter.

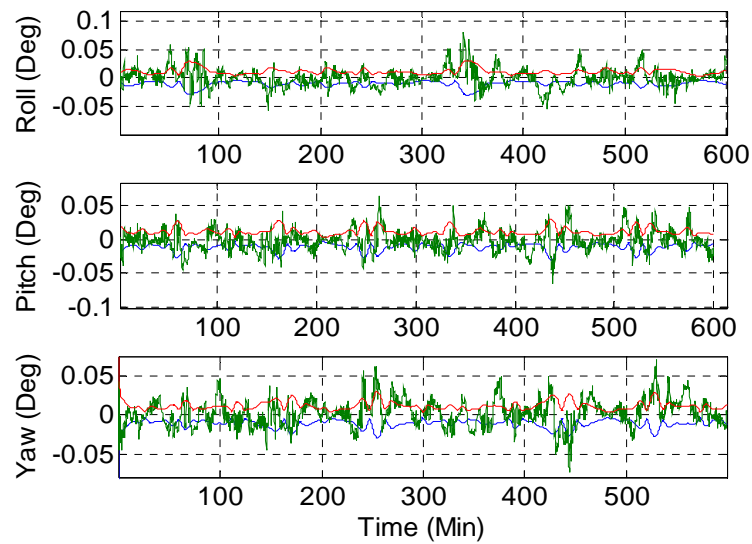


Figure 6.10. Attitude Errors and 3σ Bounds by UKF Filter.

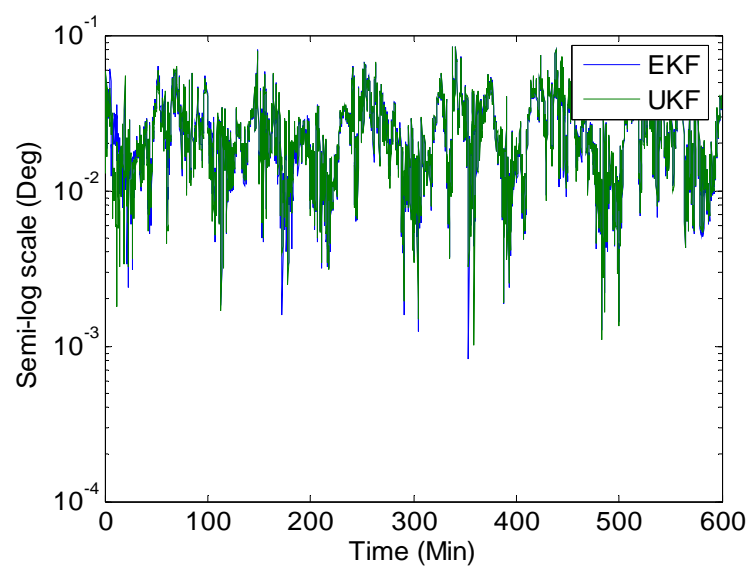


Figure 6.11. Attitude Error Norms.

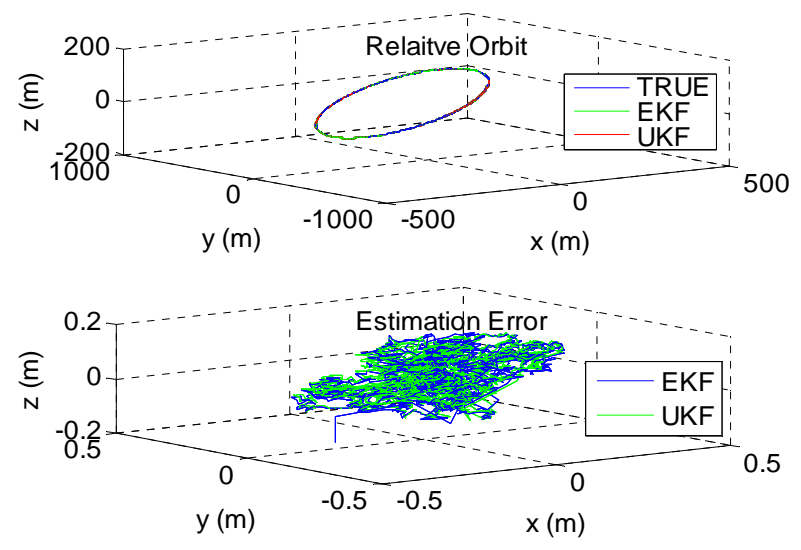


Figure 6.12. Estimated Relative Orbit and Error.

Figures 6.13 and 6.14 show the errors in relative position and velocity. There is no significant difference between the UKF and the EKF filters under this ideal condition. These results indicate that there are no advantages to the UKF filter in this case.

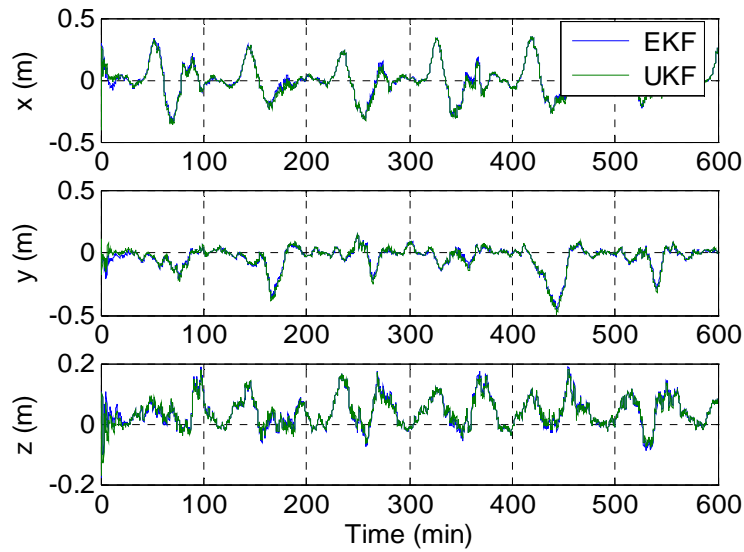


Figure 6.13. Relative Position Errors.

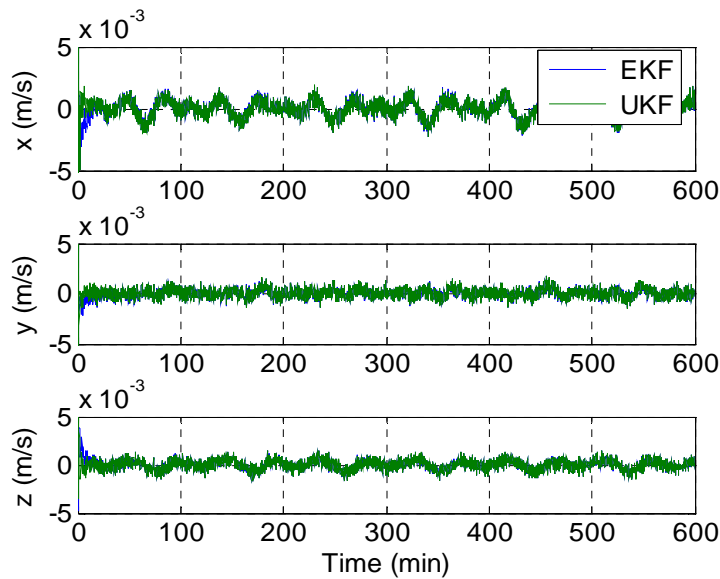


Figure 6.14. Relative Velocity Errors.

In the second simulation, errors of -10° in yaw, -15° in pitch and -25° in roll are added to the initial condition attitude estimate, with the bias estimate set to zero. The initial attitude covariance is set to $(20 \text{ deg})^2$, and the initial bias covariance is unchanged. Whereas the EKF filter never converges, the UKF filter converges to a value below 0.3

degree before one period of the target as shown in Figures 6.15 and 6.16. The attitude error norms using the EKF filter are too large.

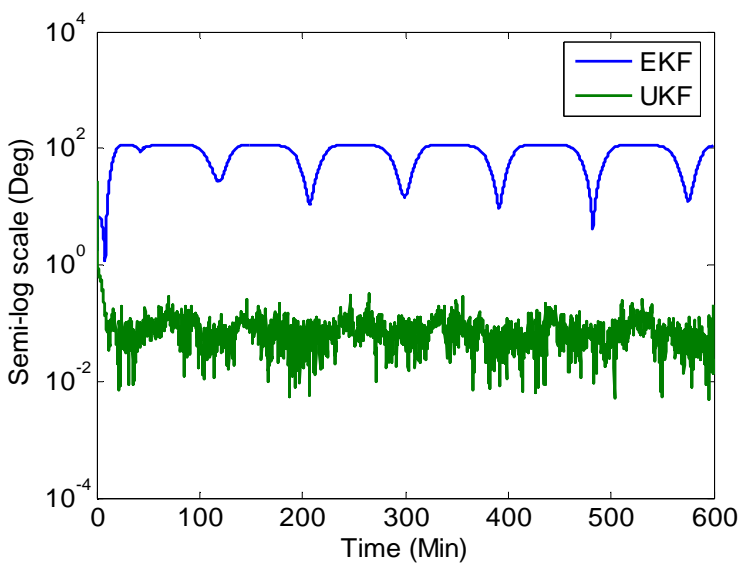


Figure 6.15. Attitude Error Norms.

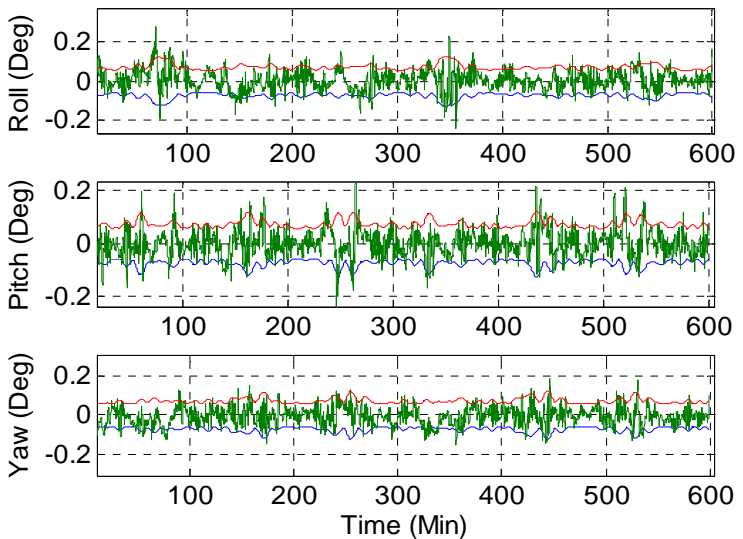


Figure 6.16. Attitude Errors and 3σ Bounds by UKF Filter.

In the third simulation, with initial biases set to zero, the initial attitude error is set back to zero. Errors of (10 m, -10 m and 10 m) are made in the initial relative position

and errors of (0.5 m/s, 0.5 m/s and 0.5 m/s) are made to the relative initial velocity. As in the second simulation, the EKF filter never converges to a value below 0.1 degree as shown in Figure 6.17, whereas the UKF filter converges to a value below 0.2 degree from the beginning as shown in Figure 6.18.

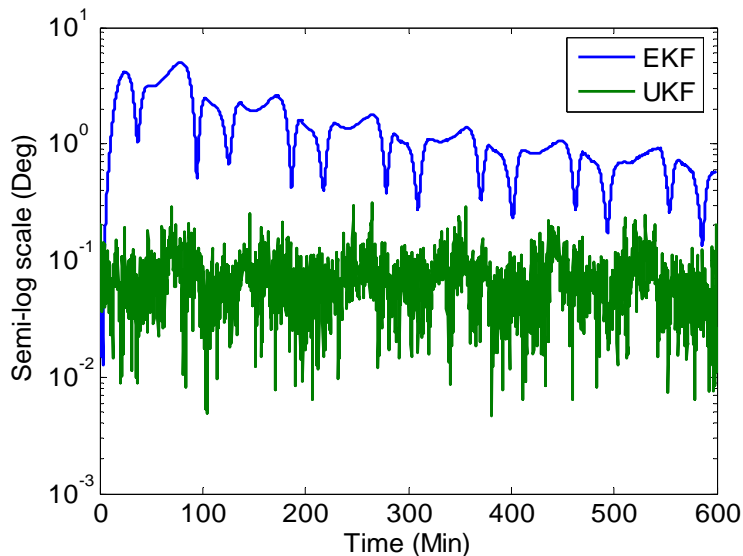


Figure 6.17. Attitude Error Norms.

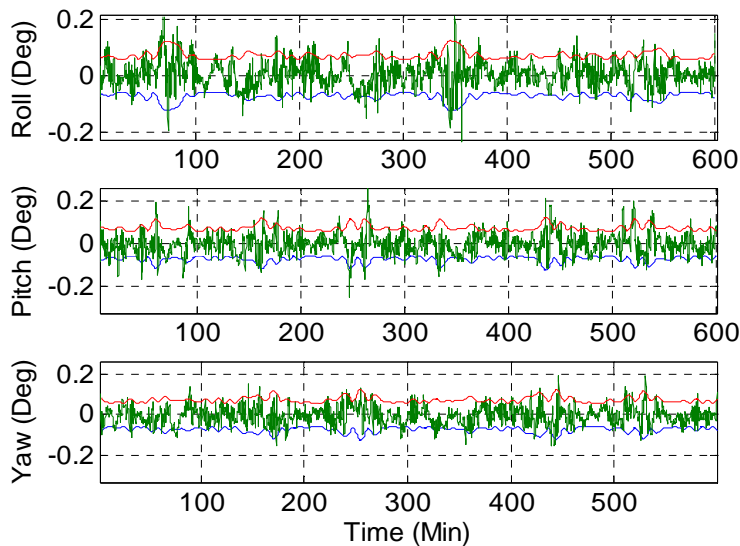


Figure 6.18. Attitude Errors and 3σ Bounds by UKF Filter.

The fourth simulation portrays the most realistic situation. All initial attitude, bias, position, and velocity errors are considered together as in the second and the third simulations. Estimation performance deterioration of the EKF filter is observed throughout the simulation, whereas the UKF filter converges as shown in Figures 6.19 and 6.20. In all these simulations, the UKF filter demonstrates its robustness under the initial error conditions.

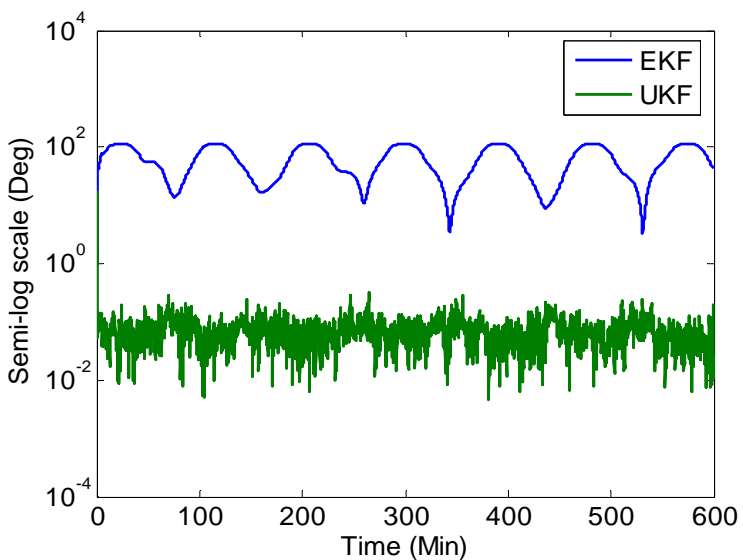


Figure 6.19. Attitude Error Norms.

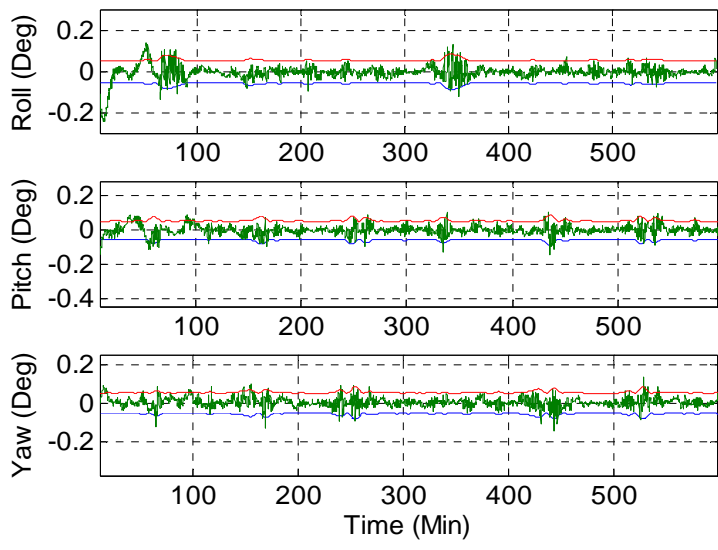


Figure 6.20. Attitude Errors and 3σ Bounds by UKF Filter.

6.6.2. Rendezvous Maneuver. Finally, this study tested a linear impulsive rendezvous maneuver [60]. The linear impulse rendezvous was performed at perigee of the chaser's orbit in order to effect rendezvous of the chaser with the target. The final relative velocity, of course, was required to be zero. The intercept was achieved at thirty minutes into the rendezvous transfer. This linear impulse rendezvous scenario was based on the CLJ transition matrix developed for an elliptical orbit [101]. The CLJ transition matrix is significantly more effective than the CW transition matrix in the generation of a reference trajectory for large elliptical orbits. Since the eccentricity of the target is very close to zero, the effect of using the CLJ transition matrix instead of the CW transition matrix is not significant. To facilitate extension of the rendezvous maneuver to an elliptical orbit, however, the CLJ transition matrix transition matrix was adopted here. The terminal time required to accomplish the linear impulse rendezvous is another important factor in this scenario. As the terminal time increases, the miss distance increases. Typically, rendezvous and docking maneuvers occur over one or two orbits, however, 30 minutes of terminal time was used in this scenario (close to one third of the target period in order to reduce the miss distance). The step size used in the rendezvous simulations is one second in contrast to the ten second step size used in bounded relative motion. First, the relative position and velocity for the intercept is calculated using the CLJ transition matrix at perigee of the chaser. The position and velocity are then substituted into Eq. (3), adding the Gaussian random noise with the spectral densities $\sqrt{10} \times 10^{-7} \text{ m}/(\text{s}\sqrt{\text{s}})$. Next, the relative attitude estimation, and the relative position and velocity estimations over the rendezvous sequence are tested and compared using both the UKF and the EKF filters under two simulation conditions.

The first simulation condition is the ideal condition adopted as the first case in Section A. Even under this ideal condition, the EKF filter did not converge from the beginning; rather, it converged near the terminal time shown in Figures 6.21, 6.22 and 6.23. The EKF filter shows deterioration of the sensitive estimations even under small initial bias errors. Figure 6.24 compares the rendezvous maneuver trajectory with respect to the true trajectory.

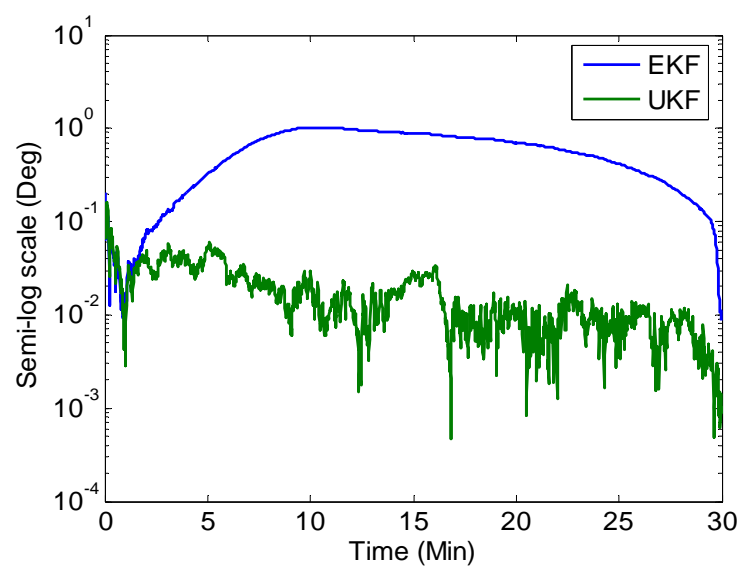


Figure 6.21. Attitude Error Norms.

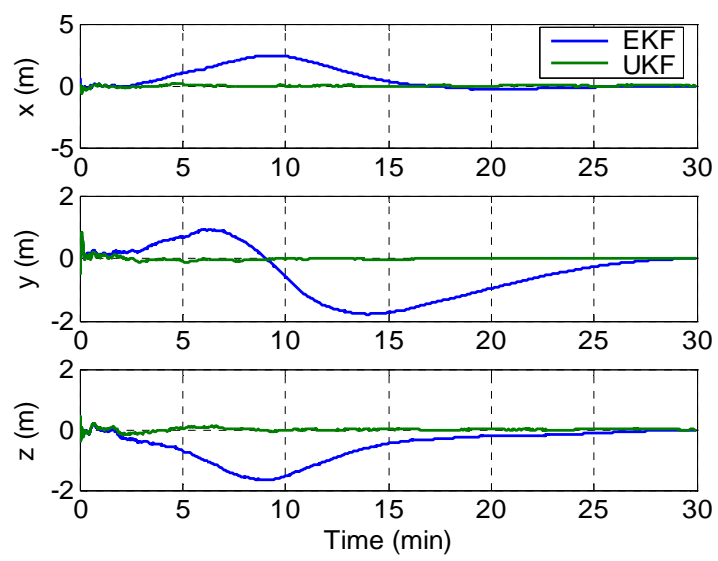


Figure 6.22. Relative Position Errors.

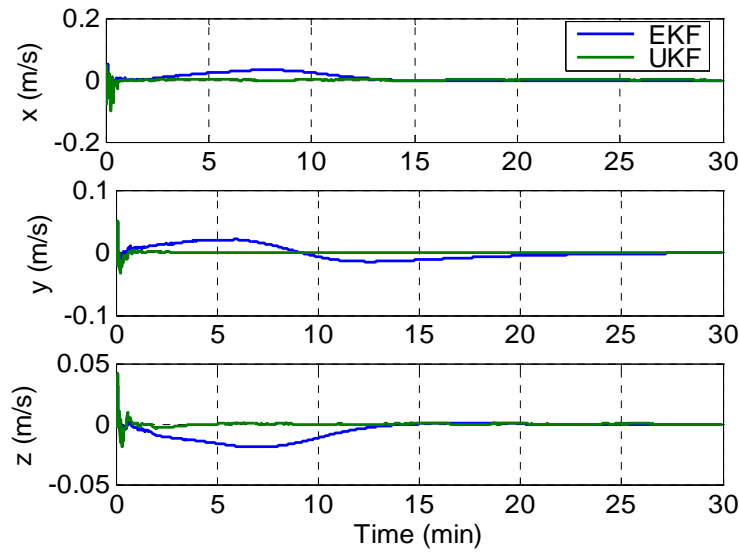


Figure 6.23. Relative Velocity Errors.

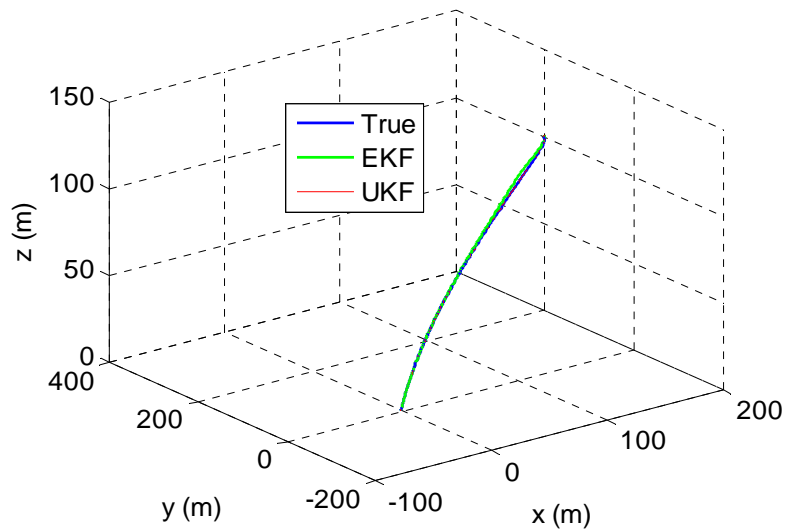


Figure 6.24. Rendezvous Maneuver Trajectory.

The second simulation condition is the most realistic; it was adopted from the fourth case in Section A. Figure 6.25 shows that the EKF filter never converged in attitude estimation, whereas the UKF filter converged from the beginning and estimated attitude more precisely as the chaser approached the target. Figures 6.26 and 6.27 show the relative position and velocity using the UKF filter only, and with similarity to Figure

6.26 shows that they are more accurately estimated near the terminal time. This is because the observations using the VISNAV system improve as the two spacecraft draw closer. Figure 6.26 shows that, unlike when using the UKF filter, the EKF filter-generated trajectory is significantly different from the true trajectory. The VISNAV-based state estimation using the UKF filter clearly demonstrates the robustness of the UKF filter under realistic initial conditions when applied to a rendezvous maneuver.

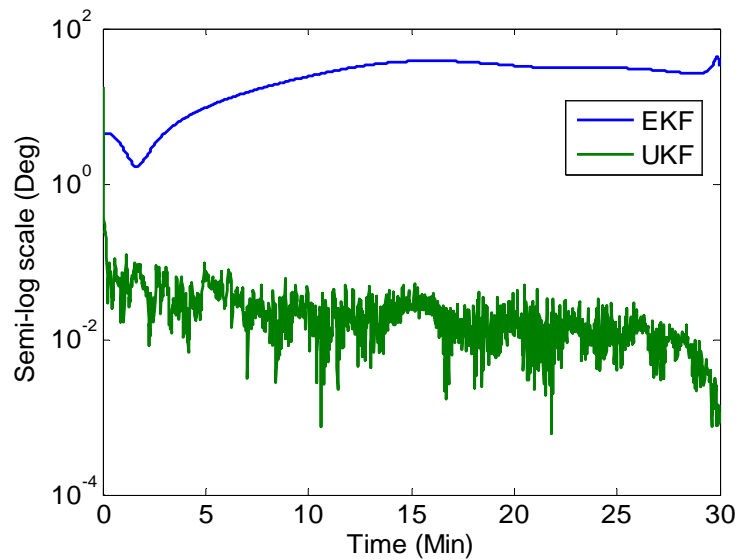


Figure 6.25. Attitude Error Norms.

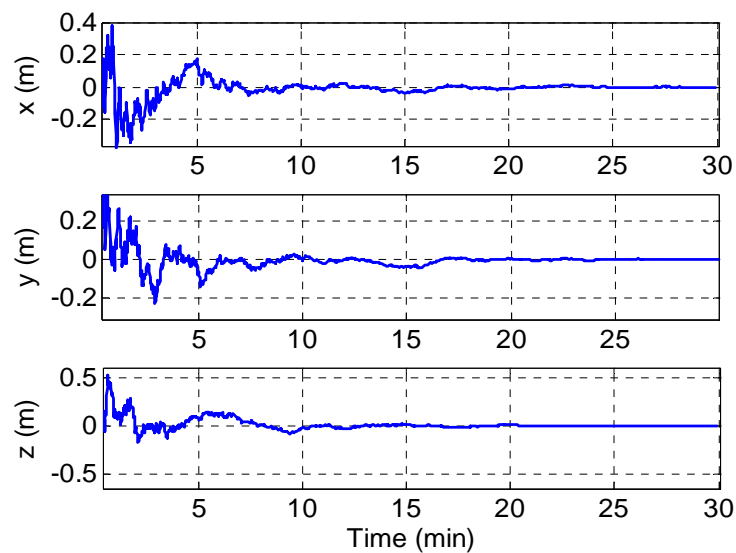


Figure 6.26. Relative Position Errors.

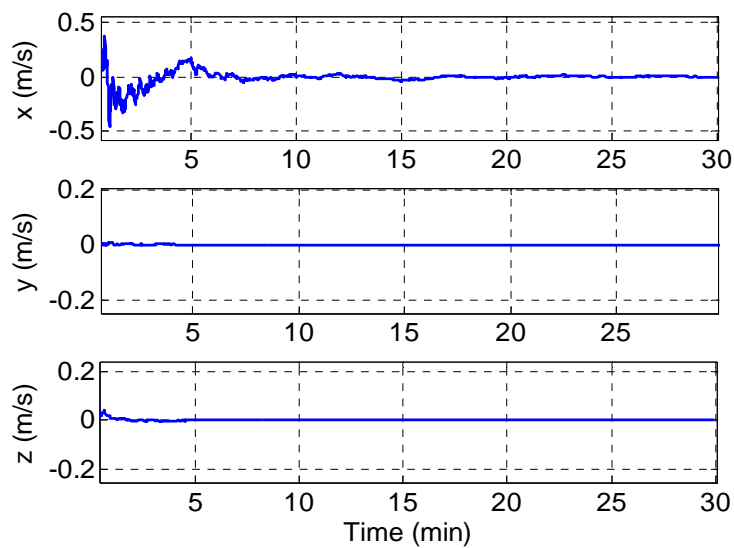


Figure 6.27. Relative Velocity Errors.

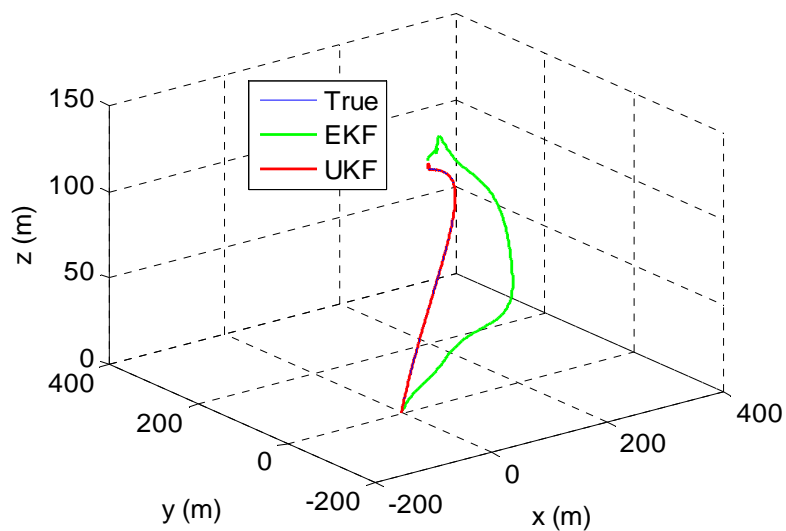


Figure 6.28. Rendezvous Maneuver Trajectory.

6.7. CONCLUSION

This work investigated a new approach to spacecraft relative attitude estimation and navigation based on use of the UKF filter, and evaluated the performance for bounded relative motion and rendezvous maneuvering. Since straightforward implementation of the UKF filter using quaternion kinematics does not maintain a unit

quaternion constraint, the quaternion was represented by a three-dimensional vector of generalized Rodrigues parameters. For the estimation of attitude information along with the relative position and velocity, the error-state vector was combined. The simulation results for the UKF filter are compared with those for the EKF filter. The UKF filter demonstrated its robustness and showed improved estimation results under realistic initial conditions with the initial errors. The states estimated by the UKF filter converged more quickly and precisely with the initial error conditions. The estimated relative position and velocity were validated by comparing them with the state computed from the two orbits generated by HPOP in STK. For the rendezvous maneuver, the reference trajectory was generated using the linear impulsive rendezvous based on the CLJ transition matrix, which is more effective in an elliptical orbit. This research shows that the suggested VISNAV system with the UKF filter provides precise relative attitude, and relative position and velocity under initial error conditions for bounded relative motion and rendezvous maneuvering.

7. CONTROL FUNCTION

In this section, three optimal control techniques are used for translational and rotational maneuvering. An SDRE tracking control for nonlinear relative dynamics and an LQT controller with free-final state for linear relative dynamics are both derived for translational maneuvering. An LQG-type controller is derived for rotational maneuvering. By using thrusters for translational and rotational control, both can be uncoupled to a high degree of approximation. However, a disturbance torque generated by thruster firing is considered as an unmodeled disturbance torque. The two controllers have different purposes but are executed simultaneously. The desired effect of the two controllers is illustrated in Figure 7.1.

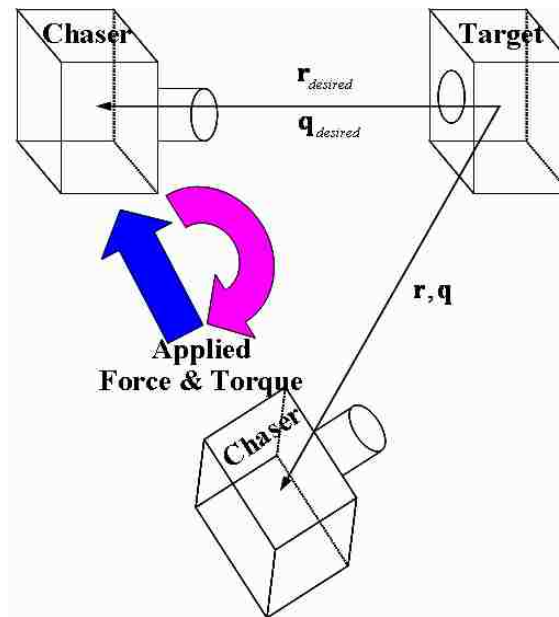


Figure 7.1. Desired Control Effect.

7.1. SDRE TRACKING FORMULATION FOR TRANSLATIONAL MOTION

Cloutier [68], [69] proposed the SDRE method [67-72], [77-81] for the first time for a nonlinear optimal regulation problem occurring in a broad class of nonlinear systems. An extended linearization, also known as state-dependent coefficient (SDC)

parameterization, is the process of factorizing a nonlinear system into a linear-like structure containing the SDC form. Motivated by the LQR method [71], [72], which is characterized by the solution to the algebraic Riccati equation (ARE), SDRE feedback control is an extended linearization control method that provides an approach similar to that of a nonlinear regulation problem. In a deterministic, infinite-horizon nonlinear optimal regulation problem in which the system is full-state observable, autonomous, and nonlinear in the state, a control law $\mathbf{u}(\mathbf{x})$ can be found to minimize the performance index. For reference trajectory tracking, the regulator problem must be recast as a tracking problem. The goal is to drive the error between the reference and the output to zero with minimum control energy. The tracking problem is then formulated by this performance index as

$$J = \frac{1}{2} \int_0^{\infty} \left\{ (\mathbf{x}^T(t) - \mathbf{x}_r^T(t)) Q(\mathbf{x}) (\mathbf{x}^T(t) - \mathbf{x}_r^T(t)) + \mathbf{u}^T(\mathbf{x}) R(\mathbf{x}) \mathbf{u}(\mathbf{x}) \right\} dt \quad (133)$$

$$\dot{\mathbf{x}} = \mathbf{f}(\mathbf{x}) + B(\mathbf{x})\mathbf{u}(\mathbf{x}) \quad (134a)$$

$$\mathbf{f}(\mathbf{x}) = A(\mathbf{x})\mathbf{x} \quad (134b)$$

where $\mathbf{x}_r(t)$ is the reference or desired state vector provided by the guidance scheme based on the CW state transition matrix [61-62] and the straight line V-bar approach [63]. The matrix $Q(\mathbf{x})$ is real symmetric positive semi-definite and $R(\mathbf{x})$ is a real symmetric positive definite matrix. If $\mathbf{f}(\mathbf{x})$ is a continuously differentiable function of \mathbf{x} , there is an infinite number of ways to factor $\mathbf{f}(\mathbf{x})$ into $A(\mathbf{x})\mathbf{x}$. For a valid solution to the SDRE, the pair $\{A(\mathbf{x}), B(\mathbf{x})\}$ must be pointwise stabilizable in the linear sense for all \mathbf{x} in the domain of interest. In order to perform tracking, the SDRE controller can be implemented as an integral servomechanism as demonstrated in Cloutier and Stansbery [68], [69]. However, this work adopts the approach that does not require increasing the state dimension. The SDRE approach for obtaining a suboptimal solution to the nonlinear problem can be summarized with the following steps:

- i) Use the direct parameter method to bring the nonlinear equation into SDC form as in Eq. (134);

ii) Solve the SDRE

$$P(\mathbf{x})A(\mathbf{x}) + A^T(\mathbf{x})P(\mathbf{x}) - P(\mathbf{x})B(\mathbf{x})R^{-1}(\mathbf{x})B^T(\mathbf{x})P(\mathbf{x}) + Q = 0 \quad (135)$$

iii) Construct the nonlinear feedback controller equation

$$\mathbf{u}(\mathbf{x}) = -R^{-1}(\mathbf{x})B^T(\mathbf{x})P(\mathbf{x})[\mathbf{x}(t) - \mathbf{x}_r(t)] \quad (136)$$

iv) The resulting SDRE controlled trajectory becomes the solution of the quasi-linear closed-loop dynamics

$$\dot{\mathbf{x}}(t) = A(\mathbf{x})(t) - B(\mathbf{x})R^{-1}(\mathbf{x})B^T(\mathbf{x})P(\mathbf{x})[\mathbf{x}(t) - \mathbf{x}_r(t)] \quad (137)$$

such that the state-feedback gain for minimizing Eq. (21) is

$$K(\mathbf{x}) = R^{-1}(\mathbf{x})B^T(\mathbf{x})P(\mathbf{x}) \quad (138)$$

The spacecraft translational maneuvering is accomplished through the use of the control force $\mathbf{F}_s \in R^3$. The nonlinear equations of the spacecraft dynamics in Eq. (9) are written in state-space form in the form of Eq. (134a) to give

$$\dot{\mathbf{x}} = \begin{bmatrix} \dot{x} \\ \dot{y} \\ \dot{z} \\ \ddot{x} \\ \ddot{y} \\ \ddot{z} \end{bmatrix} = \begin{bmatrix} \dot{x} \\ \dot{y} \\ \dot{z} \\ 2\dot{f}\left(\dot{y} - y\frac{\dot{r}_c}{r_c}\right) + x\dot{f}^2 + \frac{\mu}{r_c^2} - \frac{\mu}{r_d^3}(r_c + x) + \Delta\mathbf{a}_x \\ -2\dot{f}\left(\dot{x} - x\frac{\dot{r}_c}{r_c}\right) + y\dot{f}^2 - \frac{\mu}{r_d^3}y + \Delta\mathbf{a}_y \\ -\frac{\mu}{r_d^3}z + \Delta\mathbf{a}_z \end{bmatrix} + \begin{bmatrix} 0 & 0 & 0 \\ 0 & 0 & 0 \\ 0 & 0 & 0 \\ \frac{1}{m(t)} & 0 & 0 \\ 0 & \frac{1}{m(t)} & 0 \\ 0 & 0 & \frac{1}{m(t)} \end{bmatrix} \mathbf{u}(\mathbf{x}) \quad (139)$$

Through the SDC parameterization, the nonlinear equations are transformed to the linear-like state-space form in Eq. (134.b). The system matrix $A(\mathbf{x})$ is then

$$A(\mathbf{x}) = \begin{bmatrix} 0 & 0 & 0 & 1 & 0 & 0 \\ 0 & 0 & 0 & 0 & 1 & 0 \\ 0 & 0 & 0 & 0 & 0 & 1 \\ \left(\dot{f}^2 - \frac{\mu}{r_d^3} + \left(\frac{\mu}{r_c^2} - \frac{\mu}{r_d^3} r_c + \Delta \mathbf{a}(1) \right) / x \right) & \left(-2\dot{f} \frac{\dot{r}_c}{r_c} \right) & 0 & (2\dot{f}) & 0 & 0 \\ \left(2\dot{f} \frac{\dot{r}_c}{r_c} + \Delta \mathbf{a}(2) / x \right) & \left(\dot{f}^2 - \frac{\mu}{r_d^3} \right) & 0 & (-2\dot{f}) & 0 & 0 \\ 0 & 0 & \left(-\frac{\mu}{r_d^3} \right) & 0 & 0 & 0 \end{bmatrix} \quad (140)$$

where the denominator x must not be allowed to go to zero to avoid a singularity. The control distribution matrix is

$$B(\mathbf{x}) = \begin{bmatrix} 0 & 0 & 0 \\ 0 & 0 & 0 \\ 0 & 0 & 0 \\ \frac{1}{m(t)} & 0 & 0 \\ 0 & \frac{1}{m(t)} & 0 \\ 0 & 0 & \frac{1}{m(t)} \end{bmatrix} \quad (141)$$

The state weight matrix for the performance index in Eq. (133) is given by

$$Q = 10^4 \times \begin{bmatrix} I_{3 \times 3} & 0_{3 \times 3} \\ 0_{3 \times 3} & I_{3 \times 3} \end{bmatrix} \quad (142)$$

The control weight matrix is given by

$$R = 10 \times \begin{bmatrix} 1 & 0 & 0 \\ 0 & 1 & 0 \\ 0 & 0 & 1 \end{bmatrix} \quad (143)$$

The SDRE controller may not achieve the desired tracking error that is required at the final approach with the properly chosen initial weight matrices without causing the thruster saturation. If larger Q and smaller R weight matrices are chosen at the initial time, the controller may become saturated, resulting in control commands that cannot be executed by the thruster. To achieve the desired tracking error without thruster saturation occurring during the steady state or final approach phases, the weight matrices need to be adjusted from the initial weight matrices. When the weight matrices are adjusted at steady state, the control forces are modified and the tracking is then reduced to the desired value without thruster saturation. This adjustment of the weight matrices is very important in order to generate suitable control forces. When the weight matrices are adjusted, the adjusted Q weight matrix is then 1000 times the original Q weight matrix and the adjusted R weight matrix is 1/100 times the original R weight matrix. The implementation of the closed-loop optimal control for the SDRE tracking approach is shown in Figure 7.2. This control process is performed in real time.

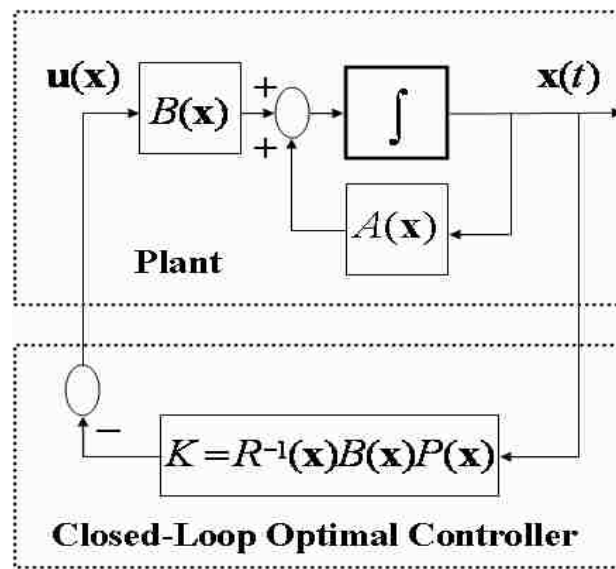


Figure 7.2. Implementation of the Closed-Loop Optimal Control.

7.2. LINEAR QUADRATIC TRACKING FORMULATION FOR TRANSLATIONAL MOTION

Tracking systems are required to track a desired trajectory in some optimal sense. Linear quadratic tracking (LQT) control with free-final state is developed to maintain the desired output with minimum control acceleration. A linear, observable system is given as

$$\dot{\mathbf{x}}(t) = A(t)\mathbf{x}(t) + B(t)\mathbf{u}(t) \quad (144.a)$$

$$\mathbf{y}(t) = C(t)\mathbf{x}(t) \quad (144.b)$$

where $\mathbf{x}(t)$ is the n^{th} order state vector, $\mathbf{u}(t)$ is the r^{th} order control, and $\mathbf{y}(t)$ is the m^{th} order output vector. The error vector becomes

$$\mathbf{e}(t) = \mathbf{x}_r(t) - \mathbf{y}(t) \quad (145)$$

The objective is to control the system in Eq. (145) such that the output $\mathbf{y}(t)$ tracks the reference state $\mathbf{x}_r(t)$ as closely as possible during the interval $[t_0, t_f]$ with minimum control effort with the chosen quadratic performance index as

$$J = \frac{1}{2} \left[\mathbf{e}(t_f)^T F(t_f) \mathbf{e}(t_f) \right] + \frac{1}{2} \int_{t_0}^{t_f} \left[\mathbf{e}(t)^T Q(t) \mathbf{e}(t) + \mathbf{u}(t)^T R(t) \mathbf{u}(t) \right] dt \quad (146)$$

and the boundary conditions defined as $\mathbf{x}(t_0) = \mathbf{x}_0$ and free $\mathbf{x}(t_f)$. The weight matrices, $F(t_f)$ and $Q(t)$ are symmetric positive semi-definite matrices, and $R(t)$ is a symmetric positive definite matrix. When $F(t_f)$ becomes large, a free final state becomes like a fixed final state. The optimal control law consists of the sum of two components given by

$$\begin{aligned} \mathbf{u}(t) &= -R^{-1}(t)B^T(t)[P(t)\mathbf{x}(t) - \mathbf{g}(t)] \\ &= -K(t)\mathbf{x}(t) + R^{-1}(t)B^T(t)\mathbf{g}(t) \end{aligned} \quad (147)$$

where the $n \times n$ symmetric, positive definite matrix $P(t)$ is the solution of the nonlinear, matrix differential Riccati equation (DRE) [71], [72], and the first term is a full-state feedback with Kalman gain. Thus

$$\dot{P}(t) = -P(t)A(t) - A(t)P(t) + P(t)B(t)R^{-1}(t)B^T(t) + R^{-1}(t)B^T(t)\mathbf{g}(t) \quad (148)$$

with the final condition

$$P(t_f) = C(t_f)F(t_f)C(t_f) \quad (149)$$

The n vector $\mathbf{g}(t)$ is the solution of the linear, nonhomogeneous vector differential equation

$$\dot{\mathbf{g}}(t) = -\left[A(t) - B(t)R^{-1}(t)B^T(t)P(t)\right]^T \mathbf{g}(t) - C^T(t)Q(t) \quad (150)$$

with the final condition

$$\mathbf{g}(t_f) = C(t_f)F(t_f)\mathbf{x}_r(t_f) \quad (151)$$

Whereas the SDRE equation is solved on-line, the DRE and the nonhomogeneous vector differential equations are solved off-line before control is performed. The optimal state is the solution of the linear state equation

$$\dot{\mathbf{x}}(t) = [A(t) - B(t)K(t)]\mathbf{x}(t) + B(t)R^{-1}(t)\mathbf{g}(t) \quad (152)$$

The spacecraft translational maneuver is performed through the use of the control force $\mathbf{F}_s \in R^3$. When the linearized equations of the spacecraft dynamics in Eq. (3) are adopted, the time varying system matrix $A(t)$ becomes

$$A(t) = \begin{bmatrix} 0 & 0 & 0 & 1 & 0 & 0 \\ 0 & 0 & 0 & 0 & 1 & 0 \\ 0 & 0 & 0 & 0 & 0 & 1 \\ \left(\dot{f}^2 + 2\frac{\mu}{r_c^3}\right) & (2\ddot{f}) & 0 & 0 & (2\dot{f}) & 0 \\ (-2\ddot{f}) & \left(\dot{f}^2 - \frac{\mu}{r_c^3}\right) & 0 & (-2\dot{f}) & 0 & 0 \\ 0 & 0 & \left(-\frac{\mu}{r_c^3}\right) & 0 & 0 & 0 \end{bmatrix} \quad (153)$$

The applied weight matrices $Q(t)$ and $R(t)$ in Eq. (146) are equal to the matrices in Eqs. 142 and 143. The weight matrix for the final state $F(t_f)$ is given by a relatively larger value than the value of $Q(t)$ to achieve the effect of the fixed-final state control.

$$F(t_f) = 10^9 \times \begin{bmatrix} I_{3 \times 3} & 0_{3 \times 3} \\ 0_{3 \times 3} & I_{3 \times 3} \end{bmatrix} \quad (154)$$

The implementation of the optimal tracking system is shown in Figure 7.3.

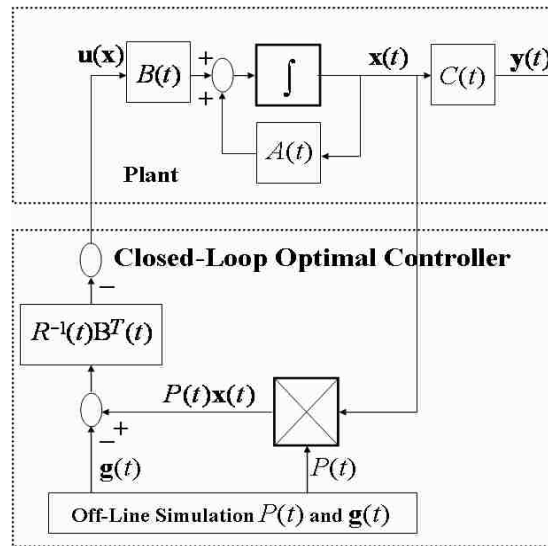


Figure 7.3. Implementation of Optimal Tracking System.

7.3. LINEAR QUADRATIC GAUSSIAN-TYPE CONTROL FORMULATION FOR TRANSLATIONAL MANEUVERS

The SDRE controller incorporates the EKF filter for relative position and velocity estimation, and guidance for the reference state. The SDRE controller is then transformed into an LQG- type controller [71-73]. Guidance, navigation and control functions are integrated into a feedback closed-loop system. This system becomes a key component of the integrated GNC system. The controller equations in Eqs. (136) and (138) are modified to

$$\mathbf{u}(\mathbf{x}) = -K(\mathbf{x})[\hat{\mathbf{x}}(t) - \mathbf{x}_r(t)] \quad (155)$$

where the controlled state $\mathbf{x}(t)$ is replaced by the estimated state $\hat{\mathbf{x}}(t)$ and $K(\mathbf{x})\mathbf{x}_r(t)$ is the feed-forward term. The optimal solution with the partial state information is given by using the SDC form of the state equation in Eq. (134). For a valid replacement, the separation principle must be met. Since the SDRE controller is in a linear-like structure, and is controllable and observable, it meets the condition for the separation principle. This validates the design for LQG-type controller. A block diagram of the LQG-type control is shown in Figure 7.4 The control commands for the translational maneuverings are then determined autonomously on the basis of the state estimation by the navigation function and predefined reference state by the guidance function.

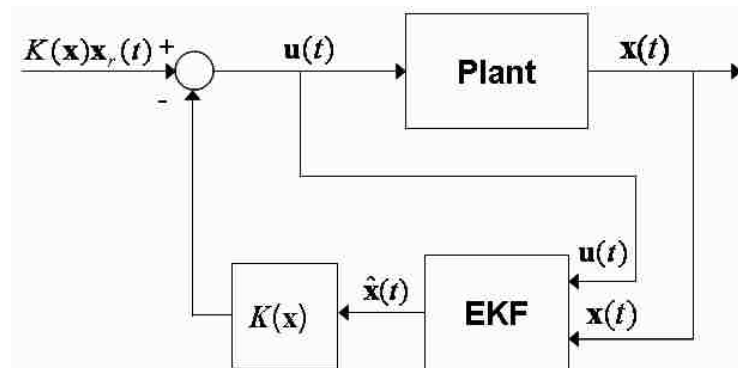


Figure 7.4. Linear Quadratic Gaussian-Type Controller.

7.4. LINEAR QUADRATIC GAUSSIAN-BASED CONTROL FORMULATION FOR ROTATIONAL MANEUVER

This section describes some properties of quaternions that make it possible to realize an exact linearization of the error dynamics formulation. An LQR approach with linearized dynamics developed by Paielli and Bach [75], [76] presents an optimal control design that provides linearized closed-loop error dynamics for tracking a desired quaternion. This study adopts this linearized equation to take advantage of the simplified equation of motion used to determine the precise attitude control. The control law formulation using LQR is combined with the EKF filter for the rotational maneuvers, which leads to an LQG-type controller which was used for controlling the translational motion. The chaser body-fixed frame must coincide with the target body-fixed frame at the moment of docking. The goal is to drive the state to zero with minimum control acceleration. The regulator problem is then formulated with the performance index

$$J = \frac{1}{2} \int_0^{\infty} \left\{ \mathbf{x}^T(t) \mathcal{Q}_{rotation}(t) \mathbf{x}^T(t) + \mathbf{u}^T(\mathbf{x}) R_{rotation}(t) \mathbf{u}(\mathbf{x}) \right\} dt \quad (156)$$

The kinematic equation for the desired or reference quaternion \mathbf{q}_d is given by

$$\dot{\mathbf{q}}_d = \frac{1}{2} \Xi(\mathbf{q}_d) \boldsymbol{\omega}_d \quad (157)$$

where $\boldsymbol{\omega}_d$ is the desired angular velocity vector and \mathbf{q}_d is assumed to be provided by the target onboard navigation. The error quaternion is defined as

$$\delta \mathbf{q} = \mathbf{q} \otimes \mathbf{q}_d^{-1} \quad (158)$$

where the variable \mathbf{q} is equal to the chaser quaternion, \mathbf{q}_c in the previous section. Then, $\delta \mathbf{p}$ and $\delta \mathbf{q}_4$ can be shown to be given by

$$\delta\mathbf{p} = \Xi(\mathbf{q}_d)^T \mathbf{q} \quad (159a)$$

$$\delta q_4 = \mathbf{q}_d^T \mathbf{q} \quad (159b)$$

As the actual quaternion approaches the desired quaternion, $\delta\mathbf{q}$ approaches zero. Some properties of the quaternion error measure are described below, making it possible to develop an exact linearization of the error dynamics for either formulation. Assume that the closed-loop dynamics have the linear form [75], [76]

$$\delta\ddot{\mathbf{p}} + L_2\delta\dot{\mathbf{p}} + L_1\delta\mathbf{p} = 0 \quad (160)$$

where L_1 and L_2 are 3×3 gain matrices. These matrices can be determined using an LQR approach

$$\delta\dot{\mathbf{p}} = \mathbf{u} \quad (161)$$

with

$$\mathbf{u} = -L \begin{bmatrix} \delta\mathbf{p} \\ \delta\dot{\mathbf{p}} \end{bmatrix} \quad (162)$$

where $L = [L_1 \quad L_2]$. The state space formulation of Eq. (160) is given by

$$\dot{\mathbf{x}}_{rotational} = \begin{bmatrix} \mathbf{0}_{3 \times 3} & I_{3 \times 3} \\ \mathbf{0}_{3 \times 3} & \mathbf{0}_{3 \times 3} \end{bmatrix} \mathbf{x}_{rotational} + \begin{bmatrix} \mathbf{0}_{3 \times 3} \\ I_{3 \times 3} \end{bmatrix} \mathbf{u} \quad (163)$$

where $\mathbf{x}_{rotational} = [\delta\mathbf{p}^T \quad \delta\dot{\mathbf{p}}^T]^T$. The notation $\mathbf{x}_{rotational}$ is used here differentiate from the state \mathbf{x} used to describe translational maneuvers. The state weight matrix for the performance index in Eq. (156) is given by

$$Q_{rotation} = 10^{-4} \times \begin{bmatrix} I_{3 \times 3} & \mathbf{0}_{3 \times 3} \\ \mathbf{0}_{3 \times 3} & I_{3 \times 3} \end{bmatrix} \quad (164)$$

The control weight matrix is given by

$$R_{rotation} = 10^4 \times \begin{bmatrix} 1 & 0 & 0 \\ 0 & 1 & 0 \\ 0 & 0 & 1 \end{bmatrix} \quad (165)$$

Similarly to the way in which the weight matrices were adjusted at steady state for translational control, they are also adjusted at steady state to reduce the attitude tracking errors. The ARE is solved to compute a constant gain matrix. It is then required to find a control torque input \mathbf{T}_u from Euler's equations of motion using Eq. (24) that satisfies the linear form given in Eq. (166). Differentiating Eq. (159a) twice and then substituting into Eq. (160) gives

$$\Xi^T(\mathbf{q}_d)\ddot{\mathbf{q}} + [2\Xi^T(\dot{\mathbf{q}}_d) + L_2\Xi^T(\mathbf{q}_d)]\dot{\mathbf{q}} + [\Xi^T(\ddot{\mathbf{q}}_d) + L_2\Xi^T(\dot{\mathbf{q}}_d) + L_1\Xi^T(\mathbf{q}_d)]\mathbf{q} = 0 \quad (166)$$

Taking the time derivative of Eq. (21) leads to

$$\dot{\mathbf{q}} = \frac{1}{2}\Xi(\mathbf{q})\dot{\boldsymbol{\omega}} + \frac{1}{2}\Omega(\boldsymbol{\omega})\dot{\mathbf{q}} = \frac{1}{2}\Xi(\mathbf{q})\dot{\boldsymbol{\omega}} - \frac{1}{4}(\boldsymbol{\omega}^T\boldsymbol{\omega})\mathbf{q} \quad (167)$$

where the identity $\Omega^2(\boldsymbol{\omega}) = -(\boldsymbol{\omega}^T\boldsymbol{\omega})I_{4 \times 4}$ is used. An identical expression for the desired quaternion is also given as

$$\ddot{\mathbf{q}}_d = \frac{1}{2}\Xi(\mathbf{q}_d)\dot{\boldsymbol{\omega}}_d + \frac{1}{2}\Omega(\boldsymbol{\omega})\dot{\mathbf{q}} = \frac{1}{2}\Xi(\mathbf{q}_d)\dot{\boldsymbol{\omega}}_d - \frac{1}{4}(\boldsymbol{\omega}_d^T\boldsymbol{\omega}_d)\mathbf{q}_d \quad (168)$$

where $\dot{\boldsymbol{\omega}}_d$ can be derived from Euler's equations of motion using Eq. (24) except for the unknown external disturbance torque \mathbf{T}_d . Substituting Eq. (24) into Eq. (168) gives

$$\ddot{\mathbf{q}} = -\frac{1}{2}\Xi(\mathbf{q})J^{-1}[\boldsymbol{\omega} \times]J\boldsymbol{\omega} - \frac{1}{4}(\boldsymbol{\omega}^T \boldsymbol{\omega})\mathbf{q} + \frac{1}{2}\Xi(\mathbf{q})J^{-1}(\mathbf{T}_g) + \frac{1}{2}\Xi(\mathbf{q})J^{-1}\mathbf{T}_u \quad (169)$$

Substituting Eq. (24) and Eq. (168) into Eq. (166), and solving for \mathbf{T}_u yields [57]

$$\mathbf{T}_u = [\boldsymbol{\omega} \times]J\boldsymbol{\omega} - \mathbf{T}_g + 2J\left[\Xi^T(\mathbf{q}_d)\Xi(\mathbf{q})^{-1}\right]^{-1} \left\{ \begin{array}{l} \frac{1}{4}(\boldsymbol{\omega}^T \boldsymbol{\omega})\Xi^T(\mathbf{q}_d) - \Xi^T(\dot{\mathbf{q}}_d)\Omega(\boldsymbol{\omega}) \\ -\Xi^T(\ddot{\mathbf{q}}_d) - L_1\Xi^T(\mathbf{q}_d) - L_2\left[\Xi^T(\mathbf{q}_d)\Omega(\boldsymbol{\omega}) + \Xi^T(\dot{\mathbf{q}}_d)\right] \end{array} \right\} \mathbf{q} \quad (169)$$

The quaternion \mathbf{q} in Eq. (169) is replaced by the estimated quaternion $\hat{\mathbf{q}}$ from the navigation process, and the control \mathbf{T}_u becomes an LQG-type control.

7.5. NUMERICAL RESULTS AND ANALYSIS

This study tested the controllers developed here in a Shuttle-like scenario in which the proximity operations and docking historically have been performed by the crew in the manual phase flight segment as shown in Figure 7.5. A six degrees-of-freedom simulation and a passive target (e.g., the ISS) were created to demonstrate the performance of the controllers. The ultimate objective was to have the chaser (e.g., Shuttle) docking port approach the target docking port leading to soft docking with the desired attitude. There are two types of axis alignments during this phase. The first one is the same direction of axis alignment illustrated by Figure 7.5 (a) and (b). The second one is the +90 degree chaser pitch rotation illustrated by Figure 7.5(a) and (c). The target quaternions \mathbf{q}_t were found through the use of the quaternion kinematic equations. The target angular velocity was assumed to be constant during the scenario. The target's inertia matrix was assumed as [63]

$$I_{target} = \begin{bmatrix} 128 \times 10^6 & 0 & 0 \\ 0 & 107 \times 10^6 & 0 \\ 0 & 0 & 201 \times 10^6 \end{bmatrix} \text{kg} \cdot \text{m}^2 \quad (170)$$

The chaser's inertia matrix was also assumed constant and taken as [102].

$$I_{chaser} = \begin{bmatrix} 1.091 \times 10^6 & -0.027 \times 10^6 & -0.008 \times 10^6 \\ -0.027 \times 10^6 & 8.287 \times 10^6 & -0.328 \times 10^6 \\ -0.008 \times 10^6 & -0.328 \times 10^6 & 8.646 \times 10^6 \end{bmatrix} \text{kg} \cdot \text{m}^2 \quad (171)$$

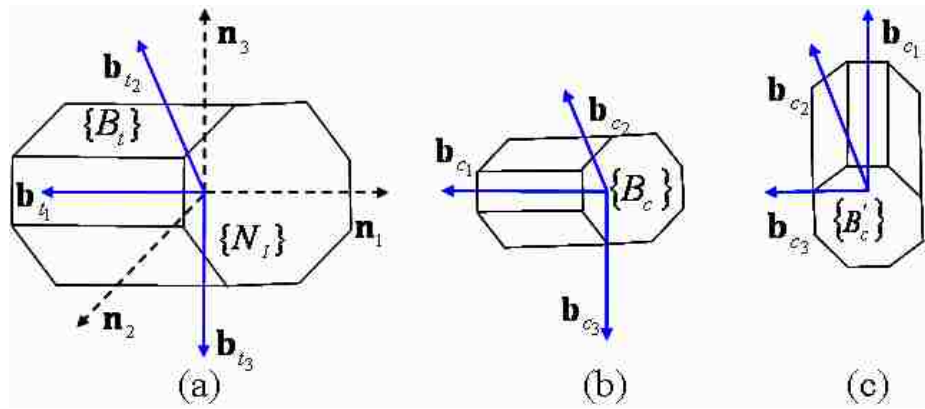


Figure 7.5. Geometry of Axis Alignment.

The chaser was initially located at the relative position $[609.6 \ 213.36 \ 0.1]$ m with a relative velocity $[0.01 \ -0.43 \ 0.01]$ m/s with respect to the target. The initial quaternion of the chaser was $[0.2473 \ 0.4123 \ 0.8651 \ 0.1426]$ whose initial attitude was -30 degree of pitch rotated with respect to the CW frame of chaser. The gyro noise parameters were specified as $\sigma_u = \sqrt{10} \times 10^{-10}$ rad/sec^{3/2} and $\sigma_{cv} = \sqrt{10} \times 10^{-7}$ rad/sec^{1/2} [66], [67]. The initial biases for each axis of gyros were 1 deg/hr [66]. The docking target location was given as $[27.30 \ 12.71 \ -2.74]$ m in the CW frame [59]. The crew's manual flight segment was divided into six total stages of subsegments. The first two are the R-bar approach from the initial point; the third is the first stationkeeping location; the fourth is the V-bar approach; the fifth is the second stationkeeping location; and final subsegment is the straight line V-bar approach intended to accomplish soft docking. There are two stationkeeping staging modes used before entering the docking phase. The simulation lasted for 68 minutes from the proximity operations holding point to the target docking

port with a 0.1 second of step size. Whereas the translational control is initialized according to each subsegment, attitude control is initialized twice to execute these axis alignments. Since the H-bar relative motion in this scenario was much smaller than R-bar and V-bar relative motions, a planar motion perspective is used to better illustrate the results. The translational maneuvering results were determined both by SDRE control and LQT control independently. The data were then plotted together from the holding point to the target docking port.

Figures 7.6 and 7.7 show proximity operation trajectories and out-of plane motions for the entire simulation duration. Using the CW guidance scheme and final straight line approach guidance with subcentimeter per second velocity, the reference trajectories are autonomously commanded to the controllers.

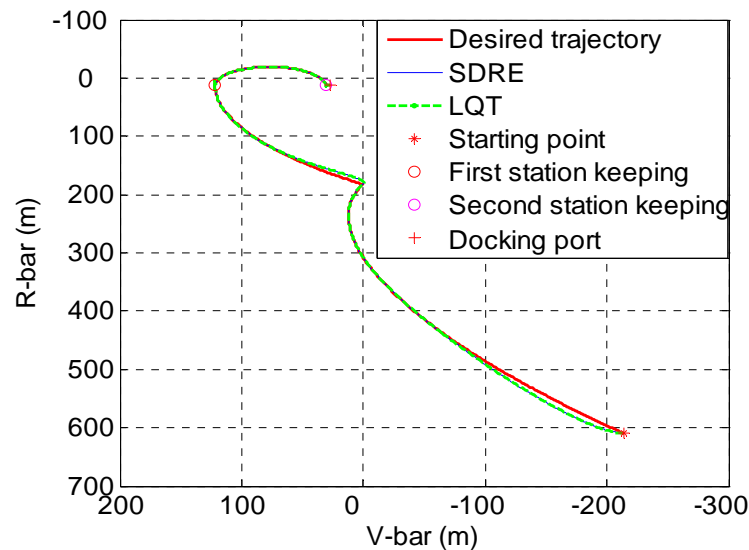


Figure 7.6. Proximity Operation Trajectories.

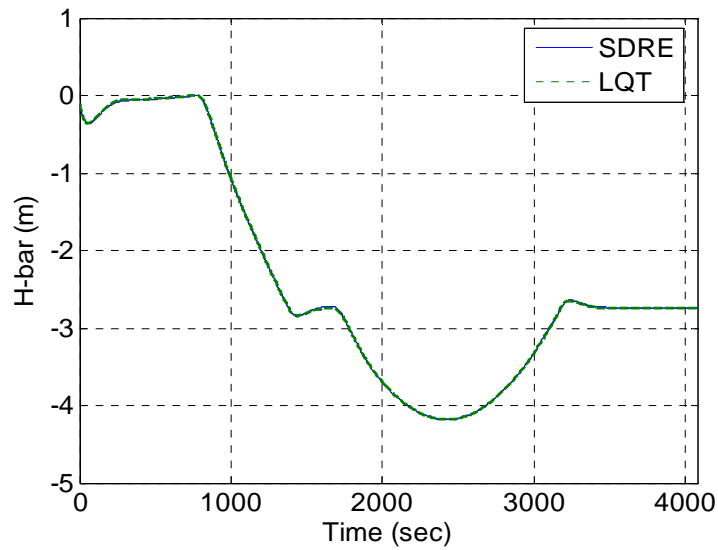


Figure 7.7. Out-of-Plane Relative Motion.

The transfer time and the nominal trajectory for the R-bar relative motion was determined by the CW terminal guidance scheme [60-63]. Figure 7.8 shows the first R-bar relative motion for thirteen minutes. As soon as each subsegment was complete, the newly initialized control was applied sequentially to the next subsegment.

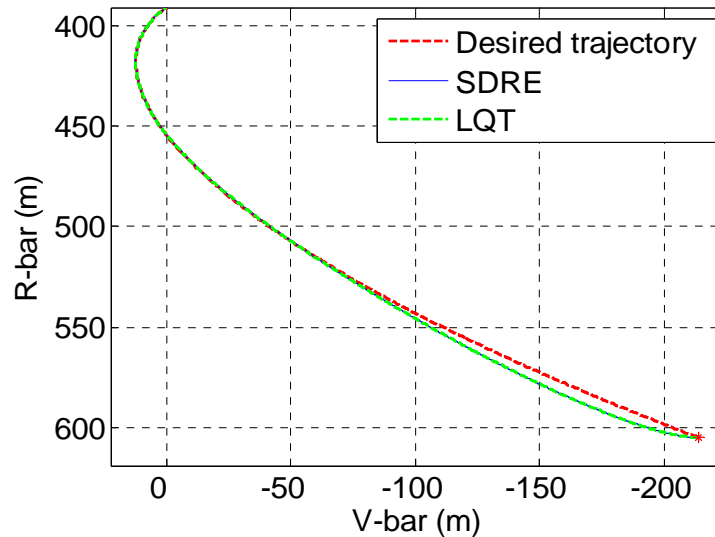


Figure 7.8. First R-Bar Approach.

For the second phase of the R-bar motion, the chaser spacecraft approached the line-of-sight (LOS) V-bar for ten minutes, shown in Figure 7.9

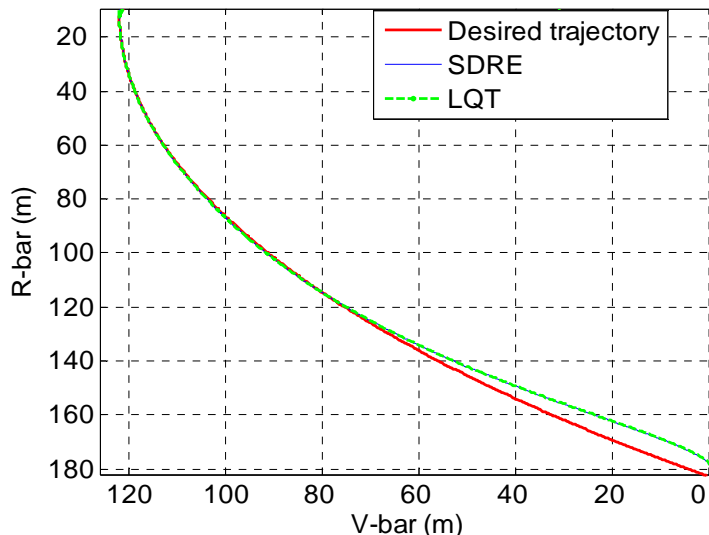


Figure 7.9. Second R-Bar Approach.

After the second subsegment was completed, a stationkeeping maneuver was executed to ensure the LOS capture for five minutes by nullifying the arrival velocity generated by the CW terminal guidance, shown in Figure 7.10. After the second R-bar approach is over, the chaser needs to capture the LOS to the docking port during the stationkeeping lasting five minutes. The time for nullifying the arrival velocity was predetermined by the simulation test using the exponential braking law [63]. The five minutes is enough time to achieve capturing the LOS during the stationkeeping phase. During the stationkeeping phase at the LOS, the chaser prepares for the straight LOS final approach phase and additional control forces were generated so that the chaser would not drift freely. After the first stationkeeping maneuver was complete, a V-bar hopping approach along the LOS was executed for twenty five minutes, shown in Figure 7.11. The nominal V-bar hopping trajectory and the transfer time were also determined by the CW terminal guidance scheme which was very fuel efficient. The chaser then executed the second stationkeeping maneuver before the straight LOS final approach, shown in Figure 7.12,

for five minutes. Unlike the first stationkeeping maneuver, the chaser's arrival velocity was opposite to that of the arrival velocity in the second R-bar maneuver. During the second stationkeeping maneuver, the chaser slows the arrival velocity, again captures the LOS to the docking port, and prepares for the straight LOS final approach.

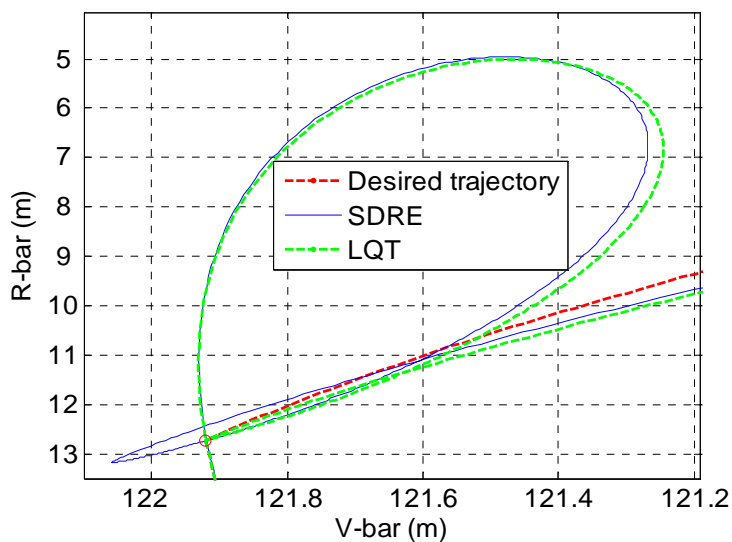


Figure 7.10. First Stationkeeping Subsegment.

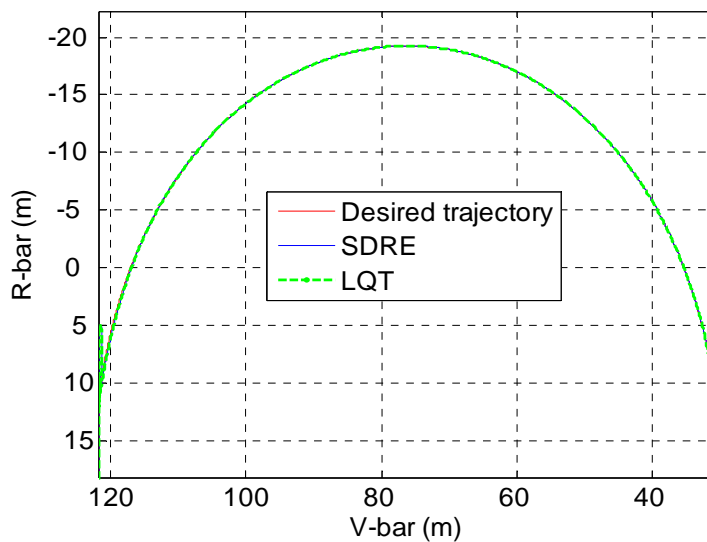


Figure 7.11. V-Bar Hopping Approach.

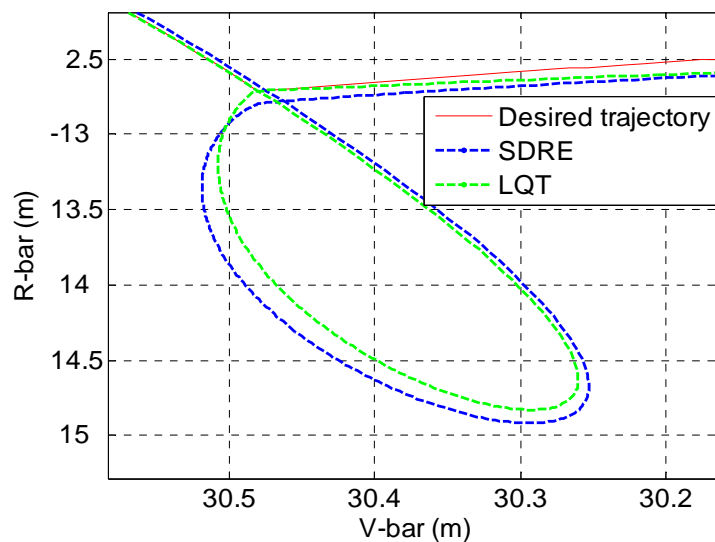


Figure 7.12. Second Stationkeeping Subsegment.

After the second stationkeeping phase was completed, the chaser spacecraft finally completes the straight line approach and docks with the target docking port, as shown in Figure 7.13. The straight line LOS final approach with very slow constant velocity was specified to ensure safety and avoid unacceptably high physical impact with the target.

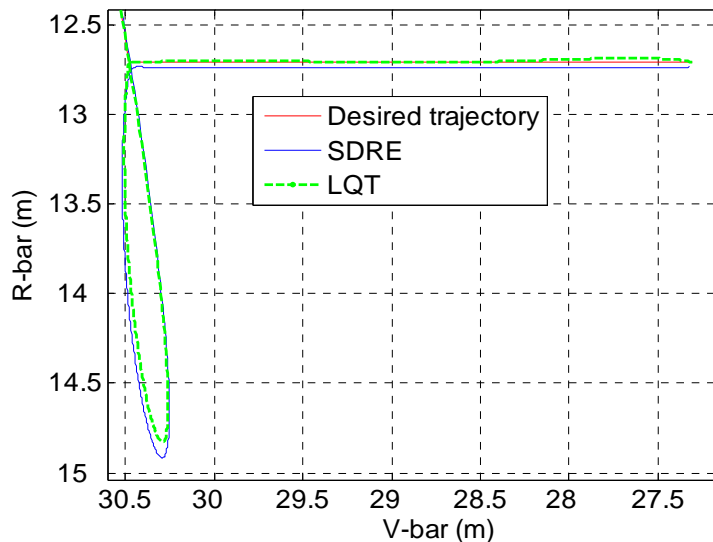


Figure 7.13. Straight LOS Final V-Bar Approach.

This straight LOS final approach also requires a relatively larger control force than the control required by the CW guidance scheme.

According to the conditions for entering the docking phase [58] proposed for the Shuttle and the ISS, lateral docking tolerance is maximum of a 0.330 m (13 inches), lateral velocity tolerance is 0.0457 m/s (0.15 ft/s), and closing velocity tolerance is 0.0914 m/s (0.30 ft/s). It is especially important to consider the position tracking error and approach range rate to investigate these conditions. For an improved inspection of them, the figures of the final straight line V-bar approach for ten minutes were magnified. Whenever the initialized control force was applied according to the subsegment, the tracking error starting from the higher value gradually decreased. This tracking error variation is acceptable to successfully perform this scenario. As the translational control was stabilized, the controlled state tracked the reference state more accurately. The SDRE control could achieve this accuracy after the weight matrices were adjusted in the final approach phase. In other words, additional control forces had to be produced to reduce the tracking errors. However, the LQT control with free-final state could achieve very precise position tracking at the final time by the use of a large weight matrix, $F(t_f)$ for the final state in Eq. (154) with no changes in the other weight matrices. By applying large weight matrix $F(t_f)$, the LQT control with free-final state could produce the result using the fixed-final state control [72]. Figure 7.14(a) shows position tracking error during the entire simulation. The approach trajectory using the SDRE control shows a constant straight-line trajectory whose error is less than 0.02 m, while the one using the LQT control with free-final state varied from about 0.14 m to 4×10^{-3} m at the final time, as shown in Figure 7.14(b).

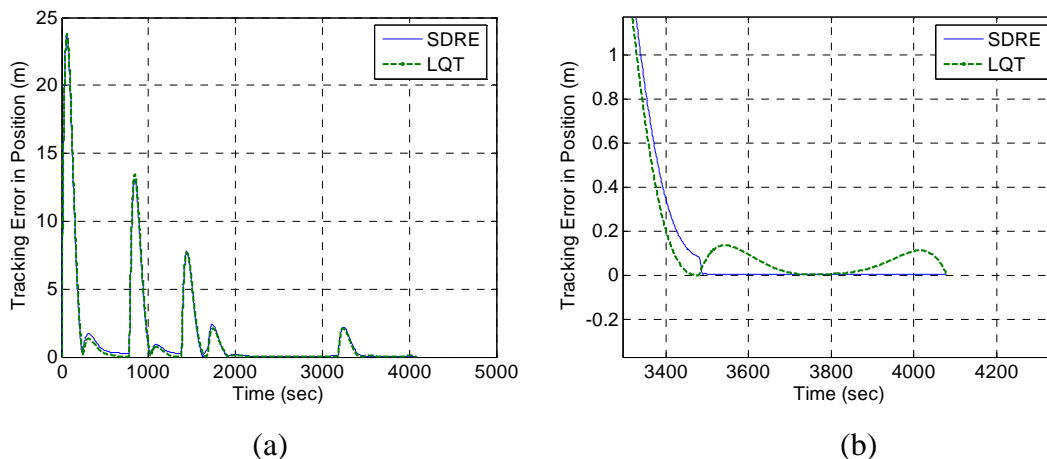


Figure 7.14. Position Tracking Error History.

The approach range rate using SDRE control, shown in Figure 7.15(a), converged to 0.0077 m/s, whereas the approach range rate using LQT control with free-final state, as shown in Figure 7.15(b), dropped to 0.0049 m/s.

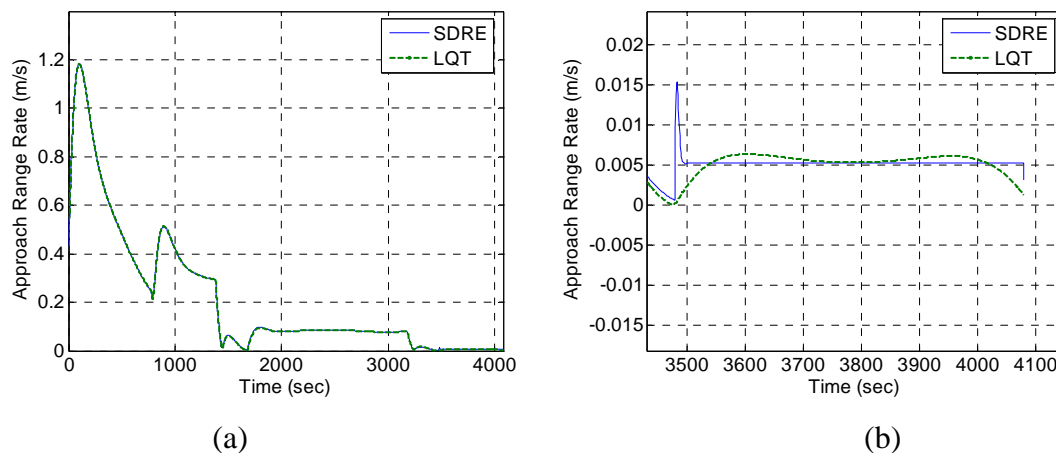


Figure 7.15. Approach Range Rate History.

The control force histories produced by the two controllers are shown in Figure 7.16. The figure also shows that the additional control forces that resulted from the adjustment of the weight matrices in the SDRE controller increased impulsively before

the final straight line approach. Unless these additional control forces are commanded by the SDRE controller, the position tracking error goes to up to about two meters in the final subsegment. The LQT control with free-final state shows that the chaser spacecraft more precisely approached each destination, shown in Figure 1.15 as S2, S3 and the docking port, than the SDRE controller did. The translational maneuvering by the SDRE controller based on the nonlinear system using the adjustment of the weight matrices at the straight LOS final approach could track the reference state provided by the straight-line guidance scheme and avoid thruster saturation. The tracking error was effectively reduced. Unlike LQT control with free-final state, the effects of relative perturbations were also considered in the SDRE approach in an attempt to control the translation more precisely. For precise translational maneuvering, the SDRE control based on the nonlinear system is preferable. As the control forces and torques are generated, the propellant mass is consumed, which changes the total mass and moment of inertia of the chaser. Figure 7.17 shows propellant mass consumption as a result of the applied control forces and control torques.

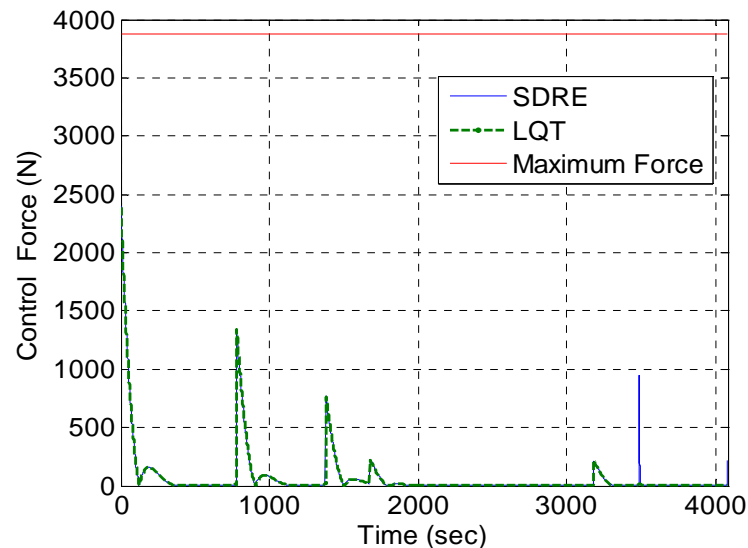


Figure 7.16. Control Force History.

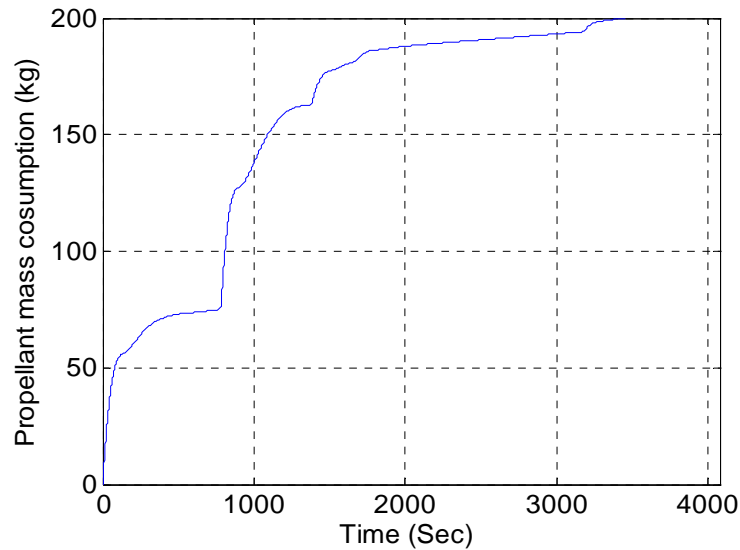


Figure 7.17. Propellant Mass Consumption.

This study assumed that the locations of all RCS thrusters are known so that the propellant consumption resulting from the control torques can be computed. The total consumed mass is the sum of the mass consumed by the control forces and the control torques. Because of the varying mass, the moment of inertia is not constant. The robustness of the rotational controller was evaluated considering the uncertainties of the moment of inertia. The uncertainty was quantified by adding thirty percent of initial moment of inertia to the initial value [103]. Moreover, external disturbances, which were not modeled in the controller, were added to the Euler rotational equation of the chaser in Eq. (24). All of the results to follow were compiled incorporating the moment of inertia uncertainty and the unmodeled external disturbances. The first rotational maneuver, illustrated by comparison of Figures 7.5(a) and 7.5(b), was executed to align the chaser body axis with the target body axis in the first segment. The second rotational maneuver, illustrated by comparing Figures 7.5(a) and 7.5(c), was performed up to the final subsegment after the first rotational maneuver was complete. Figure 7.18 shows that the chaser's quaternion tracking response exhibits good attitude tracking during the entire simulation. To illustrate the geometry of the angular motion more clearly, the Euler angle

history of the reference and chaser expressed with the 3-2-1 rotation sequence of the chaser converted from quaternions is shown in Figure 7.19.

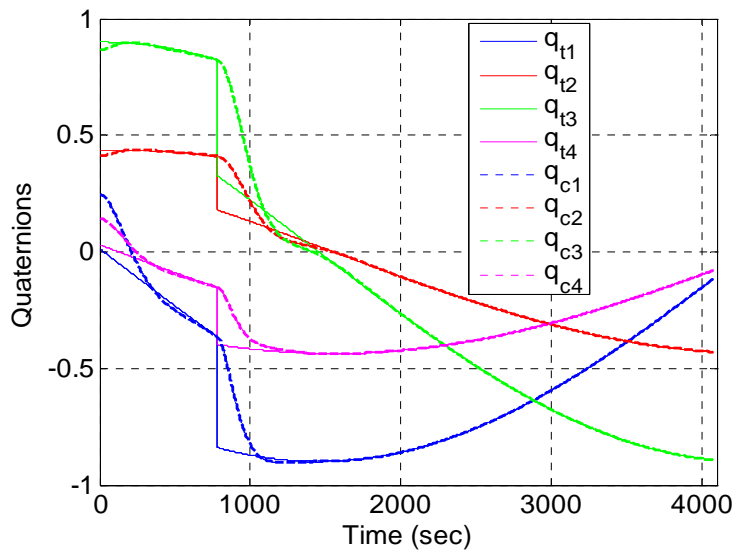


Figure 7.18. Target and Chaser Quaternion Histories.

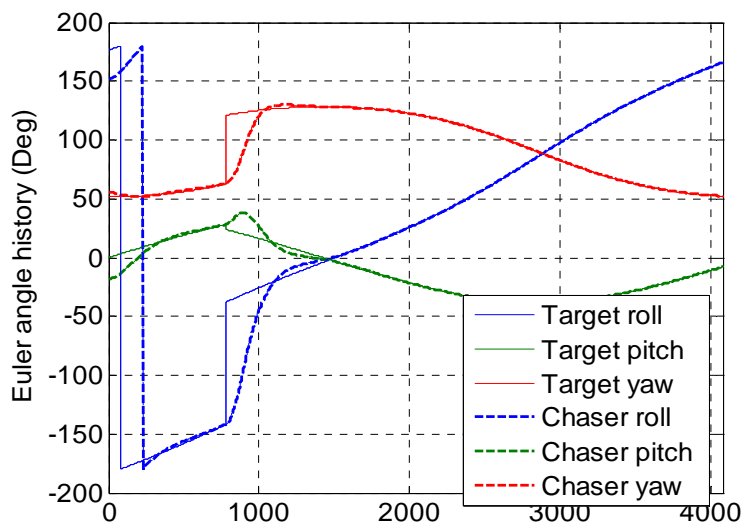


Figure 7.19. Euler Angle Histories.

Figure 7.20 shows the Euler angle error history between the target and chaser spacecraft and both axis alignments that are composed of 30 and 90 degree of pitch rotations. The

target is orbiting a near-circular, near-circular 350×450 km altitude Earth-pointing orbit. The target angular rate can then be expressed as $\boldsymbol{\omega}_t = [0 \quad n \quad 0]^T$ in the adopted body-frame where n is the mean motion of the target. This attitude control can be achieved using the chaser's precise attitude estimation using the sensors previously listed and the adjustment of weight matrices. The chaser spacecraft then maintains the desired attitude by using control torque continuously until the terminal time, leading to roll, pitch, and yaw errors of less than 0.1 deg. Figure 7.21 shows the nominal target angular rate that the chaser can track for the two different types of axis alignments which are illustrated in Figure 7.5. For efficient and quick axis alignment, the weight matrix was adjusted during the steady state interval as was done for the SDRE control. Even in the presence of unmodeled disturbance torques and the moment of inertia uncertainty, the controller could succeed in maintaining an acceptable attitude tracking error. The rotational maneuvers then met the alignment condition for the docking phase.

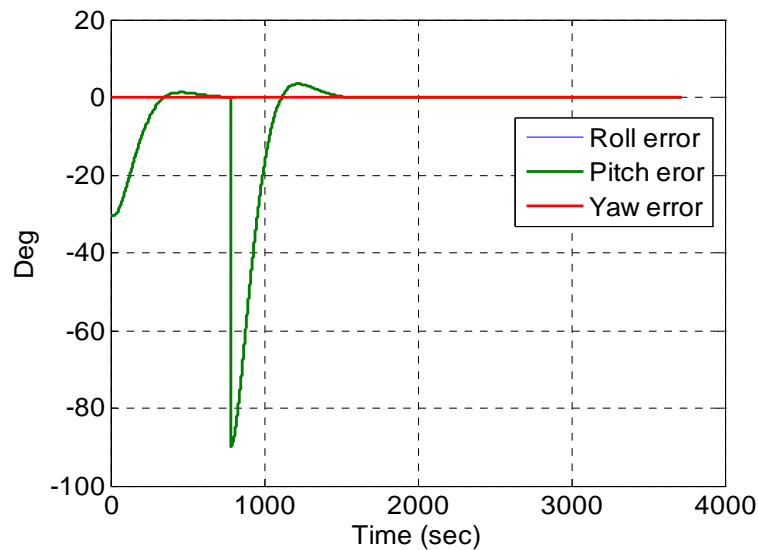


Figure 7.20. Euler Angle Error History.

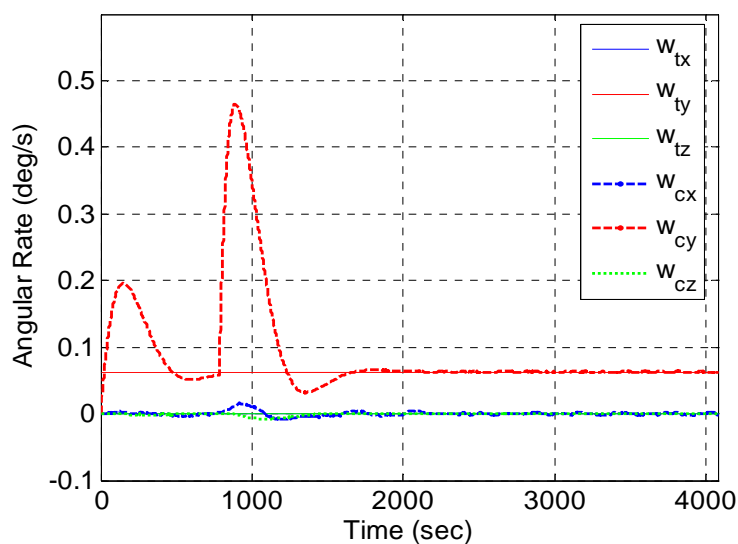


Figure 7.21 Angular Rate Histories.

The upper plot in Figure 7.22 shows the gravity-gradient torque history acting on the chaser and the lower plot shows the external disturbance torque history acting on the chaser simulated by white Gaussian-noise with mean $[10 \ 10 \ 10]^T$, both of which were added to Eq. (24).

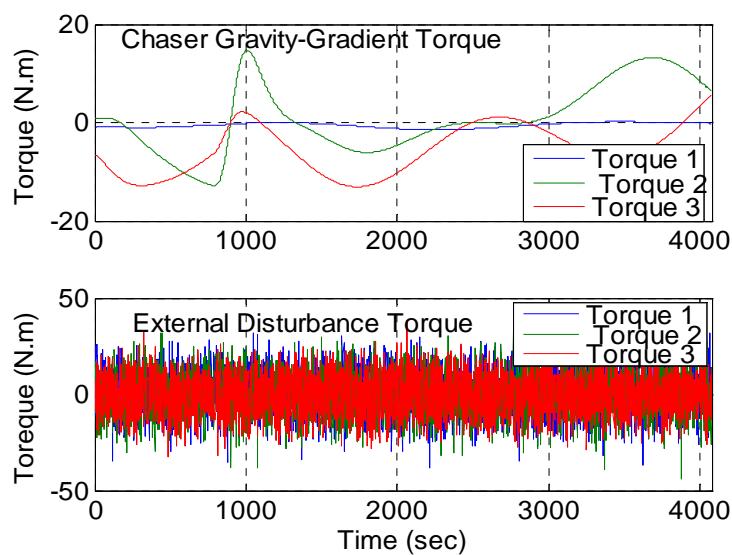


Figure 7.22. Chaser's Gravity-Gradient and External Torque Histories.

Figure 7.23 shows the applied control torque history. Along with the two required attitude changes, the initial large disturbing control torques were applied and the response was then reduced to nearly zero.

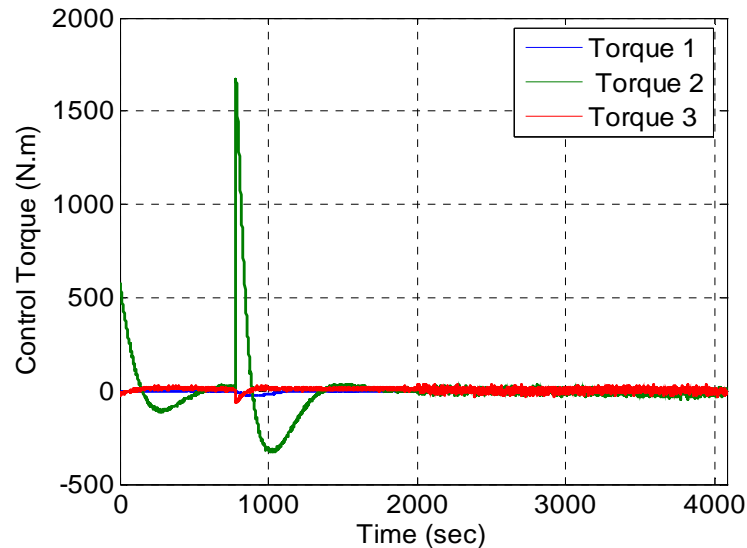


Figure 7.23. Control Torque History.

7.6. CONCLUSION

This study designed a nonlinear SDRE control technique and an LQT control technique for translational maneuvering. The adopted SDRE control technique was designed for nonlinear relative motion dynamics, including Earth oblateness and aerodynamic drag perturbations. Through the SDC parameterization, a linear-like closed-form structure was achieved for the nonlinear system control problem. For the tracking command, the controller was designed without increasing the state dimension, unlike the SDRE integral servo controller. The tracking results using the SDRE control were successfully and efficiently obtained by adjusting the weight matrices at the steady state interval to avoid saturation. The LQT controller designed using the linearized system shows that the free-final state becomes the fixed final state when the weight matrix for the final state is large. This approach is very effective in meeting the final state required condition. The LQT controller results can be used as a guide in designing the SDRE

controller. However, for more precise control, the SDRE controller is preferable because the controller was designed using the nonlinear system including the relative perturbations.

An LQG-type control technique was designed for determining the rotational maneuvers of the chaser spacecraft. A combination of an LQR controller and EKF estimation using star trackers and three axis gyros formulates the LQG-type control technique. As the weight matrices adjustment was done for SDRE control, it was also done similarly for the LQG-type control to decrease the attitude tracking error to within the desired accuracy. An acceptable tracking error was also maintained even in the presence of disturbance torques by adjusting the weight matrices and by use of accurate state estimation using precision sensors. This LQG-type control is thus robust to external disturbance torques and to moment of inertia uncertainty. The Shuttle crew's manual flight segment was chosen to demonstrate the autonomous control techniques. A six degrees-of freedom simulation demonstrated that the autonomous control techniques can successfully manage proximity operations and meet the conditions for docking. The control techniques can also be applied to other missions requiring autonomous proximity operations composed of many subphases including docking. For the execution of autonomous and precise proximity operations, including successful docking, integration with precise state estimation using accurate sensors is needed.

8. NUMERICAL RESULTS AND ANALYSIS

This chapter shows the numerical results and analysis when applying the integrated GNC system developed in this study to the new proximity operations strategy illustrated in Figure 2.1. The initial chaser (ATV) position is [0.2 -3500 0.1] m with respect to the docking port in the CW frame. The target principal moment of inertia [63] and the chaser moment of matrix [102] are given in Eq. (172), respectively. The chaser is equipped with 28 RCS thrusters for attitude control and rendezvous maneuvering. The initial mass [63] of the chaser in this scenario is assumed as 19,600 kg and is time varying as the propellant is consumed. The propellant mass consumption resulting from the control force/torque applications is assumed to be known. The simulation scenario is conducted autonomously in a predefined step-by-step manner, beginning at S2 which is 3.5 km away from the target docking port and continues until the docking port of the target is impacted. The GNC proximity operations manager provides commanding, data handling, and the management of the sequencing of all mission phases. The docking port location is assumed to have coordinates [-1.02 -20.0 0.0] m in the CW frame. The moments of inertia of both vehicles are assumed as

$$I_t = 10^6 \times \begin{bmatrix} 128 & 0 & 0 \\ 0 & 107 & 0 \\ 0 & 0 & 201 \end{bmatrix} \text{ kg m}^2, \quad I_c = 10^6 \times \begin{bmatrix} 1.091 & -0.027 & -0.008 \\ -0.027 & 8.287 & -0.328 \\ -0.008 & -0.328 & 0.328 \end{bmatrix} \text{ kg m}^2 \quad (172)$$

The initial relative position and velocity of the chaser in the CW frame shown Eq. (63) in units of meters and meter per second are given by

$$\mathbf{X}(t_0) = [-1.020 \quad -3532.0 \quad 0.1 \quad -0.01 \quad 0.4325 \quad 0.01]^T \quad (173)$$

The initial attitude of the chaser is rotated by 1 degree of roll, 5 degree pitch and 1 degree of yaw with respect to the CW frame of the target. Then initial roll, pitch, and yaw angles of the chaser with respect the inertial frame are given as

$\phi = 175.21$, $\theta = -7.02$, and $\psi = 56.89$ degrees in a body 3-2-1 sequence. The corresponding chaser quaternion is given by

$$\mathbf{q}_c(t_0) = [0.4628 \quad 0.3614 \quad 0.7716 \quad 0.2444]^T \quad (174)$$

The simulation is performed for 91 minutes at a 0.01 second step size. The spectral densities of the process noise components added to the right-hand side of Eq. (13) to adopt as the truth model are each given by $10^{-7} \text{ m}/(\text{s}\sqrt{\text{s}})$.

All of the results were compiled through simulation of the integrated GNC system and are plotted together. Figure 8.1(a) shows the overall approach trajectory from S2 to the target docking port, successfully tracking the desired nominal path of the V-bar hops (i.e., the series of three V-bar hops). In general, a distance between one and three kilometers is considered close-range rendezvous, which this study also considered. The chaser closing transfer phase was modified to three V-bar hops so that the RELAVIS scanning system would meet the FOV constraint. There are ± 5 and ± 10 degrees of approach corridors shown in Figure 8.1(b). It is very important to ensure that the approaching vehicle enter the approach corridor and pass through it without crossing its boundaries for proper alignment to the straight line final approach.

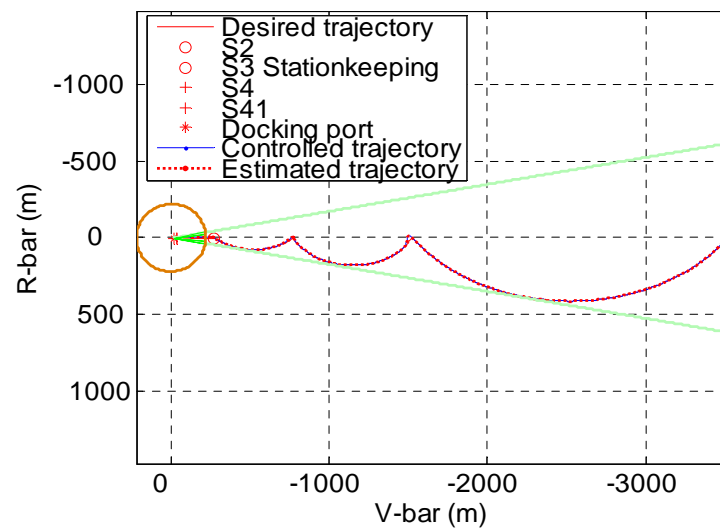


Figure 8.1 (a). Approach Trajectories.

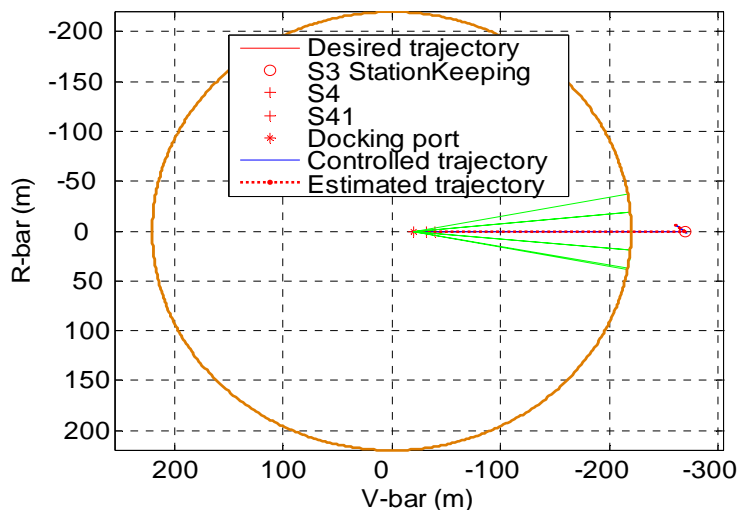


Figure 8.1. (Continued) (b). Approach Trajectories.

The approach maneuvers in Figure 8.1(b) show that it safely entered the ± 5 degrees approach corridor after performing the stationkeeping at S3. The final straight line approach was then simulated with the navigation system switching from the RELAVIS scanning system to the VISNAV system at S4 to take advantage of more accurate navigation and attitude estimation. The entire proximity operation in three dimensional space is shown in Figure 8.2. Figure 8.3 shows the relative position history.

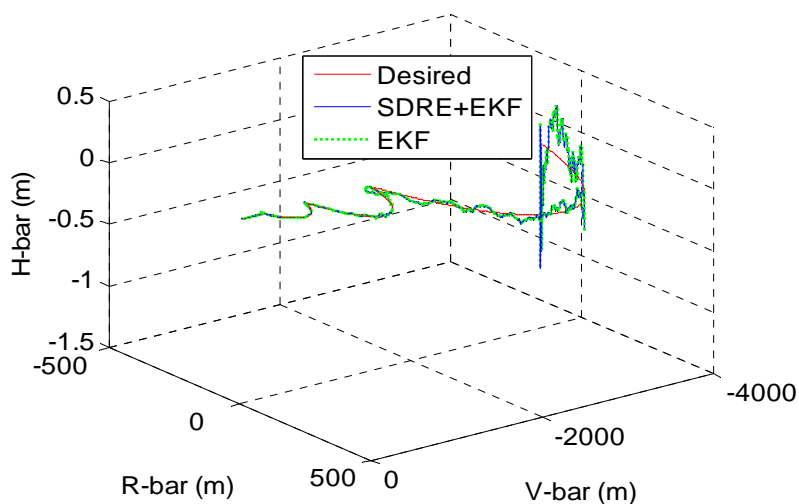


Figure 8.2. Proximity Operations in 3-D Space.

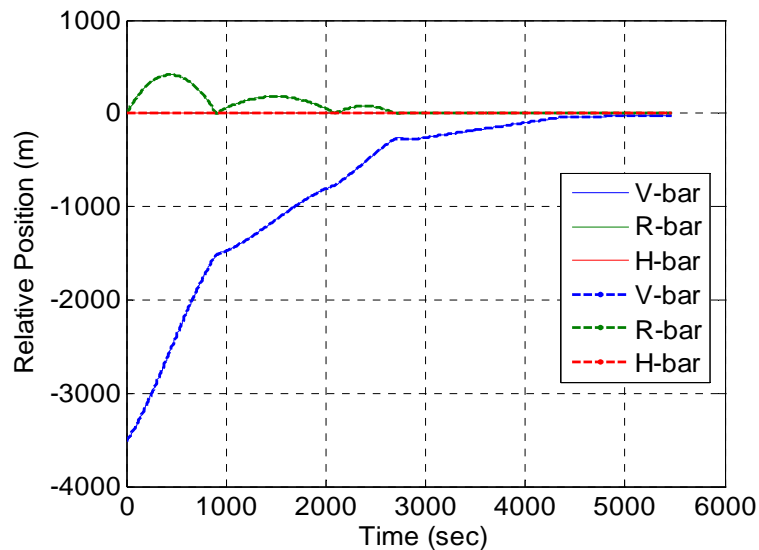


Figure 8.3. Relative Position History.

It is important to note that the relative position tracking error and approach velocity histories, shown in Figures 8.4 and 8.5, are used to ensure that the docking conditions are met.

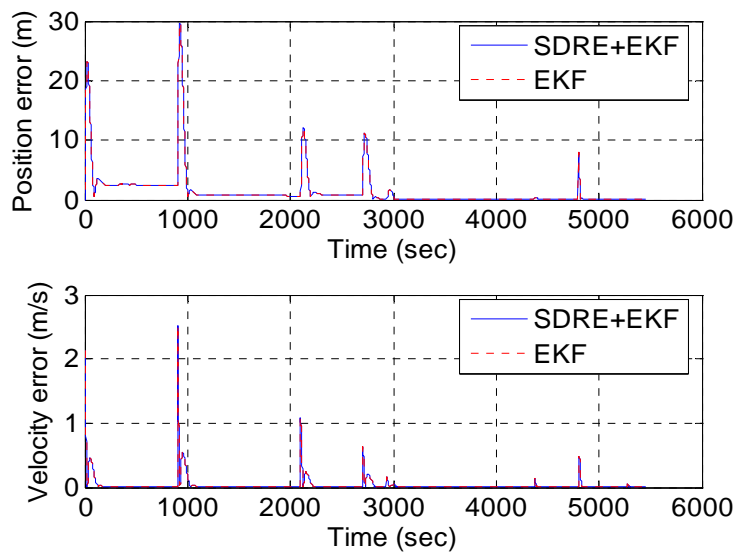


Figure 8.4. Tracking Error History.

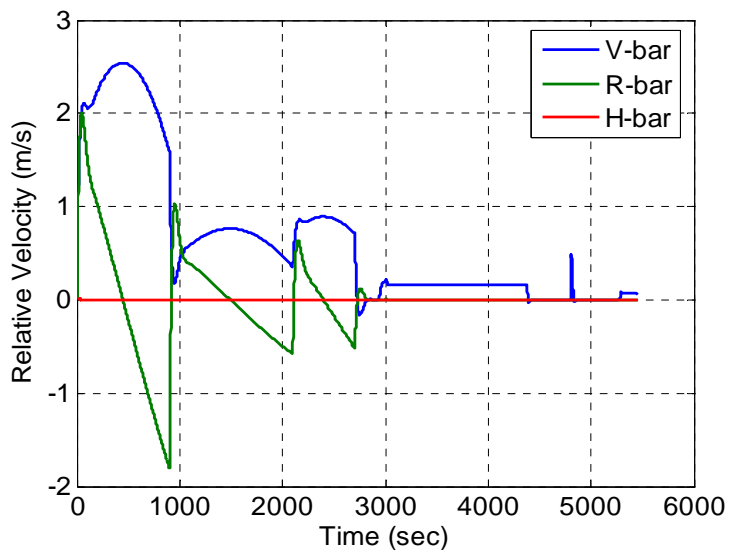


Figure 8.5. Approach Velocity History.

Table 8.1 shows the final conditions to be reached at docking for the chaser. After the chaser vehicle executed the last stationkeeping phase at S4, its position tracking error, which was less than 0.07 m, was maintained to the docking port and satisfied the lateral misalignment condition (less than 0.1 m). The relative velocity history in each direction, shown in Figure 8.5, was less than 0.07 m/s and satisfied the longitudinal closing and lateral velocity conditions.

Table 8.1. Conditions for Entering Docking Phase (3σ) [38].

Translational Conditions		Rotational Conditions	
Relative longitudinal closing velocity	0.05~0.10 m/s	Misalignment angles	< 5 deg
Relative lateral velocity	< 0.02 m/s	Angular rates (pitch)	< 0.40 deg/s
Lateral misalignment	< 0.1 m	Angular rates (roll)	< 0.15 deg/s

A nominal docking orientation with the target along the positive V-bar direction corresponds to an azimuth angle of 90 degrees. Because the docking port geometry is not exactly aligned with the target center of mass, the docking port is not precisely located along the V-bar direction. The actual azimuth angle used is 93 degrees. Figure 8.6 shows that the azimuth angle variation is less than 10 degrees and the elevation angle variation is almost zero since the approach maneuvers are all planar motions.

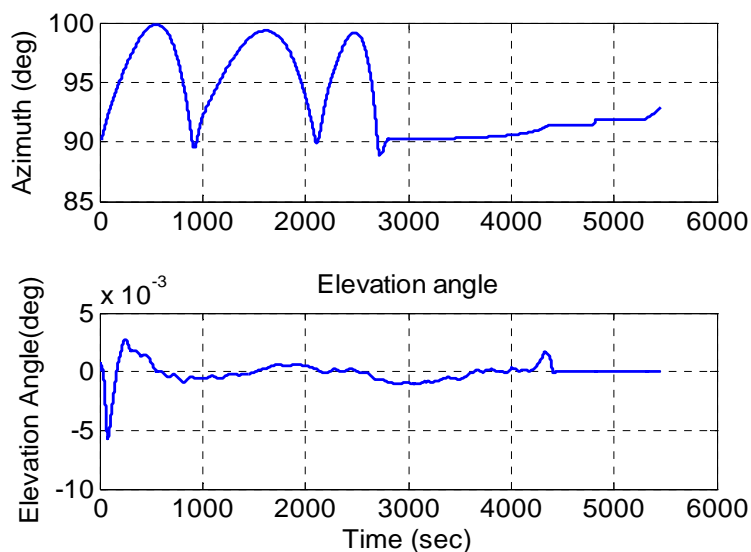


Figure 8.6. Nominal Bearing History.

Whenever the GNC system reinitialized at each assigned point to begin the subsequent phase, the control forces exhibited large impulsive reactions as shown in Figure 8.7. The weight matrices were adjusted at steady state from the initially chosen weight matrices to reduce the tracking error by generating additional control forces while avoiding thruster saturation. It is critical for the SDRE controller to command realizable control forces to the actuators (RCS thrusters) without exceeding the maximum available thrust. The commanded control forces, shown in Figures 8.7, do not exceed the maximum limit.

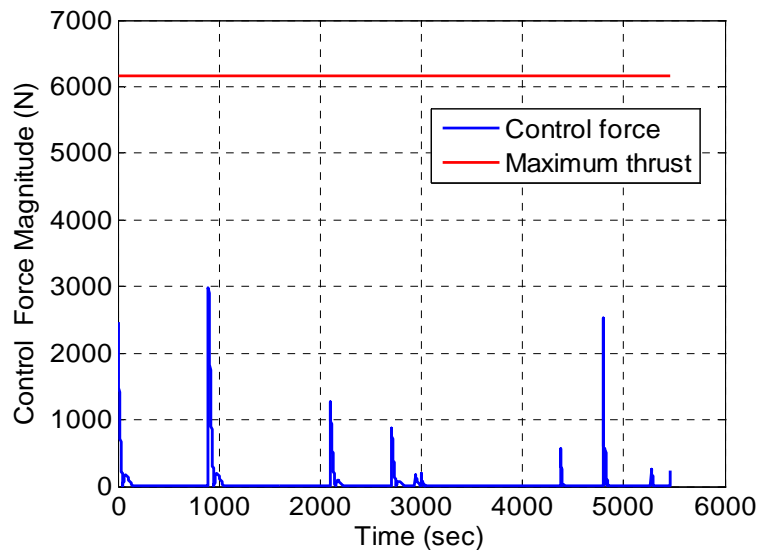


Figure 8.7. Control Force History.

Figures 8.8 and 8.9 show the relative position and velocity errors, and the respective 3σ bounds derived from the EKF covariance matrix. The relative position errors were maintained to less than 0.05 m in 30 minutes. The relative velocity errors were maintained to less than 2×10^{-4} m/s in 15 minutes.

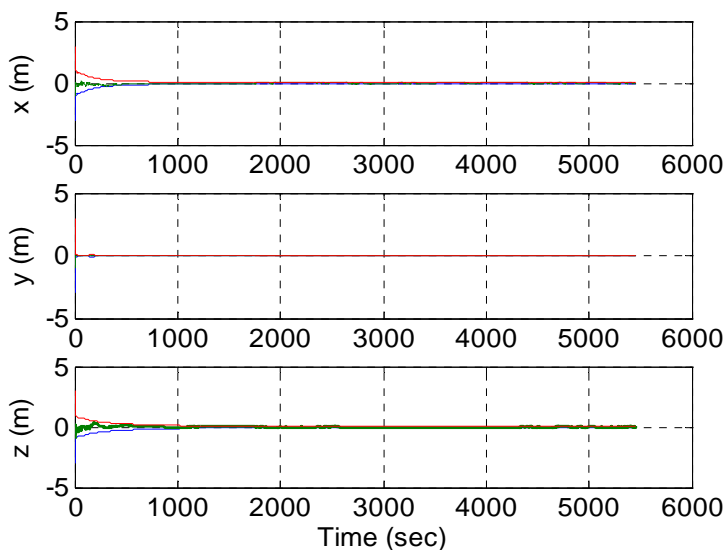


Figure 8.8. Position Errors and 3σ Bounds.

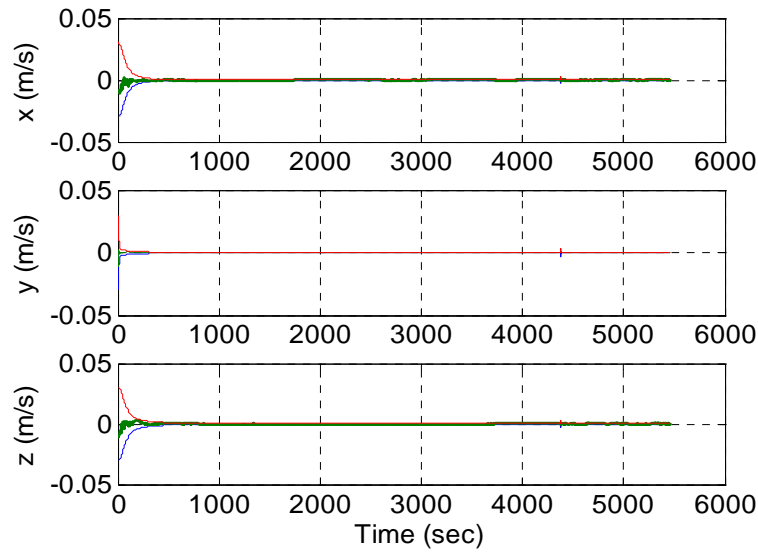


Figure 8.9. Velocity Errors and 3σ Bounds.

As the control forces and torques were applied, propellant mass was consumed, varying the mass and moment of inertia of the chaser. This study assumed that the locations of all RCS thrusters are known, and that the propellant mass consumption resulting from the control torques can be computed. The total consumed mass is the sum of the mass consumed by the application of the control forces and the control torques. The robustness of the attitude controller was evaluated considering the uncertainties of the moment of inertia. The uncertainty was modeled by adding 30 percent of the moment of inertia to the initial value [103]. Moreover, external disturbances, which were not modeled in the controller, were added to the Euler rotational equation in Eq. (24). All of the following results were obtained using the uncertain moment of inertia. Figure 8.10 shows that the chaser could align its attitude with respect to the target body-frame in 400 seconds and maintain the aligned attitude to the docking port. Figure 8.11 shows the Euler angle histories of the target and chaser, including an acceptable attitude tracking result similar to Figure 8.10. The target is on a near-circular, 350×450 km altitude orbit that is Earth pointing, so that the target angular rate can be expressed as $\boldsymbol{\omega}_t = [0 \quad n \quad 0]^T$ in the adopted body-frame where n is the mean motion of the target. From the initial conditions given in Eq. (86), the chaser can successfully perform axis

alignment with respect to the target. As the weight matrices were readjusted at steady state by the SDRE controller, they were also adjusted in the rotational controller to reduce the attitude tracking error.

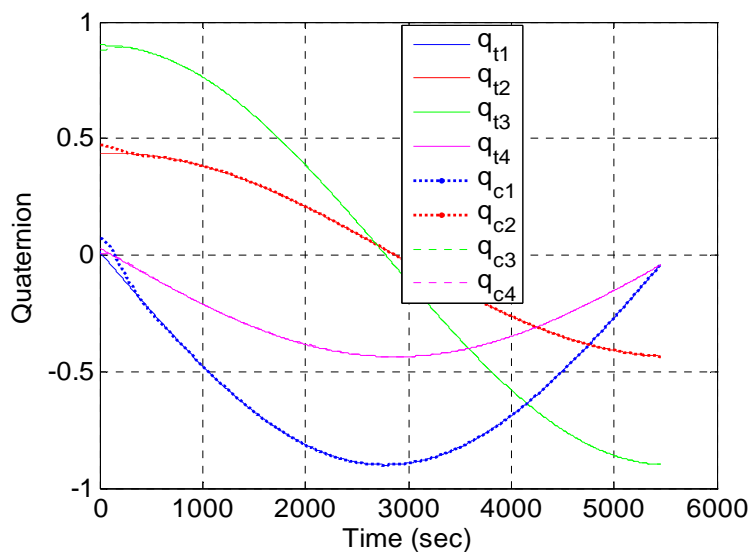


Figure 8.10. Target and Chaser Quaternion Histories.

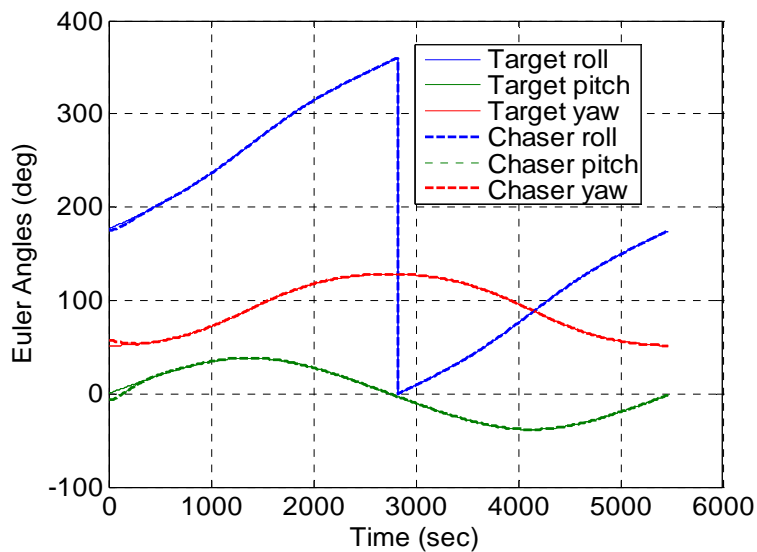


Figure 8.11. Euler Angler Histories.

Figure 8.12 shows the Euler angle error history between the target and the chaser. After the readjustment of the weight matrices, the chaser achieves attitude errors less than 0.1 degrees at the terminal time. Figure 8.13 shows the target angular rate and that the chaser could successfully track the target's attitude rate for 1000 seconds. The chaser pitch rotation rate approached the mean motion of the target as the attitude alignment was achieved.

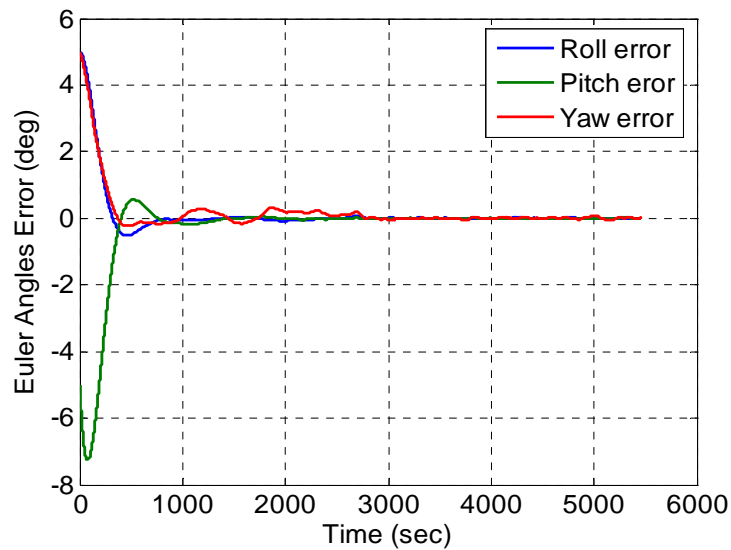


Figure 8.12. Euler Angle Error History.

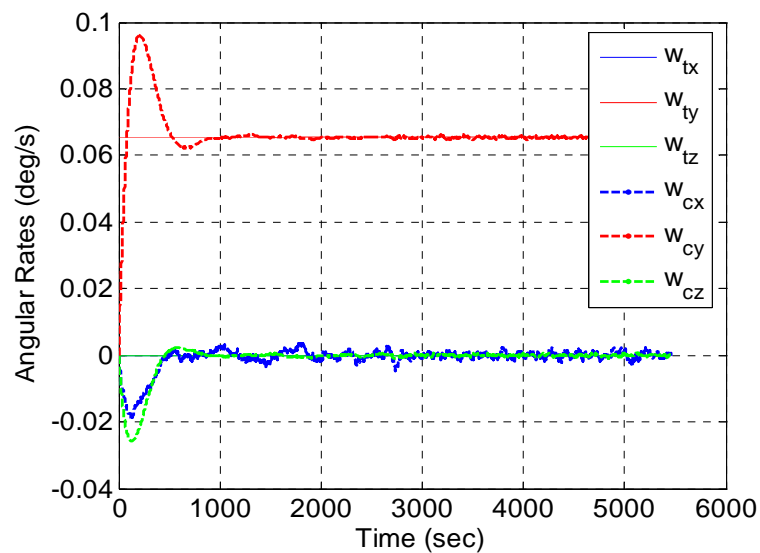


Figure 8.13. Angular Rate Histories.

Figures 8.12 and 8.13 demonstrate that the important rotational conditions listed in Table 3 are met. The small variations in these figures were caused by the external disturbance torques in Eq. (24). The upper graph in Figure 8.14 shows the gravity-gradient torque history of the chaser, and the lower graph in Figure 8.14 shows the external disturbance torques. Both were added to Eq. (24). Figure 8.15 shows the control torque history. The higher control torques were generated using the adjustment of weight matrices to align the chaser axis more accurately with respect to the target axis.

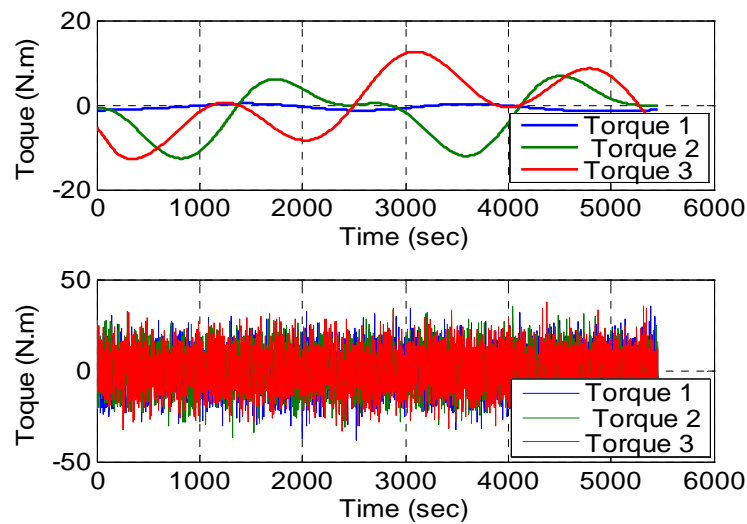


Figure 8.14. Chaser's Gravity-Gradient and External Torque History.

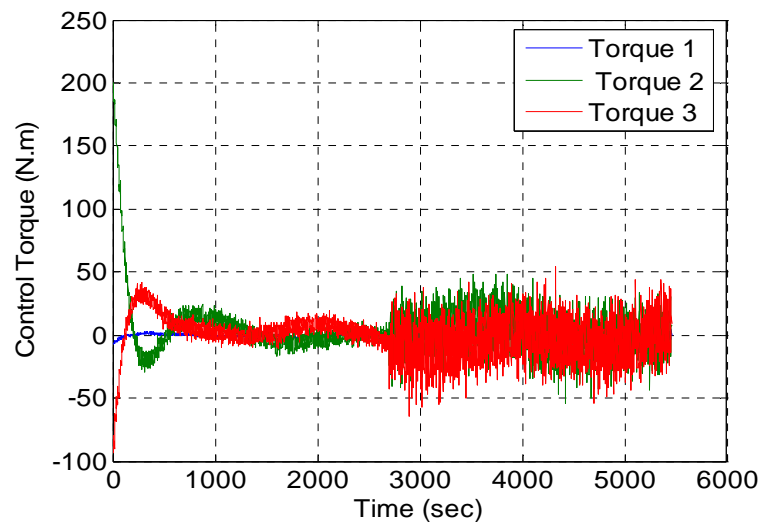


Figure 8.15. Control Torque History.

Figure 8.16 shows the propellant mass consumed by the applied control forces and control torques. Figure 8.17 shows the absolute attitude estimation and respective 3σ bounds by the RELAVIS scanning system from S2 and S4. The navigation system change from the star tracker and gyro-based attitude estimation to the VISNAV system occurs at S4. The VISNAV system provided the relative attitude between the target and the chaser. The relative attitude estimation by the VISNAV was converted to the absolute chaser attitude estimation using Eq. (117). The larger 3σ bounds were computed by the VISNAV error covariance for the relative attitude estimation. The overall attitude errors are within 0.01 degrees. The VISNAV system is more effective in providing accurate navigation and attitude estimation in the final approach phase because the VISNAV measurements improve as the vehicles get closer.

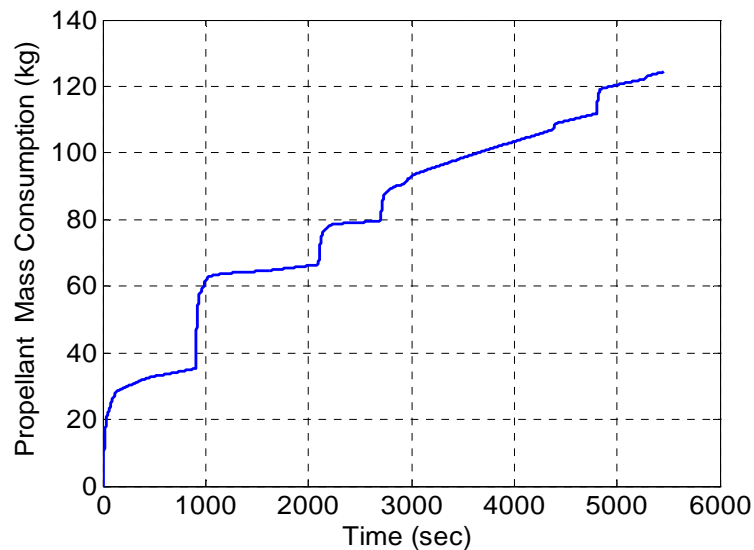


Figure 8.16. Propellant Mass Consumption.

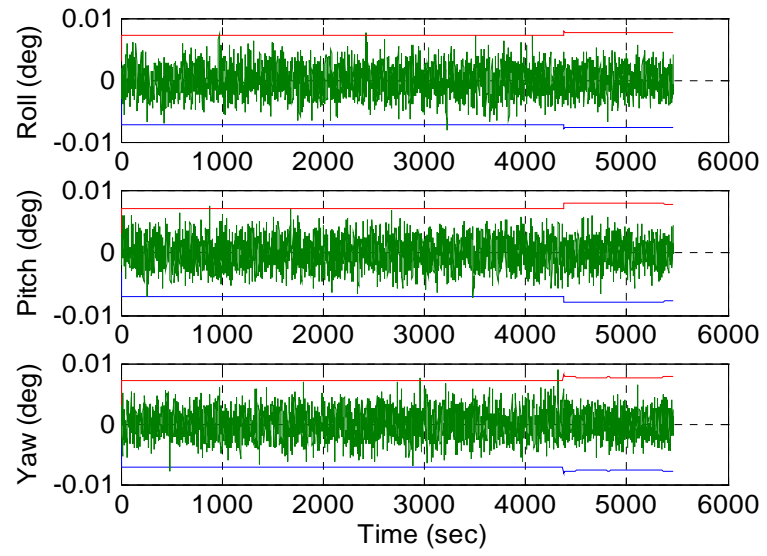


Figure 8.17. Attitude Errors and 3σ Bounds.

9. CONCLUSION

This study proposes a newly developed integrated GNC system for autonomous proximity operations and docking. The GNC system can cover close-range rendezvous as well as proximity operations. Because the RGPS in the Navigation function for closing transfers is replaced by the RELAVIS system, the GNC system can be extended to deep space where GPS system is not available, such as with lunar or Mars missions. The GNC system integrating the Guidance, Navigation and Control functions is summarized using a block diagram of a typical closed-loop controller for each of the six degrees of freedom. Two independent LQG-type controllers for the translational and rotational maneuvers were designed to optimally track the reference trajectories and orientate the spacecraft. The GNC system performs each phase autonomously in a predefined step-by-step manner. The GNC proximity operations manager covers functions common to guidance, navigation and control, and provides commanding, data handling, and managing the sequence of the overall mission phases.

9.1. GUIDANCE FUNCTION

The Guidance function provides the reference trajectories to track during the translational motion and the reference attitude to orientate to in the rotational motion. For the application of the RELAVIS scanning system, the closing transfer in the original ATV V-bar approach strategy was modified into three “V-bar hops” to meet the FOV constraint in the RELAVIS scanning system using the CW terminal guidance law. For the preparation of the next phase, two series of stationkeeping were executed using the exponential braking guidance law to nullify the approach velocity. The straight line LOS final V-bar approach is effective in providing a constant slow approach velocity leading to soft docking. The target quaternion, angular velocity and angular acceleration from onboard navigation are used as the reference states for the attitude alignment.

9.2. NAVIGATION FUNCTION

The Navigation function is in charge of estimating the relative position, velocity, absolute and relative attitude. All of the estimation filters were designed using the EKF. The

RELAVIS navigation system provides the precise relative position and velocity using range and bearing measurements for the closing transfer and for entering the approach corridor. The star trackers generating quaternions and rate-integrating three axis gyros are used to estimate the chaser absolute attitude along with the RELAVIS scanning system in the same phases. The sensor mode switch is made to provide more effective navigation in the approach corridor. The two sets of navigation systems for the translational and rotational maneuvers are replaced by the VISNAV system. As the two vehicles get closer, the VISNAV system can be effective in providing a more accurate navigation solution in the final approach phase to the docking port. The VISNAV system provides the relative position, velocity and attitude estimation meeting the final condition for docking.

9.3. CONTROL FUNCTION

This study designed a nonlinear SDRE control technique and an LQT control technique for translational maneuvering. The SDRE control technique was designed for nonlinear relative motion dynamics, including effects from Earth oblateness and aerodynamic drag perturbations. Through the SDC parameterization, a linear-like closed-form structure was achieved for the nonlinear system control problem. For determining the tracking command, the controller was designed without increasing the state dimension, unlike the general SDRE integral servo controller. The tracking results using the SDRE controller were successfully and efficiently achieved by adjusting the weight matrices at the steady state condition to avoid saturation. The LQT controller designed for the linearized system shows the free-final state becomes the fixed final state when the large weight matrix for the final state is used. This result is very useful in meeting the final state condition required. The LQT control results can be used as a guide for designing the SDRE controller. However, for more precise control with respect to the realistic dynamic model, the SDRE control is preferable because the controller was designed using the nonlinear system including the relative perturbations.

The rotational control law formulation using LQR with linearized dynamics was integrated with attitude estimation using star trackers and gyros, and a vision sensor and gyros by the EKF filter for the rotational maneuvers leading to LQG-type control. Like

the integrated translational tracking controller, the weight matrices were also adjusted at steady state for rotational control. Because of the varying total mass due to propellant consumption, the robustness of the LQG-type rotational controller was evaluated considering the uncertainty of the chaser moment of inertia. Moreover, the external disturbance torque and the gravity-gradient torque that were not modeled in the controller were included in Euler's rotational equation of motion. Even under these conditions, the LQG-type rotational controller showed robust attitude tracking results. It was then integrated with the RELAVIS and the VISNAV systems by feeding the estimated states to the controller. The integrated translational tracking controller based on the SDRE control successfully tracked the reference trajectories by readjusting the weight matrices at steady while avoiding the actuator saturation.

A new GNC system integrating the Guidance, Navigation and Control functions uses closed-loop control for each of the six degrees of freedom as the LQG-type controller satisfies the separation theorem. A six degrees-of-freedom simulation demonstrates the capacity of the GNC system to execute several translational maneuvers and axis alignments for proximity operations. The new GNC system successfully satisfies all of conditions for entering the docking phase by executing each phase autonomously.

10. FUTURE WORK

This study considered control force and torque commands requested by the controllers without specifying which thrusters were to be fired. The use of an optimal thruster selection algorithm needs to be developed. This function provides the conversion of the six degrees of freedom force and torque requests generated by the guidance and control functions into a set of thruster impulses to be realized by the propulsion system. The control forces expressed in the spacecraft local orbital frame A can be expressed in the body-fixed frame like control torques using Eq. (17). The required control forces and torques can be delivered to the actuator (RCS thruster) using a mathematical linear optimization problem.

What are the observables, and what are the criteria by which failures can be identified? On the highest level it may be possible to detect the deviation of the actual state of the vehicle from the predefined states in terms of relative position, velocity and attitude. If the fault happens in the system, the system should be equipped with a recovery system through the FDIR procedure. To detect a failure condition at a high level, the violation of safety margins around the nominal values of position, velocity, attitude and angular rates in the GNC functions can be used. FDIR needs to cover the failures of the thrusters and failures of the sensors and of the GNC software. A well-designed onboard FDIR system can assure protecting against failures to very large extent. The implementation of the FDIR system in each function can be desirable to cope with the system failure, and detect and recover it.

The numerical results in this study rely only on the simulated measurements. For the validation of the navigation system, research using test-bed experiments with the RELAVIS scanning system and VISNAV system or real measurements from the star trackers by onboard navigation are recommended. Then, the navigation system should provide valid results through numerical analysis and be compared with the conditions for adequate navigation accuracy. Instead of the selective sensor switching used in this study, the integrated navigation system using other navigation systems can be considered to increase reliability and accuracy.

BIBLIOGRAPHY

- [1] J. R. Wertz and R. Bell, "Autonomous Rendezvous and Docking Technologies — Status and Prospects," Space Systems Technology and Operations Conference, Orlando Florida, April 21-25, 2003.
- [2] C. D'Souza, F. C. Hanak, and P. Spehar, "Orion Rendezvous, Proximity Operations, and Docking Design and Analysis," AIAA Guidance, Navigation and Control Conference and Exhibit, Hilton Head, South Carolina, 20-23 Aug. 2007, AIAA 2007-6683.
- [3] M. F. Machula and G. S. Sandhoo, "Rendezvous and Docking for Space Exploration," 1st Space Exploration Conference: Continuing the Voyage of Discovery, Orlando, Florida, Jan. 30-Feb. 1, 2005, AIAA 2005-2716.
- [4] J. L. Goodman, "History of Space Shuttle Rendezvous and Proximity Operations," *Journal of Spacecraft Rockets*, Vol. 43, No. 5, Sep.-Oct. 2006, pp. 944-959.
- [5] É. Martin, É. Dupuis, J. C. Piedboeuf, and M. Doyon, "The TECSAS Mission from a CANADIAN Perspective," ISAIRAS 2005 Conference, Munich, Germany, Sep. 5-8, 2005. ESA SP-603.
- [6] J. L. Goodman, and J.P. Brazzel, "Challenges of Orion Rendezvous Development," AIAA Guidance, Navigation and Control Conference and Exhibit, Hilton Head, South Carolina, Aug. 20-23, 2007, AIAA 2007-6682.
- [7] C. D'Souza¹, F. C. Hanak¹, and P. Spehar, "Orion Rendezvous, Proximity Operations, and Docking Design and Analysis," AIAA Guidance, Navigation and Control Conference and Exhibit, Hilton Head, South Carolina, Aug. 20-23, 2007, AIAA 2007-6683.
- [8] Y. Ohkami and I. Kawano, "Autonomous Rendezvous and Docking by Engineering Test Satellite VII: A Challenge of Japan in Guidance, Navigation and Control," 51st International Astronautical Congress. Rio de Janeiro, Brazil, Oct. 2-6, 2000.
- [9] R. Quitero, R. C. Montgomery, and P. Tchoryk, "Autonomous Rendezvous and Docking Scenarios for The Development of Guidelines and Standards," AIAA Space Programs and Technologies Conference and Exhibit, Huntsville AL, Sep. 21-23, 1993, AIAA 93-4753.
- [10] W. S. Cook and S. D. Lindell, "Autonomous Rendezvous and Docking (AR&D) for Future Spacecraft Missions," AIAA Space Technology Conference & Exposition, Albuquerque, NM, Sep. 28-30, 1999, A99-42136.

- [11] T. Carrico, T. Langster, J. Carrico, D. Vallado, M. Loucks, and S. Alfano, "Proximity Operations for Space Situational Awareness: Spacecraft Closed-Loop Maneuvering Using Numerical Simulations and Fuzzy Logic," Advanced Maui Optical and Space Surveillance Technologies Conference, Sep. 2006.
- [12] M. E. Polites, "Technology of Automated Rendezvous and Capture in Space," *Journal of Spacecraft and Rockets*, Vol. 36, No. 2, Mar.–Apr., 1999.
- [13] Charles Stark Draper Laboratory, "Apollo Guidance, Navigation and Control Final Report," Volume V, The Software Effort, July 1971.
- [14] D. Zimpfer, P. Kachmar and S. Tuohy, "Autonomous Rendezvous, Capture and In-Space Assembly: Past, Present and Future," 1st Space Exploration Conference: Continuing the Voyage of Discovery, Orlando, Florida, Jan. 30- Feb. 1, 2005.
- [15] http://en.wikipedia.org/wiki/File:Gemini_6_7.jpg, Organizing Daero Lee's Thesis, June 2009.
- [16] http://upload.wikimedia.org/wikipedia/commons/2/2f/Gemini_and_Agena_D.jpg, Organizing Daero Lee's Thesis, June 2009.
- [17] http://images.google.com/imgres?imgurl=http://www.aerospacenews.com/space_pictures/albums/userpics/10001/normal_apollo.11.lunar.module.space.jpg, Organizing Daero Lee's Thesis, June 2009.
- [18] http://upload.wikimedia.org/wikipedia/commons/c/c0/Apollo_CSM_lunar_orbit.jpg, Organizing Daero Lee's Thesis, June 2009.
- [19] http://images.google.com/imgres?imgurl=http://upload.wikimedia.org/wikipedia/commons/thumb/b/b9/Atlantis_Docked_to_Mir.jpg, Organizing Daero Lee's Thesis, June 2009.
- [20] http://www.popsci.com/files/imagecache/article_image_large/files/articles/DART.jpg, Organizing Daero Lee's Thesis, June 2009.
- [21] <http://www.unsayablejazer.com/blog/wp-content/uploads/2007/07/oe.jpg>, Organizing Daero Lee's Thesis, June 2009.
- [22] <http://images.google.com/imgres?imgurl=http://www.spacetoday.org/images/Sats/XSS11>, Organizing Daero Lee's Thesis, June 2009.
- [23] http://www.satnews.com/cgi-bin/display_image.cgi?1583852487, Organizing Daero Lee's Thesis, June 2009.
- [24] http://www.skycontrol.net/UserFiles/Image/Aerospace_img/200711/200711cnes-atv-docking.jpg, Daero Lee's Thesis, June 2009.

- [25] T. Rumford, "Demonstration of Autonomous Rendezvous Technology (DART) Project Summary," Core Technologies for Space Systems Conference, Nov., 2002.
- [26] NASA Report: "Overview of the DART Mishap Investigation Results," For Public Release, May 15, 2006.
- [27] NASA Engineering and Safety Center Report: "Demonstration of Autonomous Rendezvous Technology Mishap Review Board," Dec. 2006.
- [28] G. Gottselig, "Orbital Express Advanced Technology Demonstration," 2002 Core Technologies for Space Systems Conference, Nov. 2002.
- [29] D. A. Barnhart, R. C. Hunter, A. R. Weston, V. J. Chioma, M. Steiner, W. Larsen, AIAA Defense and Civil Space Programs Conference and Exhibit, Huntsville, AL, Oct. 28-30, 1998, Collection of Technical Papers (A98-45901 12-66).
- [30] F. J. Pelletier and D.F. Golla, "Lidar-based Rendezvous Navigation for MSR," AIAA/AAS Astrodynamics Specialist Conference and Exhibit, Providence, Rhode Island, 16-19, Aug., 2004.
- [31] F. J. Pelletier and D.F. Golla, "Lidar-Based Autonomous Rendezvous in Mars Orbit," *Proceedings of the 7th International Symposium on Artificial Intelligence, Robotics and Automation in Space*, NARA, Japan May 19-23, 2003
- [32] E. Martin, D. Maharaj, R. Richards, J. Tripp, J. Bolger and D. King, "RELAVIS: The Development of a 4D Laser Vision System for Spacecraft Rendezvous and Docking Operations," *Proceedings of SPIE Spaceborne Sensors*, Orlando, FL, USA, April 13, 2004, Vol. 5418, pp. 69-80.
- [33] S. Parkes, M. Dunstan, D. Matthews, I. Martin, I, and V. Silva, "LIDAR-Based GNC for Planetary Landing: Simulation with PANGU," *Proceedings of DASIA 2003* (ESA SP-532), Prague, Czech Republic, 2-6 June, 2003.
- [34] A. E. Johnson, A. R. Klumpp, J. B. Collier, A. A. Wolf, "Lidar-Based Hazard Avoidance for Safe Landing on Mars," *Journal of Guidance, Control, and Dynamics*, Vol. 25, No. 6, Nov.–Dec. 2002. pp.1091-1099.
- [35] R. C. Fenton, A Lidar-based Pose Estimation Algorithm for Determining Relative Motion of a Spacecraft for Autonomous Rendezvous and Dock, *Master of Science*, Utah State University, Logan, Utah, 2008.
- [36] J.L. Gonnaud and V. Pascal, "ATV Guidance, Navigation and Control for Rendezvous with ISS," *Proceedings of the 4th ESA International Conference on Spacecraft Guidance, Navigation and Control Systems*, ESTEC, Noordwijk, the Netherlands, Oct. 18-21, 1999, p. 501.

- [37] J. Farbrega, M. Frezet and J. Gonnard, "ATV GNC During Rendezvous," *Proceedings 3rd International Conference on Spacecraft Guidance, Navigation and Control Systems*, ESTEC, Noordwijk, The Netherlands, Nov. 18-21, 1996.
- [38] D. Pinard , S. Reynaud , P. Delpy and S.E. Strandmoe, "Accurate and Autonomous Navigation for the ATV," *Aerospace Science and Technology*, pp. 490–498, Nov. 26-29, 2007.
- [39] J. Gonnaud, J. Sommer, and M. Tsang, "APRK GNC Design and Performances Evaluation for ATV Rendezvous," *Proceedings of the 3rd International Conference on Spacecraft Guidance, Navigation and Control Systems*, ESTEC, Noordwijk, The Netherlands, Nov. 26-29, 1996.
- [40] V.Godet, JL. Gonnaud, and J.M. Pairet, "GNC Baseline for ATV Rendezvous with ISS ," AIAA International Space Station Conference, Houston, Texas, Apr. 2, 1999.
- [41] J. Gonnaud, M. Tsang, and J. Sommer, "APRK GNC Design and Performances Evaluation for ATV Rendezvous," 3rd ESA International Conference on Spacecraft Guidance, Navigation and Control Systems, Nov. 1996.
- [42] J. Gonnaud and V. Pascal, "ATV Guidance Navigation and Control," *Proceedings 4th ESA International Conference on Spacecraft Guidance, Navigation and Control Systems*, ESTEC, Noordwijk, The Netherlands, 18-21, October 1999.
- [43] D. Cornier, D. Paris, B. Dore, F. Thellier, and J.L. Francart, "The Automated Transfer Vehicle (ATV) Mission to the International Space Station, Rendezvous and Docking Aspects," International Space Station Conference, Houston, Texas, April 2nd, 1999.
- [44] F. Chabert and S.E. Strandmoe, "Automated Transfer Vehicle (ATV) GNC Overview," *IAC-02-A.P.03*, IAF, Houston 2002.
- [45] P. Simon, S. Dussy, and P. Delaux, "Navigation Sensors Architecture for the Automated Transfer Vehicle", 15th IFAC Symposium on Automatic Control in Aerospace, Bologna, 2–7 September 2001.
- [46] J. Gonnaud, L. Lagarde, S.E. Strandmoe, and A. Ballereau, "Relative GPS Navigation Implementation for the ATV Rendezvous," 5th ESA International Conference on Spacecraft G,N & C Systems, Frascati, 2002.
- [47] D.E. Gaylor and E.G., Lightsey, "GPS/INS Kalman Filter Design for Spacecraft Operating in The Proximity of The International Space Station," AIAA Guidance, Navigation, and Control Conference and Exhibit, Austin, Texas, 11-14, Aug. 2003.

- [48] P. Singla and K. Subbarao, "Adaptive Output Feedback Control for Spacecraft Rendezvous and Docking Under Measurement Uncertainty," *Journal of Guidance, Control, and Dynamics*, Vol. 29, No. 4, Jul-Aug 2006.
- [49] S.R. Walker, "Space Shuttle Rbar Pitch Maneuver for Thermal Protection System Inspection," AIAA Guidance, Navigation, and Control Conference and Exhibit, San Francisco, California, 15–18, Aug. 2005.
- [50] J. P. Brazzel, "RPOP Enhancements to Support the Space Shuttle R-Bar Pitch Maneuver for Tile Inspection," AIAA Guidance, Navigation, and Control Conference and Exhibit, San Francisco, California, 15-18 Aug. 2005, AIAA 2005-5984.
- [51] John L. Junkins, Declan C. Hughes, Karim P. Wazni, and Vatee Pariyapong, "Vision-Based Navigation for Rendezvous, Docking and Proximity Operation," AAS 99-021, May 24-28, 1999, pp. 203-214.
- [52] Kiran K. Gunnam, Declan C. Hughes, John L. Junkins, and Nasser Kehtarnavaz, "A Vision-Based DSP Embedded Navigation Sensor," *IEEE Sensors Journal*, Vol. 2, No. 5, Oct. 2002, pp. 428-442.
- [53] Alonso, R., Crassidis, J. L., and Junkins, J. L., "Vision-Based Navigation for Formation Flying of Spacecraft," AIAA Guidance, Navigation, and Control Conference, Denver, CO, Aug. 2000, AIAA 2000-4439.
- [54] K. Subbarao and J. McDonald, "Multi-Sensor Fusion Based Relative Navigation for Synchronization and Capture of Free Floating Spacecraft," AIAA Guidance, Navigation, and Control Conference and Exhibit, San Francisco, California, 15-18 August 2005, AIAA 2005-5858.
- [55] J. M. Kelsey, J. Byrne, M. Cosgrove, S. Seereeram, and R. K. Mehra, "Vision-Based Relative Pose Estimation for Autonomous Rendezvous And Docking," Aerospace Conference, 2006 IEEE, Jun. 24, 2006.
- [56] M. Romano, "Laboratory Experimentation of Autonomous Spacecraft Proximity-Navigation using Vision and Inertia Sensors," AIAA Guidance, Navigation, and Control Conference and Exhibit, San Francisco, California, 15-18 Aug. 2005, AIAA 2005-6461.
- [57] D. Lee and H. Pernicka, "Vision-Based Relative State Estimation Using the Unscented Kalman Filter," paper AAS 09-166, AIAA/AAS Spaceflight Mechanics Meeting, Savannah, Georgia, 2009.
- [58] Pearson, D. J., Shuttle Rendezvous and Proximity Operations," *Proceedings of the CNES International Symposium on Space Dynamics*, Centre National d' Etudes Spatiales, Paris, 1989, pp. 833-851.

- [59] O. W. Olszewski, "Automated Terminal Guidance for a Space Shuttle Rendezvous to Station Freedom," AIAA Guidance, Navigation and Control Conference, Portland, OR, Aug 20-22, 1990, AIAA-90-3356-CP.
- [60] J.A. Prussing and B. A. Conway, *Orbital Mechanics*, Oxford University Press, Inc., Avenue, New York, New York, 1993, Chapter 8.
- [61] W.H Clohessy and R. S Wiltshire, "Terminal Guidance System for Satellite Rendezvous," *Journal of Guidance, Control, and Dynamics*, Sept. 1960, pp. 653-658.
- [62] M. A. Turbel, J. H. McDuffie, B. K. Dekock, and K. Betts, "SPARTAN: A High-Fidelity Simulation for Automated Rendezvous and Docking Applications," AIAA Modeling and Simulation Technologies Conference and Exhibit, Hilton Head, South Carolina, Aug. 20-23, 2007, AIAA-2007-6806.
- [63] Fehse, *Automated Rendezvous and Docking of Spacecraft*, Cambridge University Press, 2003.
- [64] R.G. Brown and P.Y. Hwang, *Introduction to Random Signals and Applied Kalman Filtering with Matlab Exercises and Solutions*, Wiley, 3rd Edition, 1997, pp. 202-204.
- [65] B. Schutz, G. H. Born, and B. Tapley, *Statistical Orbit Determination*, Elsevier Academic Press, Burlington, MA, 2004.
- [66] Son-Goo Kim, John L. Crassidis, Yang Cheng and Adam M. Fosbury, "Kalman Filtering for Relative Spacecraft Attitude and Position Estimation," *Journal of Guidance, Control, and Dynamics*, Vol. 30, No. 1, 2007, pp. 133-143.
- [67] J.L. Crassidis and J.L. Junkins, *Optimal Estimation of Dynamic Systems*, Chapman & Hall/CRC, 2004.
- [68] J. R. Cloutier, "State-Dependent Riccati Equation Techniques: An Overview," *Proceedings of the American Control Conference*, Albuquerque, New Mexico, June 1997.
- [69] D. T. Stansbery and J. R. Cloutier, "Position and Attitude Control of a Spacecraft Using the State Dependent Riccati Equation Technique," *Proceedings of the American Control Conference*, Chicago, Illinois, June 2000.
- [70] T. Cimen, "State-Dependent Riccati Equation (SDRE) Control: A Survey," *Proceedings of the 17th World Congress*, The International Federation of Automatic Control, Seoul, Korea, July 6-11, 2008.

- [71] F. L. Lewis and V. L. Syrmos, *Optimal Control*, John Willey & Sons, Inc., 2nd ed., 2005.
- [72] D. S. Naidu, *Optimal Control Systems*, CRC Press, Inc., Boca Raton, FL, 2003.
- [73] A. Green and J. Z. S, "Methods of Trajectory Tracking for Flexible Link Manipulators," AIAA Guidance, Navigation, and Control Conference Exhibit, Monterey, California, Aug. 5-8, 2002, AIAA 2002-4565.
- [74] R. Bach and R. Paielli, "Linearization of Attitude-Control Error Dynamics," *IEEE Transactions on Automatic Control*, Vol. 38, No. 10, Oct. 1993.
- [75] R. A. Paielli and R. E. Bach, "Attitude Control with Realization of Linear Error Dynamics," *Journal of Guidance, Control, and Dynamics*, Vol. 16, No. 1, 1993.
- [76] H. Schaubl, M. R. Akella, and J. L. Junkins, "Adaptive Control of Nonlinear Attitude Motions Realizing Linear Closed-Loop Dynamics," *Proceedings of the American Control Conference*, San Diego, California, June 1999.
- [77] M. Sznaier and R. Suarez, "Suboptimal Control of Constrained Nonlinear Systems via Receding Horizon State Dependent Riccati Equations," *Proceedings of the 40th IEEE Conference on Decision and Control*, Orlando, Florida, Dec. 2001.
- [78] T. Cimen, "State-Dependent Riccati Equation (SDRE) Control: A Survey," *Proceedings of the 17th World Congress*, The International Federation of Automatic Control, Seoul, Korea, July 6-11, 2008.
- [79] R. A. Florest and E. Barbierit, "Real-Time Infinite Horizon Linear-Quadratic Tracking Controller for Vibration Quenching in Flexible Beams," 2006 IEEE International Conference on Systems, Man, and Cybernetics, Taipei, Taiwan, Oct. 8-11, 2006
- [80] J. Imae, H. Sagami, T. Kobayashi, and G. Zhai, "Nonlinear Control Design Method Based on State-Dependent Riccati Equation (SDRE) via Quasi-Newton Method," 43rd IEEE Conference on Decision and Control, Atlantis, Paradise Island, Bahamas, Dec. 14-17, 2004.
- [81] C. P. Mracek and Ames R. Cloutier, "Control Design for the Nonlinear Benchmark Problem via the State-Dependent Riccati Equation Method," *International Journal of Robust and Nonlinear Control*, Volume 8 Issue 4-5, pp. 401-433, 1998.
- [82] Satellite Toolkit, Analytical Graphics Inc., 220 Valley Creek Blvd., Exton, PA 19341.
- [83] H. Schaub and J.L Junkins, *Analytical Mechanics of Space Systems*, American Institute of Aeronautics and Astronautics, Inc, Reston, Virginia, 2003, Chapter 14.

- [84] D.A. Vallado, *Fundamentals of Astrodynamics and Applications*, 2nd ed., Microcosom Press, 2004, pp. 524-537.
- [85] R.G. Madonna, *Orbital Mechanics*, Krieger Publishing Company, Inc., 1997, pp. 105-107.
- [86] B. Wie, *Space Vehicle Dynamics and Control*, American Institute of Aeronautics and Astronautics, Inc., Reston, Virginia, 1998, pp. 365—369.
- [87] D. Lee and H. Pernicka, “Vision-Based Relative State Estimation Using the Unscented Kalman Filter,” AAS 09-166, AIAA/AAS Spaceflight Mechanics Meeting, Savannah, Georgia, 2009.
- [88] E.J. Lefferts, F.L. Markley, and M. D. Shuster, “Kalman Filtering for Spacecraft Attitude Estimation,” *Journal of Guidance, Control, and Dynamics*, Vol. 5, No. 5, Sept.-Oct. 1982, pp. 417-429.
- [89] Shuster, M. D., “Kalman Filtering of Spacecraft Attitude and the QUEST Model,” *The Journal of the Astronautical Sciences*, Vol. 38, No. 3, July-Sept. 1990, pp. 377–393.
- [90] Malcolm D Shuster, “Survey of Attitude Representations,” *The Journal of the Astronautical Sciences*, Vol. 41, No. 4, 1993, pp. 439-517.
- [91] Matthew C. Van Dyke, Jana L. Schwartz and Christopher D. Hall, “Unscented Kalman Filtering for Spacecraft Attitude State and Parameter Estimation,” AAS/AIAA 16th Annual Space Flight Mechanics Meeting, Jan. 22-26, 2006, pp. 217-228.
- [92] John L. Crassidis, and F. Landis Markley, “Unscented Filtering for Spacecraft Attitude Estimation,” *Journal of Guidance, Control, and Dynamics*, Vol. 26, No. 4, 2003, pp. 536-542.
- [93] Yee-Jin Cheon and Jong-Hwan Kim, “Unscented Filtering in a Unit Quaternion Space for Spacecraft Attitude Estimation,” Industrial Electronics, IEEE International Symposium, 2007, pp. 66-71.
- [94] S.J. Julier and J.K. Uhlmann, “Unscented Filtering and Nonlinear Estimation,” *Proceedings of the IEEE*, Vol. 92, No. 3, March 2004, pp. 401-422.
- [95] Eric A. Wan and Rudolph van der Merwe, “The Unscented Kalman Filter for Nonlinear Estimation,” *Proceedings of Symposium 2000 on Adaptive Systems for Signal Processing, Communication and Control*, Oct. 2000, pp. 153-158.

- [96] S. A. Banani and M. A. Masnadi-Shirazi, "A New Version of Unscented Kalman Filter," *Proceedings of the World Academy of Science, Engineering and Technology*, Vol. 20, April 2007.
- [97] S.J. Julier, J.K. Uhlmann and H.F. Durrant-Whyte, "A New Approach for Filtering Nonlinear Systems," *Proceedings of the American Control Conference*, Vol. 3, June 1995, pp. 1628-1632.
- [98] M. D. Shuster and S. D. Oh, "Three-Axis Attitude Determination from Vector Observations," *Journal of Guidance and Control*, Vol. 4, Jan.-Feb. 1981, pp. 70-77.
- [99] C.F. Van Loan, "Computing Integrals Involving the Matrix Exponential," *IEEE Transactions on Automatic Control*, Vol. AC-23, No. 3, June 1978, pp. 396-404.
- [100] Hanspeter Schaub and John L. Junkins, "Stereographic Orientation Parameters for Attitude Dynamics: A Generalization of the Rodrigues Parameters," *The Journal of the Astronautical Sciences*, Vol. 44, No. 1, January-March 1996, pp. 1-9.
- [101] Daero Lee, J.E Cochran. and J.H. Jo, "Solution to the Variational Equations for Relative Motion of Satellites," *Journal of Guidance, Control, and Dynamics*, Vol. 30, No. 3, May-June 2007, pp. 669-678.
- [102] T. Nagata, V. J. Modi and H. Matsuo, "Dynamics and Control of Flexible Multibody Systems Part II: Simulation Code and Parametric Studies with Nonlinear Control," *Acta Astronautica*, Vol. 49, No. 11, 2001, pp. 595-610.
- [103] M. Xin, S.N. Balakrishnan, and D. T. Stansbery, "Spacecraft Position and Attitude Control with $\theta - D$ Technique," 42nd AIAA Aerospace Sciences Meeting and Exhibit, Reno, Nevada, 5-8 Jan, 2004, AIAA 2004-540.

VITA

Daero Lee was born on a small island, Wando, Korea, on April 11, 1974, as the eldest son of Bok-Nan Lee and Pyung-Sun Lee. He received the Bachelor of Science and Master of Science in Aerospace Engineering from Konkuk University, Seoul, Korea in 1999 and 2001, respectively. While he attended Konkuk University as a master's student, he researched on the precise orbit determination using GPS and Real Time Kinematics (RTK) of GPS. He left to study abroad at Auburn University in 2003 as a Ph.D. student, and received the Master of Aerospace Engineering in May 2006. He transferred to the University of Texas at Austin in August 2006 to pursue a Ph.D. After he spent one year at the University of Texas at Austin, he transferred to the Missouri University of Science and Technology in August 2007, and fulfilled the requirements and earned his Doctor of Philosophy in Aerospace Engineering in August 2009. His research interests cover precision navigation system, optimal control and nonlinear control, autonomous rendezvous and proximity operations, and astrodynamics applications.

He can be reached at leed61@naver.com. His permanent address is 120 Hwagaelee, Wando-eup, Wando-koon, JeonNam, Republic of Korea.